A Dissertation for the Degree of Doctor of Philosophy

Studies on efficient hepatocyte differentiation using bioprinting and graphene quantum dots

바이오프린팅과 그래핀 양자점을 이용한
효율적인 간세포 분화 연구

By

Hyun Kyoung Kang

August 2022

Major in Veterinary Pathobiology and Preventive Medicine,
Department of Veterinary Medicine,
Graduate School of Seoul National University

Studies on efficient hepatocyte differentiation using bioprinting and graphene quantum dots

By

Hyun Kyoung Kang

A dissertation submitted in partial fulfillment of
the requirement for the degree of
DOCTOR OF PHILOSOPHY
Supervisor : Kyung-sun Kang, D.V.M., Ph.D.
June 2022

Dissertation Committee:

Rhee, KunSoo
    (Chairman of Committee)

Kang, Kyung-Sun
    (Vice chairman of Committee)

Kong, Young-Yun
    (Committee member)

Yun, Jun-Won
    (Committee member)

Lee, SeungHee
    (Committee member)

ABSTRACT

Studies on efficient hepatocyte differentiation using bioprinting and graphene quantum dots

Hyun Kyoung Kang

Major in Veterinary Pathobiology and Preventive Medicine,
Department of Veterinary Medicine
Graduate School of Seoul National University

Supervisor: Kyung-Sun Kang, D.V.M., Ph.D.

Three-dimensional (3D) bioprinting is a promising technology to establish a 3D in vitro hepatic model that holds great potential in toxicological evaluation. However, in current hepatic models, the central area suffers from hypoxic conditions, resulting in slow and weak metabolism of drugs and toxins. It remains challenging to predict accurate drug effects in current bioprinted hepatic models. In the first of this study, I constructed a hexagonal bioprinted hepatic construct and incorporated a spinning condition with continuous media stimuli.

Interestingly, under spinning conditions, cells in the boprinted hepatic construct exhibited enhanced proliferation capacity and functionality compared to those under static conditions. Increased number of spheroids under spinning conditions exhibited intensive TGFβ-induced epithelial-to-mesenchymal transition (EMT) and increased susceptibility to acetaminophen (APAP)-induced hepatotoxicity as well as hepatotoxicity prevention by administration of N-acetylcysteine (NAC). These results demonstrate that the spinning condition employed during the generation of bioprinted hepatic constructs enables the recapitulation of liver injury and repair phenomena in particular. This simple but effective culture strategy facilitates bioprinted hepatic constructs to improve in vitro modeling for drug effect evaluation.

In the second part, the goal of this research was to secure large amounts of human pluripotent stem cell-derived hepatcytes by increasing differentiation efficiency using graphene quantum dots (GQDs). GQDs have been found to promote efficient differentiation of stem cells into a variety of cell types. However, their bioactivity and signalling mechanisms in the hepatic lineage have not been fully investigated. Here, we report that the hepatoblast differentiation rate can be promoted by using Ca2+-rich coffee bean-derived GQDs, where the incorporated calcium ions activate the signaling of insulin-like growth factor 1 receptor (IGF1R)-AKT. We also found that the human pluripotent stem cells (hPSCs)-derived hepatoblasts from the CB-GQDs treatment tended to upregulate the maturation into hepatocyte-like cells and downregulate the differentiation towards cholangiocytes, therby successfully obtaining a large number of functional hepatocyte-like cells. Moreover, the activation of IGF1R from the CB-GQD treatment enhances the hepatoblast differentiation efficiency regardless of growth factors, implying that chelated calcium may play a key role in

activating IGF1R. Our findings suggest that CB-GQDs with independent bioactivity can be widely used in place of insulin-like growth factor 1 (IGF1) and represent a cost-effective growth factor as well as a potential differentiation factor.

In conclusion, these findings imply that (i) dynamic condition can be a strategy to alleviate the hypoxic condition of large-sized bioprinted in vitro hepatic models to promote drug matabolism, (ii) hepatoblast differentiation of pluripotent stem cells is related to the presence of calcium, and chelated calcium in CB-GQDs help secure an affinity from IGF1R present in the phospholipid membrane through electrostatic attraction, potentially contributing to promoting hepatoblast differentation via calcium channels.

TABLE OF CONTENTS

CHAPTER I

Establishing a 3D In Vitro Hepatic Model Mimicking Physiologically Relevant to In Vivo State

CHAPTER Ⅱ

Improved Hepaotblast Differentiation of Human Pluripotent Stem Cells by Coffee Bean Derived Graphene Quantum Dots

LIST OF ABBREVIATIONS

3D	Three-dimensional
EMT	Epithelial-to-mesenchymal transition
APAP	Acetaminophen
NAC	N-acetyl-L-cysteine
HepG2	Human hepatocarcinoma
DMEM	Dulbecco's Modified Eagle's Medium
PI	Propidium iodidle
DAPI	4', 6-Diamidino-2-phenylindole
ECM	Extracellular matrix
GelMA	Gelatin methacrylate
PAS	Periodic acid-schiff
p62	ubiquitin-binding protein p62
H2AX	H2A histone family member X
ELISA	Enzyme-linked immunosorbent assay
ALB	Albumin
A1AT	Alpha-1-antitrypsin
AFP	Alpha-fetoprotein
TGF	Transforming growth factor
TNF	Tumor necrosis factor
IL	Interleukin
GQDs	Graphene quantum dots
hPSCs	human pluripotent stem cells
Ca^{2+}	Calcium ions
CB-GQDs	coffee bean derived GQDs
CF-GQDs	carbon fiber derived GQDs

TEM	transmission electron microscopy
AFM	atomic force microscopy
FT-IR	Fourier transform infrared
XPS	X-ray photoelectron spectroscopy
CK18	cytokeratin 18
HBs	Hepatoblasts
ASGR1	Asialoglycoprotein receptor 1
ZO-1	Zonula occludens-1
MRP2	multidrug resistance-associated protein 2
AQP1	Aquaporin-1
IGF1	Insulin-like growth factor 1
IGF1R	IGF1 receptor
HBF	Hepatoblast medium minus FBS
MAPK	Mitogen-activated protein kinase

LIST OF FIGURES

CHAPTER Ⅱ

LIST OF TABLES

LITERATURE TABLE

CHAPTER Ⅱ

LITERATURE REVIEW

A. Artificial liver construction in tissue engineering

In the United States, one name is added to the organ transplant waiting list every 15 minutes (Abouna et al., 2008). The demand for organ transplants increases rapidly, but less than one-third of patients in the waiting list can receive matching organs from donors. One of the most promising technique to alleviate this shortage is tissue engineering, which uses a combination of cell, engineering and material methods to produce artificial organs (Langer et al., 1993). Artificial organs are engineering devices or tissues that can be implanted in people to replace damaged organs in the context of living tissues. Artificial organs are categorized into three types: "Xenotransplantation" that use animal organs, "cell-based artificial organs" that use cells or biomaterials, and "electronic devices" that combine bio or mechanical with electronics. The focus of this review is on cell-based artificial organs.

The liver is the largest internal organ in the human body and performs a number of essential functions, including toxins and drug metabolism. The homeostasis process of this organ is supported by numerous cells that form integral units. Hepatocytes, sinusoidal endothelial cells, Kuffer cells, and stellate cells communicate through direct contact and diffusion (Marta et al., 2020). It also has a dual blood supply circulation system that included nutrient-rich veins and oxygen-rich arteries, showing remarkable regeneration capacity through continuous and sufficient oxygen and nutrition supply. Despite this remarkable self-regenerative ability, total liver transplantation is the only treatment option for patients with end-stage cirrhosis, liver cancer, or

chronic liver failure. Unfortunately, this procedure is limited by lack of donors, immunological complications associated with rejection, and the use of immunosuppressants. As a result, in vitro devices such as artificial liver and cell transplantation technology have been developed, allowing them to bypass the limitations of liver transplantation.

Recently, liver tissue engineering has emerged as a potential technology for efficient regeneration of liver tissue. Various combinations of cell sources and biomaterials are being tested in the context of liver tissue engineering. Creating liver microtissues is a multidisciplinary endeavor, requiring expertise from engineering and materials science in addition to molecular and cellular biology. Hepatocytes possess incredible self-organizing ability in 3D culture, and the use of biomaterals can improve the structural and functional complexity of the microtissues. Recapitulating the lobule, the functional unit of the liver, is of great interest in liver tissue engineering.
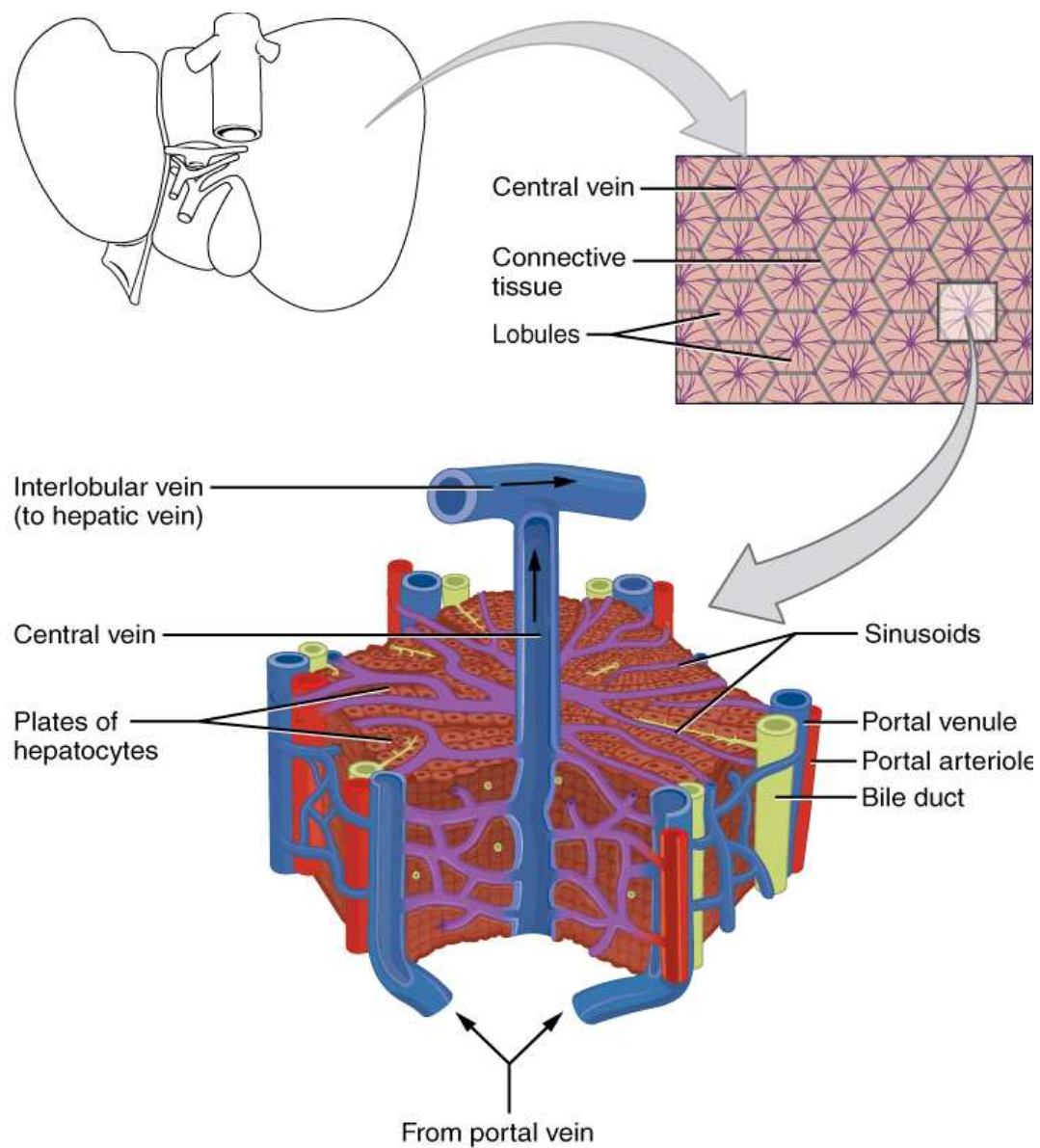
Figure 1. Schematic illustration of liver

B. 3D Bioprinting in tissue engineering

Hepatocytes easily lose hepatic characteristics and exhibit low viability and proliferation capacity in traditional 2D culture systems (Zhang et al., 2010). However, 3D scaffolds made of biocompatible and biodegradable polymers have been shown to improve cell survival and hybridization by creating microenvironments such as 3D extracellular matrix (ECM), which mimic in vivo conditions. The manufacture of biomaterials with adequate mechanical strength and various bioactive molecules can significantly promote the regeneration of liver by enabling biochemical and mechanical signal modulation that promotes cell proliferation, differentiation, and functioning of hepatocytes. As biomaterials to be used in tissue engineering, there have been many reports using decellularized matrices and hydrogels, and scaffolds using 3D bioprinting technology from natural and synthetic polymers(). Among them, since decellularization process requires a relatively long time, 3D bioprinting technology, which can construct 3D scaffolds with high speed, availability and low cost, has been spotlighted in tissue engineering and regenerative medicine. The four major bioprinting techniques of extrusion, inkjet, laser based-and sterolithography bioprinting each have advantages and disadvantages (Table 1).

Table 1. Comparision of commonly used 3D bioprinting methods.

Feature	Extrusion	Inkjet	Laser	Sterolithography
Density (cells/ml)	High-spheroids	10^6-10^7	10^6-10^7	$<10^8$
Viability (%)	40-95	>85	>95	>90
Speed	low	medium	high	High
Resolution (µm)	100~1000	50~300	10~50	<100
Cost	medium	low	High	Low
Advantages	Simple High cell density	Low viscosity Fast print Low shear forces	Distribution of biomaterial in solid or liquid	Nozzle-free High accuracy High viability
Disadvantages	Viscous liquid High shear stress	Low cell density Mechanical deformation	Damages from temperature	Damages from photocuring UV Light source toxicity

Four major types of bioprinting techniques have been developed to reflect the sophistication of the structure and the unique characteristics of the organ. This figure is modified from (Klak et al., 2020).

Extrusion based bioprinting is one of the most commonly used technique which relies on extruding biomaterials from cartridges by mechanical forces or pneumatic pressure onto the platform in a continuous manner. Since extrusion based bioprinting is simple and can laden high density of cells, it has been used in various bioprinted tissue and organs including vessel (Dolati et al., 2014; Duan et al., 2013; Miller et al., 2012; Kolesky et al., 2014; Khali et al., 2009), bone (Loozen et al., 2013), cartilage (Visser et al., 2013), skeletal muscle (Merceron et al., 2015; Zhang et al., 2013), tumor (Zhao et al., 2014). From a technical point of view, bioprinting enables controlled and automated biological model production. However, depending on the biomaterial in which the cell is embedded, this process requires thorough optimization of individual steps. The most important aspects of this are the preparation of bio-ink for bioprinting with a composition imitating the native cell environment, optimization of the conditions of the bioprinting process, evaluation of the final bioprinted structure, and monitoring of the state of the target cell of the bioprinting process. Synthetic and natural polymers like as alginate, gelatin, collagen, polyethylene glycol (PEG), hydroxypartite, and others have been produced to match biocompatibility qualities and ECM structure and formation for this purpose. (Bodhak et al., 2010; Tevlek and Aydin, 2017). Various printing technology have been developed for refinement of bioprinting structure and reflect the characteristic of tissue in vivo, leading to optimization of bioprinitng conditions. In addition, efforts have been made to facilitate the exchange of nutrients and growth factors through bioreactor or coculture with various cells to simulate the heterogenic environment in vivo (Lee et al., 2016). In addition, there have been reports of studying cell viability, migration, cell-cell and cell-ECM interaction followed by the culture periods. In particular, in

the case of the liver, since the main functions are drug and toxin metabolism, drug screening and toxicological evaluation using chips have been developed after bioprinting in an ultra-small size (Guilemot et al., 2011).

Table 2. 3D bioprinting methods, cell source, and biomaterials for construction of artificial liver.

Cell source	Materials	Methods	References
Mouse primary hepatocyte	3% Alginate	Extrusion	Kim et al., 2017
Human Pluripotent stem cells	RGD-coupled sodium alginate, Calcium chloride dihydrate, Barium choloride	Extrusion	Faulkner-Jones et al., 2015
Primary rat hepatocytes, Human endothilial cells(HUVECs), Human lung fibroblasts	Polycaprolactone (PCL), polylactic glycolic acid.	Extrusion	Lee et al., 2016
HepG2 cells	3% Alginate	Extrusion	Jeon et al., 2017
hiPSC-hepatic cells, HUVECs, adipose-derived stem cells (ADSCs)	5% gelatin mthacrylate (GelMA), 2% Glycidal methacrylate-hyaluronic acid (GMHA)	Digital light processing (DLP)	Ma et al., 2016

C. Cell sources for Liver Tissue Engineering

Cellular models for liver disease and regeneration mainly focus on the hepatocytes, which are the main parenchymal cells that account for 80% of liver cells. It is important to select the appropriate cell source for liver tissue engineering applications to consider cost, availability, reproducibility, scalability, and physiological relevance.

Primary hepatocytes are considered the golden standard among different kinds of resources to obtain hepatocytes in vitro, but there are practical limitations in using as stable cells for cell therapy or tissue engineering. These limitations includes the lack of donor liver tissue which will be isolated and the loss of functionality and hepatic characteristics during expansion and cryopreservation in vitro.

Stem cells that can be differentiated into the hepatic lineage are considered a novel resource in liver tissue engineering. Stem cells include embryonic stem cells, induced pluripotent stem cells, mesenchymal stem cells. Embryonic stem cells have infinite proliferation capacity and can be differentiated into any cell or tissue type, including hepatic lineages. Adult stem cells have limited differentiation capacity despite their high safety, while embryonic stem cells and reverse differentiation stem cells have high differentiation capacity, but have a risk of teratoma formation in the body.

However, direct reprogramming technology allows somatic cells obtained from fibroblasts, skin, and urine to be differentiated into liver cells in the process of reverse differentiation. It does not go to the stage of universal differentiation, so it is not tumorigenic, but it is difficult to mass produce, and has the disadvantage of low direct reprogramming efficiency.
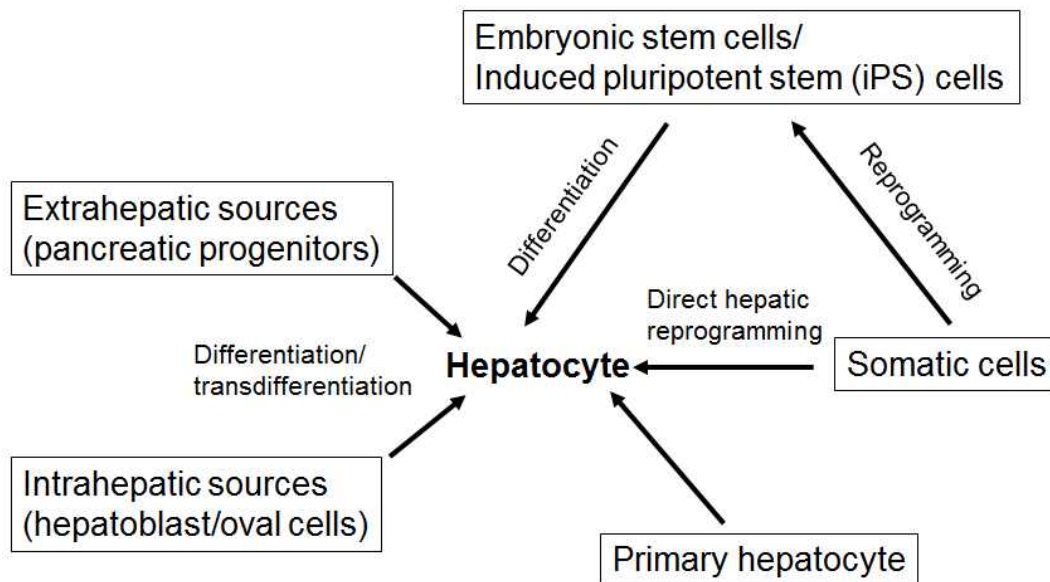
Figure 2. Sources of hepatocytes.

Developing cell-based therapy for treating liver disease is hampered by a lack of suitable hepatocyte sources. Methods for improving the expansion of primary human hepatoctyes in vitro, the directed differentiation of pluripotent stem cells (both ESCs and iPSCs), the differentiation of either intrahepatic or extrahepatic adult progenitor cells, and new methods for the direct reprogramming of adult somatic cells to hepatic cells are all being investigated. (Sangeeta et al., 2014)

Differentiation of Human Pluripotent Stem Cells (hPSCs)

hPSCs, including hESC and hiPSC, have great potential as unlimited cell sources for both basic research and patient-specific cell therapy. But there are limitations to overcome in order to realize their full potential. These include efficient induction of desired cell types from hPSCs and scalable production of mature cells to form functional tissue structures suitable for transplantation. In general, when human embryonic stem cells are cultured without the treatment of external factors such as specific growth factors or compounds, only basic fibroblast growth factors (bFGF) are removed, spontaneous differentiation is initiated and differentiated into various cells. However, the widespread differentiation ability of human embryonic stem cells into various cells serves as a disadvantage for the ultimate purpose of differentiating only certain cells, making it impossible to obtain a large number of desired cells through voluntary simple differentiation. Therefore, studies have been actively conducted recently on the development of effective induction differentiation techniques including the treatment of growth factors, inhibitory factors, or compounds with similar activity to increase the differentiation yield to specific cells.

Growth factors and chemical compounds are essential to effectively differentiate from hPSCs into desired cells. Growth factors and hormones regulate stem cell differentiation and versatility, but so far laboratory procedures rely on processes with expensive cytokines and unclear mechanisms of action. In most cases of artificial growth factors, it is easy to lose bioactivity through repeated thawing processes because they must be stored in freezing with an expiration time. Therefore, the key components of the new differentiators should include

cost-effective producibility and ease of storage, while exhibiting a clear signaling pathway.
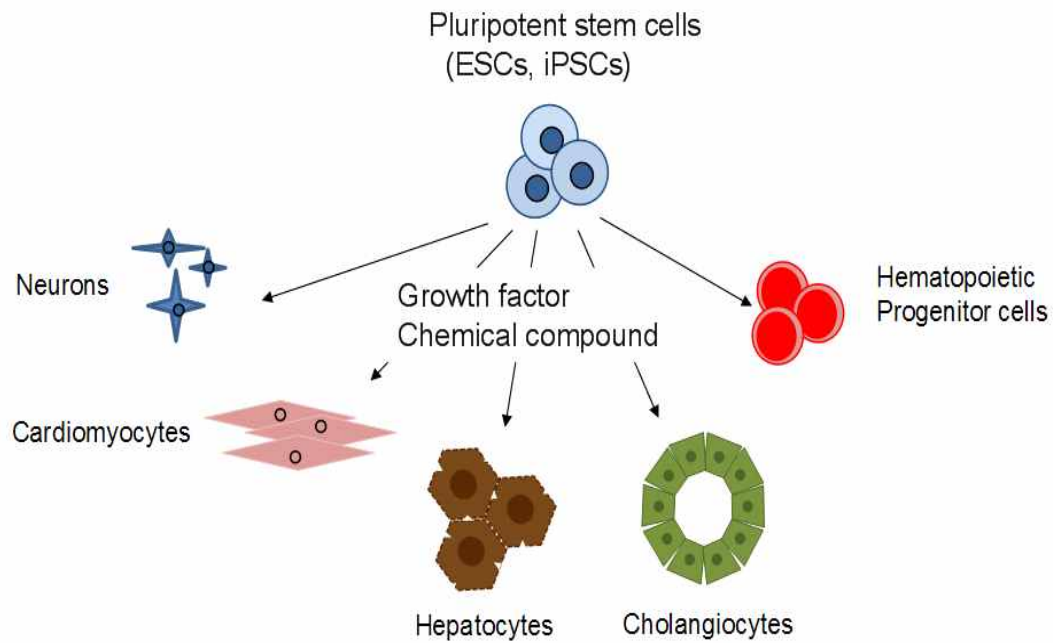
Figure 3. Differentiation of pluriopotent stem cells into multiple cell types.

Pluripotent stem cells, including esc and ipsc, have infinite proliferation capabilities and have the ability to differentiate into all cell types. In order to differentiate into the desired cell type, growth factors, chemical compounds, and small molecules that stimulate specific signals are essential. This figure is modified from (Hwang et al., 2021).

D. Nanomaterials in stem cell differentiation

Nanomaterial is a material having a microstructure of a characteristic length scale (at least one dimensional) in a nanometer range (~1 to 100 nm), and includes carbon nanotubes (CNTs), graphene (GR), and silicon nanoparticles. Nanomaterials are in the spotlight in biomedical and biomedical fields, such as drug delivery systems and tissue engineering 3D scaffolds, due to their unique characteristics such as controllable particle size, large surface-to-volume ratio, adjustable surface chemistry, and biocompatibility. Recent accumulated evidence has shown that nanomaterials can promote stem cell proliferation and differentiation, and there have been many efforts to explore the modulation methods and mechanisms. Different types of nanomaterials have been identified to regulate the differentiation of stem cells (i.e., ESC, iPSC, MSC) into different types of cells, including adipocytes, myocardial cells, osteoblasts, and neurons, through different mechanisms. Nanomaterials also play an important role in controlling the chemical and physical properties of the surrounding microenvironment by manipulating cell behavior and contributing to stem cell growth and differentiation due to their small size, easy synthesis, and multifunctional surface functionality. Supplementing certain differentiation factors, such as growth factors and bioactive molecules, to the medium is a widely accepted pathway to promote stem cell differentiation (Lee et al., 2017). Recently, accumulated evidence shows that some nanomaterials, such as functionalized CNTs and GRs, can promote stem cell proliferation and differentiation without a speci fic medium containing additional supplements.

Due to the high interest in nanomaterials in medicines, much attention has been given to the potential toxicity of graphene through administration throughout the route, including ingestion, inhalation, systemic and skin applications. Although there are reports of graphene being absorbed into the organ and signs of oxidative stress stimulation, clear conclusions about toxicity are hampered by the use of various capacities and types of graphene and its derivatives. Nevertheless, the reason behind the improvements observed in cell differentiation and tissue regeneration is still explained. Understanding how graphene affects cell fate is important for rational material design and treatment strategies. Considering that most nanomaterials do not deteriorate after being absorbed by cells in vitro, the use of natural resource-based nanomaterials with minimal toxicity is a simple but effective strategy for increasing biocompatibility. Therefore, new biologically active nanomaterials based on potentially natural materials can be an attractive candidate for improving differentiation efficiency.
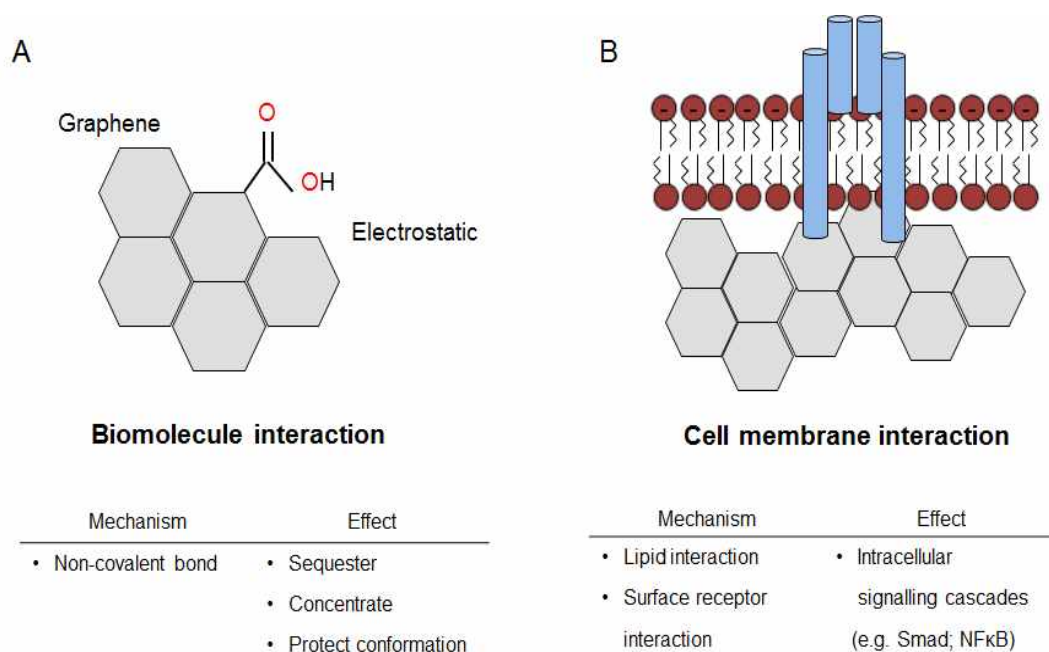
Figure 4. Role of graphene famly nanomaterials (GFN) in stem cell differentiation.

The environment and cellular activity are affected by the physical and chemical characteristics of graphene family nanomaterials (GFN), modulating cell response toward differentiation. (A) GFN interacts with hormones, growth factors, and other biomolecules through a variety of chemical interactions (e.g. electrostatic, p-p bonds, hydrogen bonding, hydrophobic interactions), improving the local bioavailability and thus cell differentiation. (B) When the membrane comes into touch with GFN, intracellular cascades are triggered, which can affect cell responses. This figure is modified from (Loung-Van et al.,2020).

CHAPTER I

Establishing a 3D In Vitro Hepatic Model Mimicking Physiologically Relevant to In Vivo State

1.1 INTRODUCTION

Three-dimensional (3D) bioprinting technology is an emerging approach that has pro- vided researchers an opportunity to fabricate personalized and complex tissue constructs with systemic 3D microarchitecture capable of integration into the native microenvironment (Cui et al., 2020; Tasoglu et al., 2013). Additionally, this technology can be used to create in vitro models for studies of disease mechanisms and drug screening and as a prospective tool in regenerative medicine (Matai et al., 2020; Mandrycky et al., 2016; Bhatia et al., 2014). Among 3D bioprinting methods, extrusion-based bioprinting is one of the most commonly used techniques that enables the deposition of high concentrations of cells within biocompatible biomaterials to reconstruct engineered tissue in a layer-by-layer manner (Tasoglu et al., 2013; Ozbolat et al., 2016). This approach potentially represents the most appropriate method to fabri- cate large-scale engineered tissue, such as the liver, if its main limitations are overcome. These limitations include low cell viability caused by pneumatic pressure-induced shear stress and hypoxic conditions in the core of large-scale bioprinted constructs resulting fromlimited control of cell‑cell and cell‑matrix interactions that hamper the long-term c ulture period (Davoodi et al., 2020; Ozbolat et al., 2015).

The liver is the largest organ with complex architecture and mainly consists of hepato- cytes, which comprise approximately 80% of the liver mass, and other cell types. Addition- ally, the liver primarily metabolizes toxins and drugs first absorbed by the gastrointestinal tract before entering the bloodstream. Indeed, the liver has a dual blood supply circulation system that primarily involves a nutrient-rich vein

and oxygen-rich artery (Lee et al., 2020). Constant and sufficient amounts of oxygen and nutrient supplements enable the high regeneration capacity of the liver, which is one of its important characteristics compared with other organs. Given the liver 's major roles in exogenous xenobiotic metabolism and detoxifica- tion, an appropriate in vitro hepatic model is still needed (Huang et al., 2020; Lauschke et al., 2016; Hosseini et al., 2019). In an in vitro hepatic model, it is important to represent the high metabolism of drugs and toxins resulting from the complex liver microenvironment (Rashidi et al., 2016). Despite many attempts to establish in vitro models, these models do not provide a dynamic microenvironment that is relevant to biochemical and biophysical processes in the liver. Nevertheless, even developed biocompatible extracellular matrices generate cell‑ECM and cell‑cell interactions and are able to maintain cellular properties in current in vitro hepatic models; however, they remain slightly different from native tissue. Thus, another strategy needs to be created to reflect the complete in vivo microenvironment.

Although many studies on the effect of drugs in the liver were previously conducted using animal models, many candidate drugs failed to demonstrate efficacy in humans due to species differences (Bhise et al., 2016; No et al., 2015). The situation is exacerbated by increasing ethical issues over animal-based tests, resulting in restricted animal experiments worldwide (Cho et al., 2017; Ahmed et al., 2017; Lee et al., 2019). These limitations accelerated the development of better predictive platforms that can complement the existing approaches for drug discovery and testing (Cho et al., 2017). In this regard, refined 3D culture methods were discovered to overcome the mentioned restrictions (Bhise et al., 2016, Ahmed et al., 2017; Chang et al., 2010; Jin et al., 2018, Nguyen et al., 2016).

Here, we constructed hexagonal bioprinted constructs using commercial laminin-521- enriched bioink to provide an environment for cells that progressively increased viability and maintained intrinsic functions. Additionally, continuous spinning conditions generated by orbital shakers improved the growth and functionality of encapsulated cells within bioprinted constructs over 2 weeks compared to static conditions. We observed obvious TGF-β-induced epithelial-to-mesenchymal transition and restoration induced by treatment with the TGF-β inhibitor SB431542 under spinning conditions but not under static condi- tions. Furthermore, spinning conditions recapitulated liver injury and repair phenomena, increasing susceptibility to acetaminophen-induced hepatotoxicity and alleviation by ad- ministration of N-acetylcysteine (NAC) in bioprinted hepatic constructs. These results indicate that bioprinted constructs generated under spinning conditions could represent a better strategy for establishing a 3D in vitro hepatic model that is physiologically relevant to the in vivo state.

1.2 MATERIALS AND METHODS

1.2.1 Cell culture

Human hepatocarcinoma cells (HepG2 cells) purchased from ATCC was cultured as a monolayer in high-glucose Dulbecco's Modified Eagle's Medium (DMEM; SH3002201; HyClone, Logan, UT, USA) supplemented with 10% fetal bovine serum (FBS; 26140079; Gibco, Carlsbad, CA, USA) and 0.2% Primocin (ant-pm-1; InvivoGen, San Diego, CA, USA) at 37℃ with 5% CO_2. Cells with 80% confluency were subcultured after dissociation with 0.25% trypsin (GIB-25200-072; Invitrogen, Carlsbad, CA, USA). The medium was changed every other day.

1.2.2 Bioprinting of 3D Hepatic Constructs

GelXA LAMININK and Cellink BIO X 3D pneumatic bioprinters (Cellink, Boston, MA, USA) were used to fabricate functional 3D bioprinted hepatic constructs at room temperature. Hexagonal structures ($3 \times 3 \times 2$ mm^3) mimicking three hepatic lobules were designed using the Tinkercad online 3D modeling program (https://www.tinkercad.com, accessed on 1 May 2021). Cells were prepared at a final density of 3×10^7 cells/mL and mixed with commercial bioinks based on gelatin, alginate, xanthan gum and LAMININ a5b2y1 (IK3 $\times$ 21270301, GelXA LAMINIK521, Cellink). Bioink mixed with the cells was loaded into syringes fitted with a 0.25-gauge nozzle and printed on an ultra low-attachment 6-well plate (3471, Costar, Washington, DC, USA). Bioprinted structures were crosslinked for 5 min with a crosslinking agent containing 50 mM calcium chloride provided by Cellink Company (CL1010001501,

5

Cellink). The hepatic constructs were cultured in 4 mL of high-glucose DMEM supplemented with 10% FBS at 37℃ in a humidified atmosphere containing 5% CO_2. For spinning conditions, culture plates were placed in a platform orbital shaker (88881124, Thermo Fisher Scientific, Waltham, MA, USA) at 60 rpm. The medium was changed every other day.

1.2.3 Live/Dead Cell Staining

Live/dead cell staining was conducted on days 1, 3, 5 and 7 after printing to analyze cell viability in 3D printed hepatic constructs. Calcein AM (15560597, Invitrogen) and propidium iodide (PI; 81845-25MG, Sigma-Aldrich, Saint-Louis, MO, USA) were used at the final concentrations of 0.25 μM and 20 μg/mL, respectively. The images were taken by a confocal microscope (Nikon, Shinagawa, Tokyo, Japan).

1.2.4 Quantitative RT-PCR

Total RNA was extracted using TRIzol (BRL-15596-018, Invitrogen) according to the manufacturer's instructions. cDNA was synthesized from isolated RNA and detected by real-time PCR using SYBR Green PCR Master Mix (4309155, Applied Biosystems, Foster City, CA, USA) and QuantStudio3 (Applied Biosystems). The expression level of each gene was normalized to GAPDH. At least three independent analyses were conducted for each gene. The results were analyzed using Quantstudio Design and Analysis software v1.4.

1.2.5 Histological Characterization (H&E Staining)

The bioprinted hepatic constructs were collected and washed 3 times with phosphate- buffered saline (PBS; SH30256.01, GE Healthcare

Life Sciences, Buckinghamshire, UK). The constructs were fixed with 4% paraformaldehyde (PFA; 158127, Sigma-Aldrich) at 4℃ overnight. The fixed bioprinted structures were processed following a typical method, including dehydration with ethanol, clearing with xylene and wax infiltration with paraffin. Paraffin-embedded blocks were sectioned to 5 μm thickness. Sliced sections were deparaffinized using xylene (1330-20-7, Duksan, Ansan, Republic of Korea) and graded alcohols (64-17-5, Duksan). Samples were stained with hematoxylin (HX73999849, Merck, Darmstadt, Germany) for 30 s and eosin (3200-2, Muto Pure Chemicals, Tokyo, Japan) for 5 min. Finally, samples were washed with running water, rehydrated with graded alcohols and mounted with Canada balsam (C1795, Sigma) for further visualization by microscopy as previously described (Lee et al., 2020).

1.2.6 Immunocytochemistry

Paraffin slides were deparaffinized, rehydrated and heated for antigen retrieval using sodium citrate solution (pH 6.0) at 95℃ for 20 min. The samples were blocked with 5% normal goat serum (K-S-10000-K13, Vector Laboratories, Burlingame, CA, USA) for one hour at room temperature. The slides were then washed thrice with PBS and incubated with primary antibodies using mouse anti-cytokeratin 18 (MAB3234, Millipore, Burlington, WI, USA) and rabbit anti-albumin (102419, GeneTex, Irvine, CA, USA) at a 1:100 dilution at 4℃ overnight. Alexa Fluor mouse 488 (A1100, Invitrogen) and Alexa Fluor rabbit 555 (A-21428, Invitrogen) secondary antibodies were applied at a 1:1000 dilution for 1 h at room temperature. After washing, fluorescent staining was performed with DAPI solution at 1:1000 in PBS for nuclear detection. The sections were mounted with DAKO fluorescence mounting medium (Agilent Pathology Solutions, Santa Clara, CA, USA)

and examined by confocal microscopy (Eclipse TE200, Nikon) as previously described (Sung et al., 2017). The list of antibodies used for immunostaining is provided in Supplementary Table S1.

1.2.7 Functional Analysis

The amounts of secreted human albumin, alpha-fetoprotein, alpha-1 antitrypsin and urea from collected cell supernatants were measured using Human Albumin ELISA Quantification Kit (E80-129, Bethyl Laboratories, Montgomery, AL, USA), Human Alpha Fetoprotein ELISA Kit (ab108388, Abcam, Cambridge, UK), Human Alpha-1 Antitrypsin ELISA (ab108799, Abcam) and QuantiChrom Urea Assay Kit (DIUR-100, Bioassay system, Hayward, CA, USA) according to the manufacturer's instructions.

1.2.8 Western Blot Analysis

The protein concentration was measured using a Pierce BCA Protein Assay Kit (23227, Thermo Fisher Scientific). Approximately 10 μg of protein from each cell was subjected to 8% to 15% sodium dodecyl sulfate polyacrylamide gel electrophoresis and then transferred onto a nitrocellulose membrane. The membranes were blocked with 3% bovine serum albumin solution in TBST, followed by 1 h incubation. After that, the membrane was incubated with primary antibody at 4℃ overnight. The primary antibodies used to probe each protein were as follows: mouse anti-phosphoSmad2/3 (8828, Cell Signaling, Danvers, MA, USA): 1:1000, rabbit anti-Smad2/3 (8685, Cell Signaling): 1:1000, anti-fibronectin (ab2413, Abcam): 1:1000, mouse anti-β-actin (4967, Cell Signaling): 1:1000, mouse anti- phospho-histone H2A.X (05-636, Merck): 1:1000, rabbit anti-cleaved caspase3 (9664, Cell Signaling): 1:1000, rabbit anti-caspase3 (9662, Cell Signaling): 1:1000, rabbit

anti-p62 (610832, BD Bioscience, Franklin Lakes, NJ, USA): 1:500 and rabbit anti-LC3 (NB100-2331, Novus Biologicals, Centennial, CO, USA): 1:1000. Secondary horseradish peroxidase (HRP)-conjugated antibodies (G21040, G21234, Invitrogen): 1:2000. The antibody binding was detected using an enhanced chemiluminescence (ECL) detection kit (RPN2106, GE Healthcare Life Science).

1.2.9 Drug Treatment

For the drug sensitivity assessment, bioprinted hepatic constructs were cultured under spinning conditions for 14 days. Then, the constructs were treated with N-acetyl-L-cysteine (A7250, Sigma-Aldrich) for 12 h. Then, culture supernatants were collected. On day 14.5, bioprinted hepatic constructs were treated with acetaminophen (APAP; A3036-1VL, Sigma- Aldrich) at a working concentration of 15 mM for 48 h. Supernatants were collected every 48 h for 8 days and frozen at $-80\,℃$ for human albumin ELISA and urea production. On the final day, the bioprinted structures were fixed with 4% PFA and embedded in paraffin for histological characterization.

1.2.10 Statistical Analysis

Statistical analyses were performed using GraphPad Prism version 9 Software. In addition, the data are presented as representative examples or mean values when more than three experiments were conducted. Data are presented as the means ± S.D. Two-tailed Student's t-test was performed to compare the data from two groups, or one-way ANOVA followed by Bonferroni's test was performed to compare data from multiple groups throughout our experiments.

1.3 RESULTS

1.3.1 Fabrication of 3D Bioprinted Human Liver Tissue

To create artificial hepatic tissue that mimics native architecture and microenvironment, we encapsulated HepG2 cells, a widely used hepatocarcinoma cell line, in a hexagonal digital pattern with dimensions adjusted to the approximate size of one liver lobule unit. In the first step, three hexagonal units ($3 \times 3 \times 2$ mm^3 each unit) anatomically resembling liver lobules were designed to follow human l iver tissues in vivo (Figure 5A). A laminin-enriched crosslinkable biomixture provided by Cellink company was used as a bioink. Based on previous studies, laminin-enriched bioink was selected to support the maintenance of hepatic profile expression and clonal expansion of encapsulated cells that have the ability to migrate within bioprinted structures after bioprinting (Cameron et al., 2015; Schmidt et al., 2019). Initially, encapsulated HepG2 cells were well distributed based on the movement of the bioprinter nozzle. On day 7 after bioprinting, cells started to aggregate by themselves in a spheroid-like fashion and increased in size at the edge of bioprinted hepatic constructs until day 14 (Figure 5B,C). Consequently, a number of the cells started to relocate out of the structure. We further questioned whether cells in isolated spheroids have relevant hepatic phenotypes and functionality. Although separated spheroids showed liver cell characteristics confirmed by H&E, PAS staining and immunostaining, these spheroids had hypoxic core areas resulting from the absence of extracellular matrix (Figure 7). Previous data report (Talari et al., 2017) similar results in observed data which showed necrotic central region with some cells and cell debris (Figure 7). Additionally, 7 days following bioprinting, single cells located in the interior area of the bioprinted hepatic

construct started to aggregate into small-diameter spheroids 7 days after bioprinting (Figure 5B,C). These results suggest that the surface area of the bioprinted hepatic construct was amenable to the motility of encapsulated cells resulting from sufficient supplementa- tion of nutrients and oxygen to form spheroids compared to the interior. Additionally, these findings implied that a prolonged culture period with the current bioprinted hepatic model will reveal progressive problems and that the method should be improved. To evaluate scaffold biocompatibility, we tested which laminin-enriched bioink developed by Cellink would maintain cell survival, growth and hepatic features of HepG2 cells. On day 7, the highest cell viability and proliferation capacity were observed when printed with GelXA LAMININK521 (Figure 6A,C). Quantification of live cell numbers showed that on day 7, cell viability in bioprinted hepatic constructs was the highest in the hepatic construct printed with GelXA LAMININK521 (Figure 6B). These results suggest that GelXA LAMININK521, unlike other types of bioink, allowed encapsulated cells to extend the culture period with consistent cell viability. Furthermore, we monitored hepatic constructs bioprinted with GelXA LAMININK521 over 14 days to determine whether the cell culture period could be extended. Hepatic constructs bioprinted with GelXA LAMININK521 maintained cell viability (Figure 5D,E) and constant hepatic marker protein expression for 14 days (Figure 5F). In addition, we tested whether the bioink can improve the hepatic function of HepG2 cells in terms of gene expression. PROX1, CYP1A2 and CYP3A4 mRNA expression showed significant differences in bioprinted hepatic constructs mixed with GelXA LAMININK521 compared to other groups at 14 days following bioprinting (Figure 6D). Additionally, the expression of the nonsecreted protein CK18 and the representative hepatocyte marker albumin was upregulated in the

constructs printed with GelXA LAMININK521 (Figure 6E) compared to the other constructs using different bioink types. This result suggested that the encapsulated cells not only proliferated but also expressed constant hepatic markers in the bioprinted hepatic constructs over 14 days (Figure 5G). These findings highlight that GelXA LAMININK521 is the most appropriate scaffold for HepG2 cells to establish 3D-printed hepatic constructs resembling hexagonal liver lobules with improved hepatic properties and sufficient matrix components.
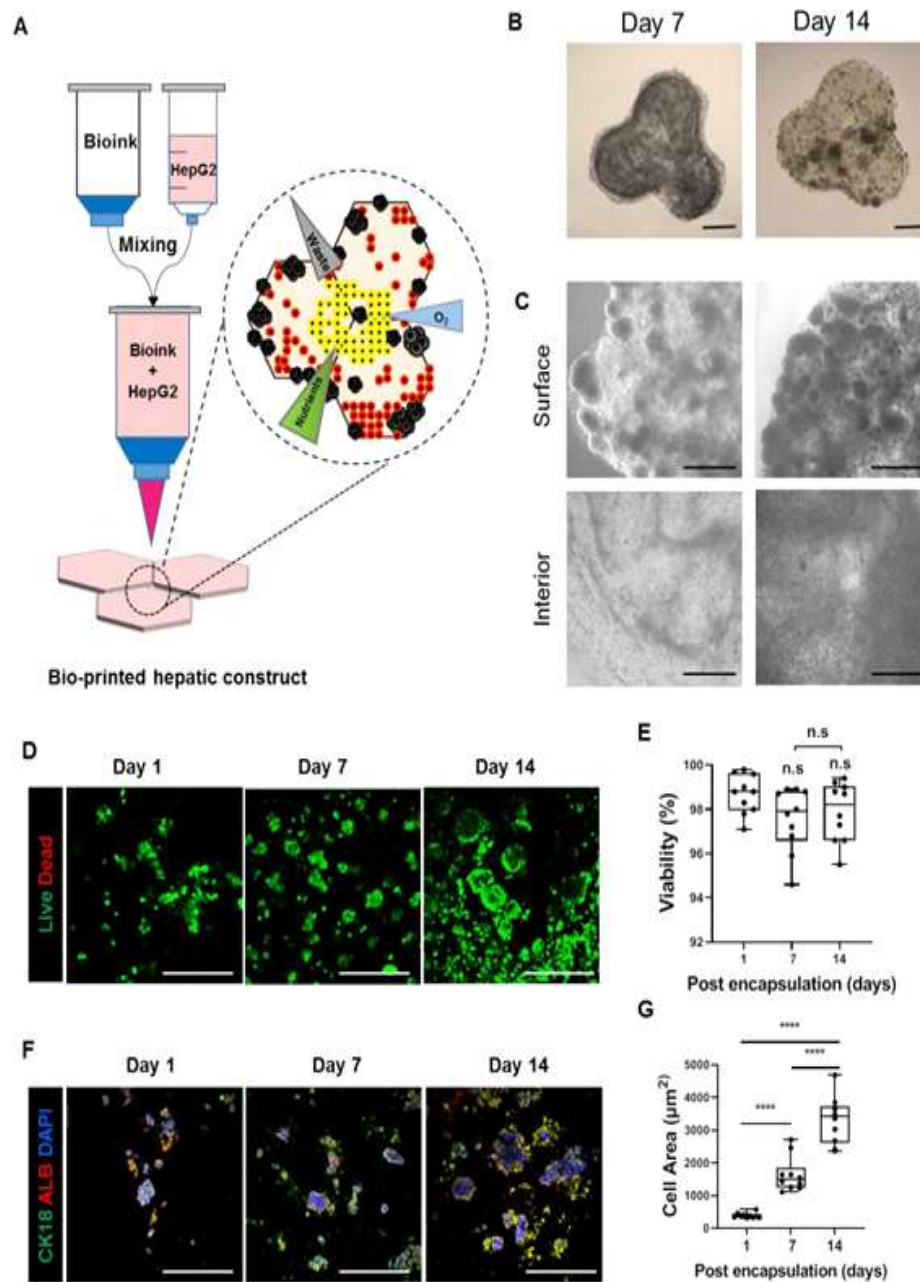
Figure 5. Fabrication of a 3D bioprinted hepatic construct.

(A) Schematic illustration for fabrication of 3D bioprinted hepatic constructs encapsulated with HepG2 cells. (B,C) Bright field images for bioprinted hepatic constructs on days 7 and 14. Cells self-aggregated

into spheroid-like structures. (B) Whole construct, Scale bar = 1000 μm. (C) Surface and interior areas. Surface area of spheroids is greater compared to interior area. Scale bar = 1000 μm. (D) Representative live/dead images of encapsulated cells in 3D bioprinted hepatic constructs on days 7 and 14 stained with calcein AM (green) and PI (red). Scale bar = 500 μm. (E) Quantification of cell viability from live/dead images. Bar graph represents viability of HepG2 cells in bioprinted hepatic constructs at indicated time points. n.s: no significance. (F) Representative immunofluorescence images of HepG2 cells encapsulated in the 3D bioprinted hepatic construct on days 7 and 14. Sections were stained with CK18 (green) and ALB (red). Scale bar = 500 μm. (G) Quantification of cell area of CK18 and ALB double-positive stained cells. Bar graph represents calculated cellular area of encapsulated cells that expressed hepatic marker in bioprinted hepatic constructs at indicated time points. All error bars represent the means ± S.D. from three separate experiments. **** $p < 0.0001$.
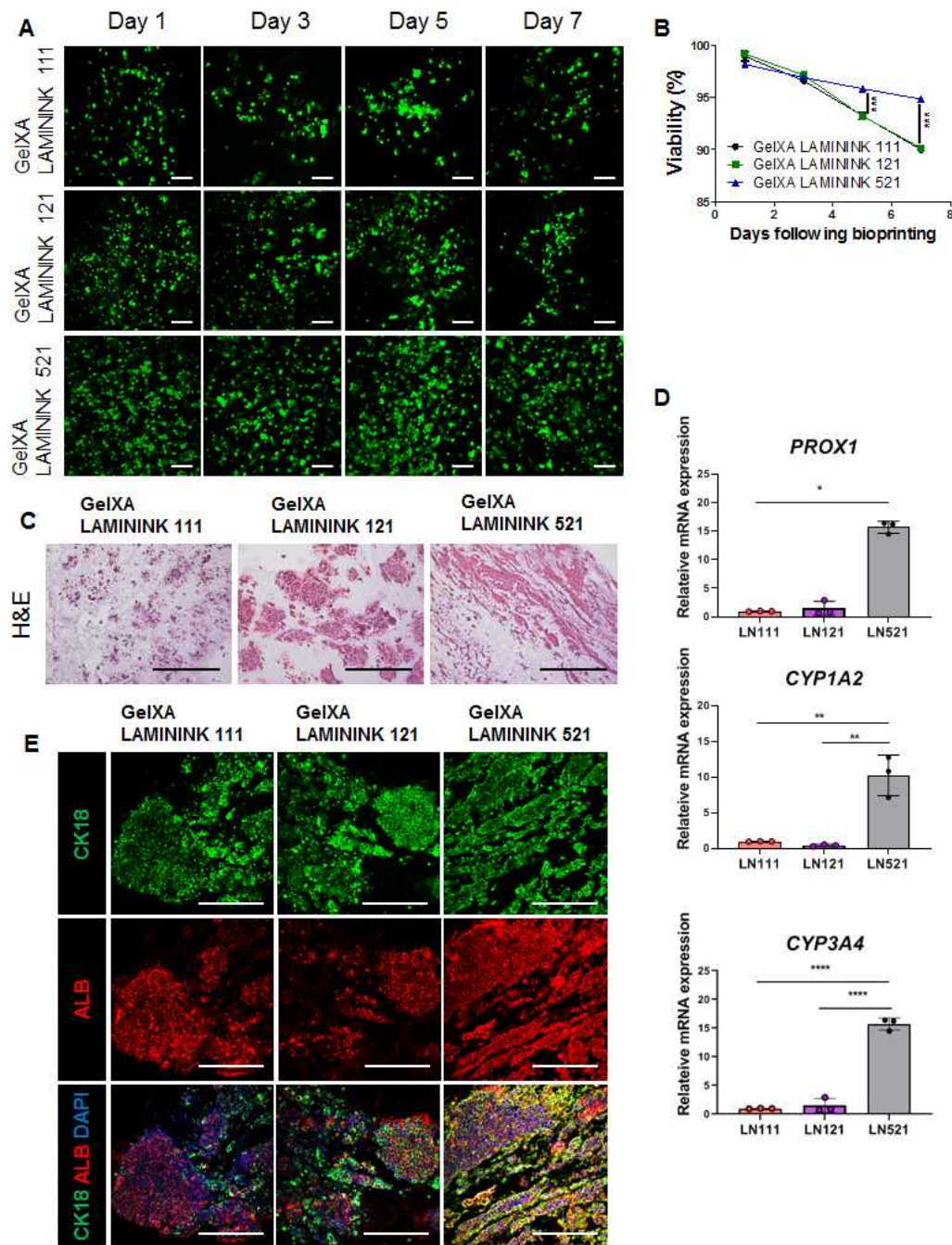
Figure 6. GelXA LAMININK521 is the most appropriate bioink for encapsulated cells to maintain inherent phenotype within bioprinted hepatic constructs.

(A) Representative images for live/dead staining with calcein AM (green) and PI (red) in bio-printed hepatic constructs generated using GelXA LAMININK111, GelXA LAMININK121 and GelXA LAMININK521 on day 1, day 3, day 5 and day 7. Scale bar = 200 μm.

(B) Quantification of encapsulated cells viability in bio-printed hepatic constructs generated using GelXA LAMININK111, GelXA LAMININK121 and GelXA LAMININK521. Line graph represents viability of the cells in different types of bioinks for 7 days.

(C) Representative H&E images for bio-printed hepatic constructs generated using GelXA LAMININK111, GelXA LAMININK121 and GelXA LAMININK521. Scale bar = 250 μm.

(D) Gene expression profiles showing the expression levels of PROX 1, CYP1A2, CYP3A4 in bio-printed hepatic constructs generated using GelXA LAMININK111, GelXA LAMNINK121 and GelXA LAMININK521. All error bars represent the means±S.D. from three separate experiments. One-way ANOVA followed by Bonferroni's test were used for the statistical analysis. *P $\leq$ 0.05 and **P $\leq$ 0.01.

(E) Representative immunofluorescence images of 3D bioprinted hepatic constructs generated in different bioinks. Sections were stained with CK18 (green) and ALB (red) on day 14. Scale bar=250 μm
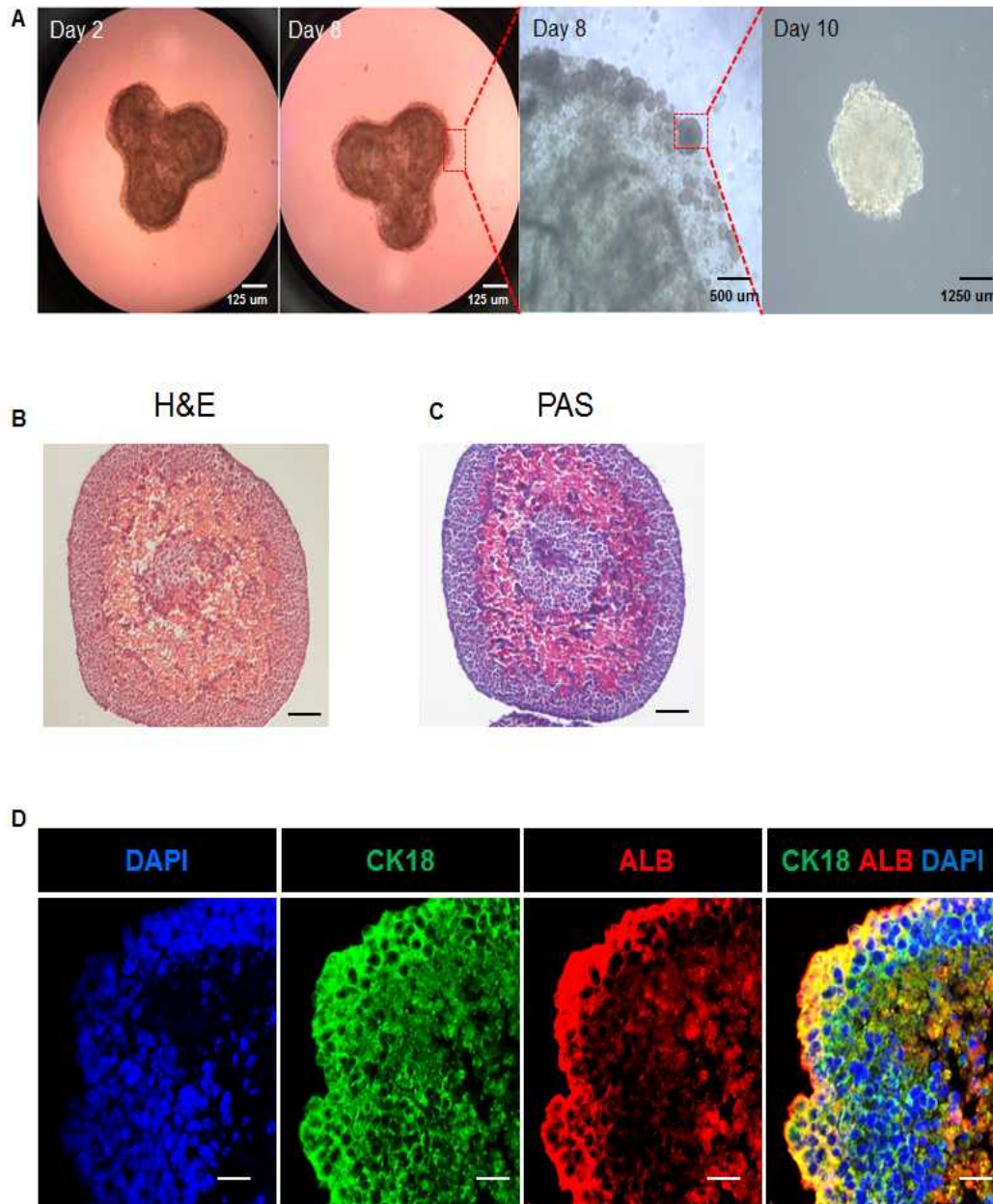
Figure 7. Characterization of self-generated spheroids from 3D bioprinted hepatic constructs.

(A) Representative grow view of bright field images for 3D bio-printed hepatic construct on day 8. Magnified bright field images showed a spheroid generated from bioprinted hepatic constructs were migrated

from bioprinted structures on day 8 and cultured in 96 well ultra low attachment plates during 7 days (Total culture day 15).

(B-C) Representative images of spheroids from bio-printed hepatic constructs stained with (B) H&E and (C) PAS on total culture day 10. Scale bar = 100 μm.

(D) Representative immunofluorescence images of spheroids released from 3D bio-printed hepatic construct on total culture day 15. Sections were stained with ALB (red) and CK18 (green). Scale bar = 100 μm.

1.3.2 Spinning Culture Conditions Enable a Long-Term Culture Period of Bioprinted Hepatic Constructs with Consistent Hepatic Expression and Functionality of Encapsulated Cells

Mechanical stimuli that are absent in static culture conditions contribute to the formation of key physiological structures and affect the growth and functionality of cells encapsulated in bioprinted structures (Rashidi et al., 2016). Based on these facts, we adjusted the bioreactor- like system to recapitulate a microfluidic environment containing a mechanical stimulus mimicking blood flow and diffusion by circular shaking motion using an orbital shaker. HepG2 cells were encapsulated in bioprinted hepatic constructs and cultured under either static or spinning conditions where continuous media flow was induced using a plat- form orbital shaker at 60 rpm (Figure 8A). On day 14, bright-field images exhibited large spheroids, which were observed on the edge of bioprinted hepatic constructs, and spinning conditions contributed to the formation of larger amounts of spheroids (Figure 8B). In addition, cells located in the interior area of the bioprinted hepatic construct under spinning conditions showed more obvious aggregation and proliferation than those under static conditions (Figure 8B). Representative H&E images showed not only a large number of encapsulated cells but also spreading out of the whole bioprinted hepatic construct under spinning conditions compared to static conditions (Figure 8C). Next, we examined whether HepG2 cells in bioprinted hepatic constructs under spinning conditions could maintain hepatic expression and functionality for 14 days. The hepatic expression of HepG2 cells within bioprinted hepatic constructs was visualized with cytokeratin 18 and albumin antibodies. Compared to static conditions, spinning conditions contribute to the formation of larger amounts of $CK18^+ALB^+$ cells in bioprinted hepatic constructs (Figure 8D). This

result indicated that although bioprinting was performed using equal cell concen- trations, the amounts of the cells remaining in the bioprinted hepatic constructs could differ depending on the culture conditions. Consistent with many observed morphological changes, there are also functional reinforcements in hepatic constructs cultured under 3D spinning conditions. In contrast to the increased secretion of human albumin (ALB) and alpha-1-antitrypsin (A1AT), the secreted level of alpha-fetoprotein (AFP) in the culture supernatant of bioprinted hepatic constructs did not show significant differences between static and spinning conditions from day 4 to day 10 (Figure 8E–G). These results are also consistent with the impact of spinning conditions in terms of the growth and maturity of encapsulated cells. Therefore, our results imply that spinning conditions enable HepG2 cells to grow with a consistent hepatic phenotype in bioprinted hepatic constructs over 2 weeks after bioprinting. Additionally, further studies on the secreted level of immature AFP protein compared to other proteins need to be conducted to more accurately explore the effects of spinning conditions on functional maturity utilized by different sources of human hepatocytes. Taken together, reinforcement of the clonogenic growth potential of encapsulated cells and functional maturation can be enhanced under spinning conditions. Additionally, the application of the orbital shaker provides continuous stimuli with appropriate diffusion of oxygen, nutrients and mechanical stimulation that supports defined and well-distributed encapsulated cells.
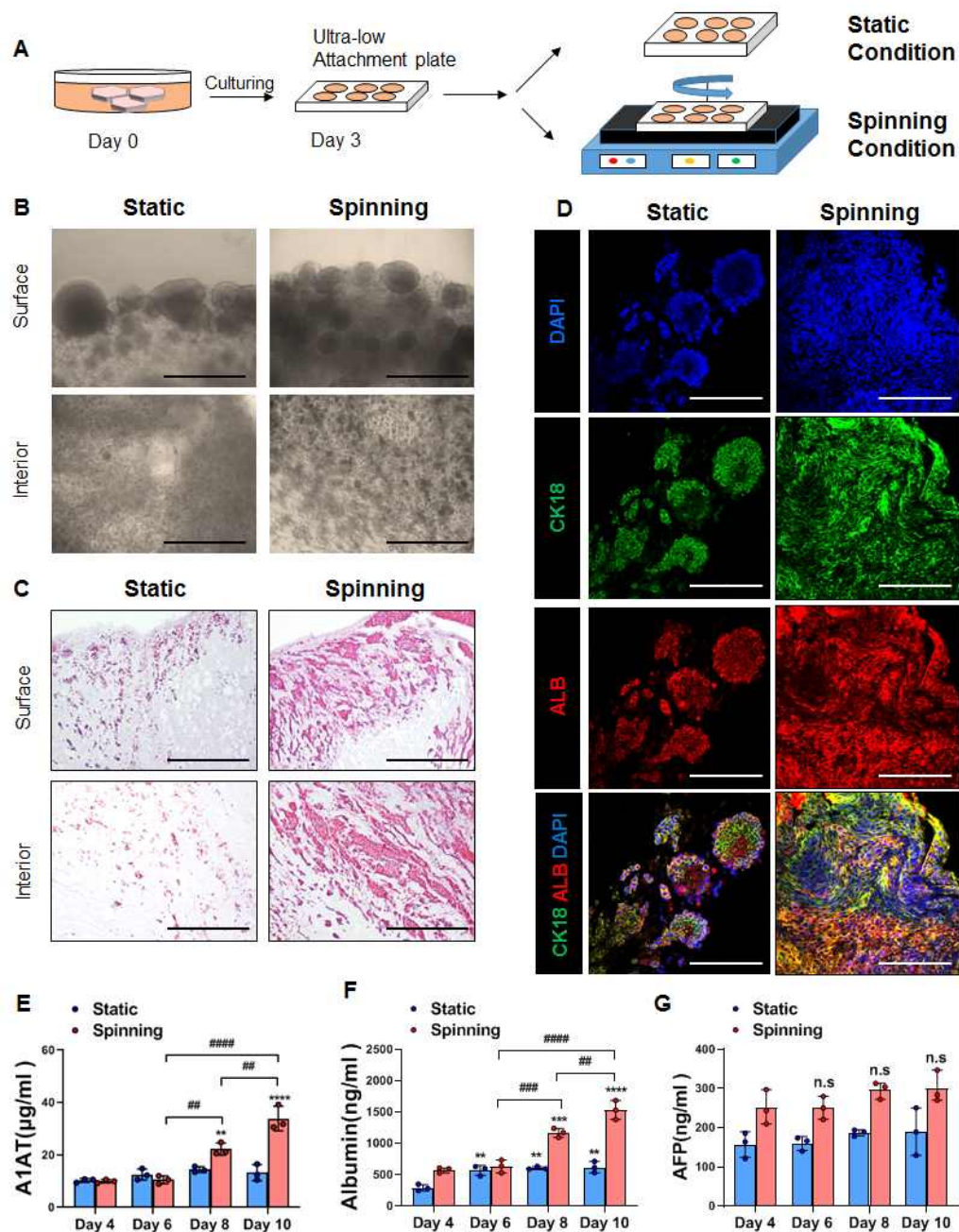
Figure 8. Encapsulated cells in bioprinted hepatic constructs revealed increased proliferative potential and further compacted liver parenchyma under spinning compared to static conditions.

(A) Schematic diagram of bioprinted hepatic constructs. Rotatory culture condition generated by orbital shaker was designated as "spinning",

whereas the condition without rotating was referred to as "static". Rotation was performed at 60 rpm. (B) Morphology of encapsulated cells located at the surface and interior areas of bioprinted hepatic constructs on day 14. Scale bar = 500 μm. (C) Representative H&E staining images showing the localization of encapsulated cells at the surface and interior areas of bioprinted hepatic constructs under static and spinning conditions on day 14. Scale bar = 500 μm. (D) Representative immunofluorescence images of bioprinted hepatic constructs. Sections were stained with cytokeratin 18 (green) and albumin (red) antibodies. Hepatic expression of HepG2 cells within bioprinted hepatic constructs was visualized on day 14 of culturing under static and spinning conditions. Scale bar = 250 μm. (E‐G) ELISA for the secretion level of (E) human alpha-1 antitrypsin, (F) human albumin and (G) human alpha-fetoprotein in bioprinted hepatic constructs at indicated time points. The level was calculated every two days from days 4 to 10. Error bars represent the means ± S.D. from three separate experiments. One- way ANOVA followed by Bonferroni's test was used for the statistical analysis. ** $p < 0.01$, *** $p < 0.001$ and **** $p < 0.0001$ show significant difference between day 4 and another day under the described culture condition. ## $p < 0.01$, ### $p < 0.001$ and #### $p < 0.0001$ indicate significance difference among each day under spinning condition. n.s: no significance.

1.3.3 3D Bioprinted Hepatic Constructs Show Efficient Changes in Cellular Characteristics under Spinning Conditions

The epithelial-to-mesenchymal transition (EMT) process could contribute to hepatic fibrogenesis not only in chronic liver diseases, as reported in other organs, but also in acute liver disease (Pinzani et al., 2011; Choi et al., 2009). Additionally, rapid migration of a large number of fibrogenic cells by EMT could be one of the phenomena by which liver injury occurs (Hosseini et al., 2019). Before we started to establish an APAP-induced liver injury model, constructs were treated with TGFβ to induce EMT as reported previously (Pang et al., 2018). To investigate whether spinning condi- tions enhance the EMT process in bioprinted hepatic constructs, at day 3 after bioprinting, constructs were treated either with TGFβ or with TGFβ in combination with its inhibitor SB431542 for 7 days. On the third day of TGFβ treatment (total culture day 6), morpho- logical changes started to appear differently depending on location in both of the culture conditions. As a result of TGFβ treatment, the encapsulated cells in 3D bioprinted hepatic constructs migrated to the surface area and began to form larger spheroids compared to static conditions. However, cells in the interior area showed a slightly elongated cell morphology exclusively under spinning conditions. Compared with spinning conditions, obvious morphological differences after TGFβ treatment under static conditions were not observed (Figure 9A). H&E staining images for the whole bioprinted hepatic con- struct demonstrated distinct cell numbers and distributions among the areas followed by different culture conditions (Figure 9B). For quantitative real-time PCR analysis and Western blotting, treatment with different TGFβ concentrations (2.5 and 5 ng/mL) was performed to ensure that TGFβ concentration dose-dependently induced the EMT response in the bioprinted hepatic

construct. In particular, under spinning conditions, different TGFβ concentrations confirmed dose-dependent EMT induction, as evidenced by gene expression analysis (Figure 9C). In contrast to static conditions, 2.5 ng/mL TGFβ treatment under spinning conditions had a significant effect on effectors related to EMT gene levels (Figure 9C). No significant differences in relative EMT-related gene levels were noted with different culture conditions in the control groups (Figure 9C). Furthermore, treatment with TGFβ and SB431452 simultaneously showed significant reversible levels of EMT-related gene expression under spinning conditions (Figure 9C). Western blotting of fibronectin and phospho-smad2/3 demonstrated that bioprinted hepatic constructs cultivated under spinning conditions were more dose-dependently responsive to TGFβ signaling than the control groups (Figure 9D,E). Based on these results, spinning conditions accelerate exogenic chemically induced microenvironmental signaling. Therefore, these bioprinted hepatic constructs cultivated under spinning conditions allow us to predict possible drug effects to understand the underlying action mechanism and provide the potential possibility for establishing a drug-induced liver injury model.

D

TGF-β (ng/ml)							Static							Spinning	

Static: - 2.5 5 2.5 5 -
Spinning: - 2.5 5 2.5 5 -

SB431542 (10μM)
Static: - - - + + +
Spinning: - - - + + +

Fibronectin

p-Smad2/3

Smad2/3

GAPDH

E
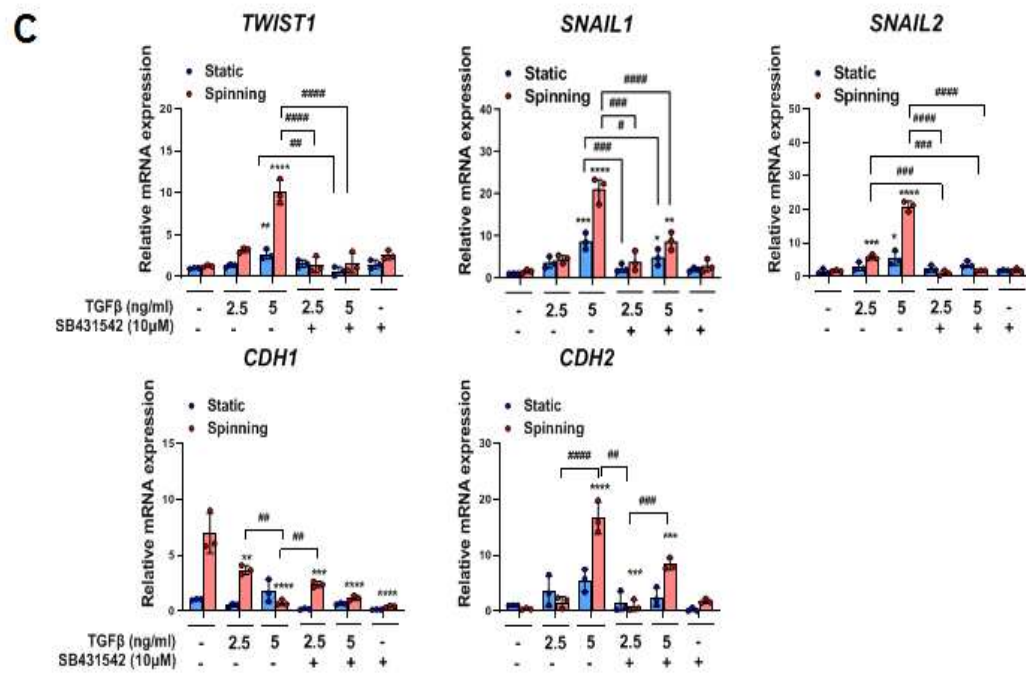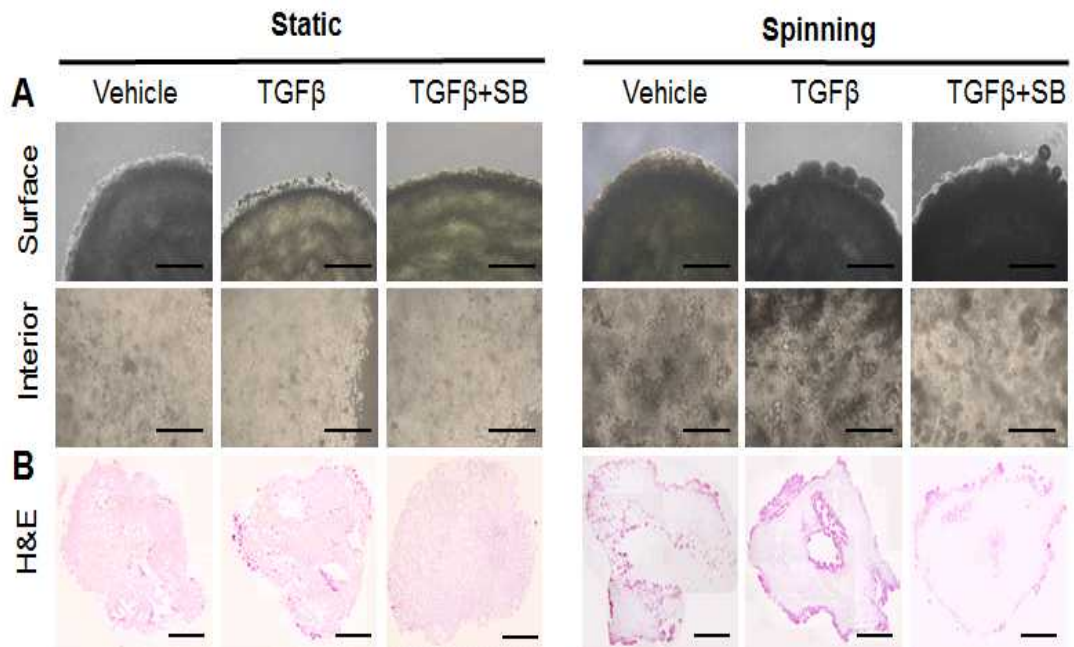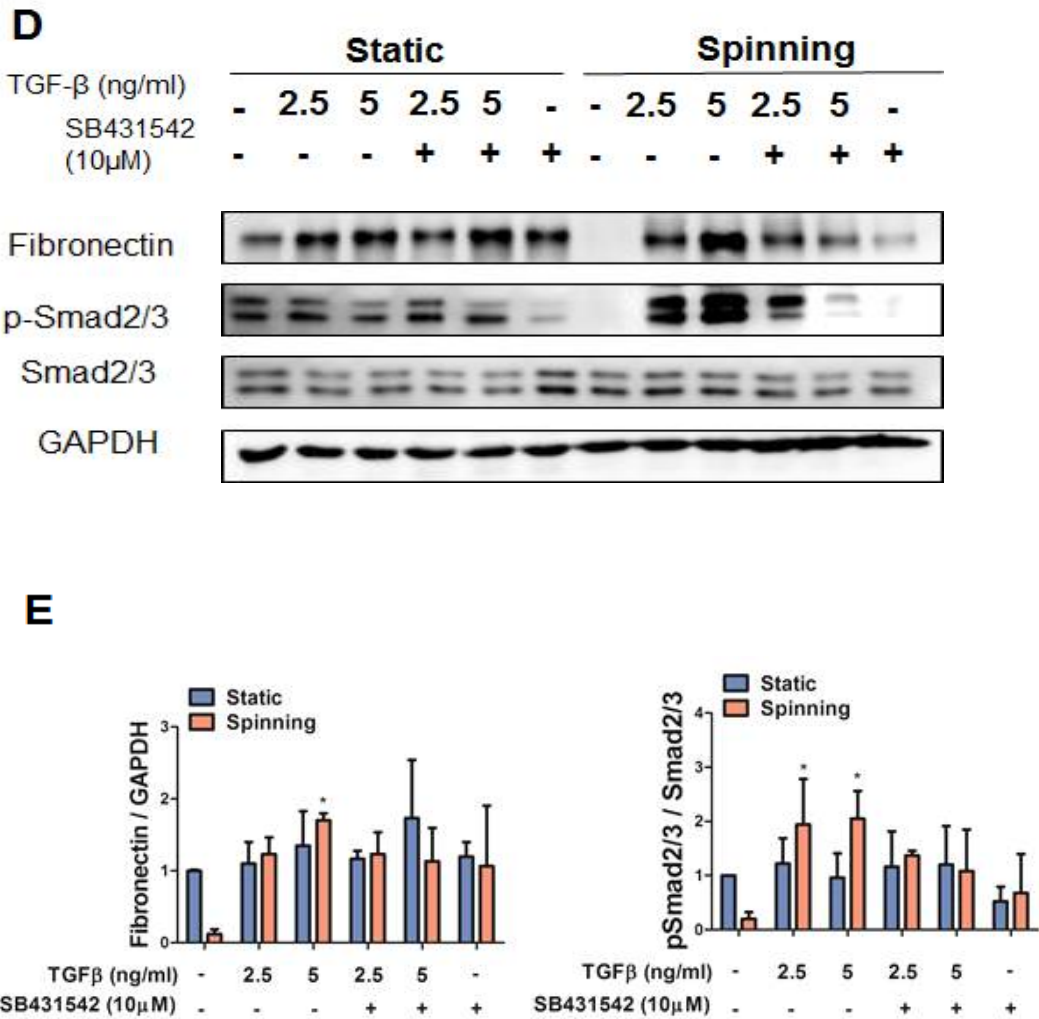
Figure 9. Spinning condition compared to static condition enhances TGF-β-induced epithelial-to-mesenchymal transition (EMT) pathway upregulation and inhibition by SB431542 treatment in bioprinted hepatic constructs.

(A) Morphology of the surface and interior areas of bioprinted hepatic constructs in each group on day 10. Subgroups were divided into nontreated vehicle control, TGFβ-treated and combination of TGFβ with SB431542. Scale bar = 1000 μm. (B) Representative view of growth based on images for H&E staining of bioprinted hepatic constructs

treated with TGFβ or TGFβ and SB431542 together under spinning and static conditions on day 10. Scale bar = 1000 μm. (C) qRT-PCR analysis of TWIST1, SNAIL1, SNAIL2, CDH1 and CDH2 genes that are involved in the EMT pathway in bioprinted hepatic constructs under static and spinning conditions on day 10. Error bars represent the means ± S.D. from three separate experiments. One-way ANOVA followed by Bonferroni's test was used for statistical analysis. * $p < 0.05$, ** $p < 0.01$, *** $p < 0.001$ and **** $p < 0.0001$ show significance between control and other group under indicated culture condition. # $p < 0.05$, ## $p < 0.01$, ### $p < 0.001$ and #### $p < 0.0001$ denote significance among each group under indicated culture condition. (D) Western blot analyses of total cell lysates from bioprinted hepatic constructs using anti-fibronectin, anti-phosphosmad2/3, anti-Smad2/3 and anti-β-actin antibodies. β-Actin served as a loading control. (E) Quantification of fibronectin expression normalized to β-actin and phoshpho-Smad2/3 expression normalized to Smad2/3. One-way ANOVA followed by Bonferroni's test was used for statistical analysis. Error bars represent the means ± S.D. from three separate experiments. * $p < 0.05$ indicate significance between control and other group under indicated culture condition.

1.3.4 The Dynamic Microenvironment Generated by an Orbital Shaker Enables Artificial Liver Construction as a Liver Toxicity Test Model

Because we observed that reinforcement of TGFβ induced the EMT process under spinning conditions, we hypothesized that drug responses in bioprinted hepatic constructs could also be improved depending on culture conditions. To ensure that the drug ef- fect was in accordance with culture conditions, two drugs were selected: acetaminophen (APAP) for the induction of hepatotoxicity and N-acetylcysteine (NAC) for the prevention of APAP-induced hepatotoxicity. The confluency of encapsulated cells and the number of spheroids in the bioprinted hepatic constructs affect drug metabolism (Chang et al., 2010). Hence, we introduced spinning conditions for 14 days to generate a large number of spheroids and provided similar con fluency of encapsulated cells in all the bioprinted hepatic constructs. Extended treatment with NAC hinders hepatic function and impairs recovery potential from APAP-induced hepatotoxicity (Yang et al., 2009). Thus, we treated bioprinted hepatic constructs with NAC 12 h before APAP treatment at the indicated time point (Figure 10A). Under spinning conditions, the control groups showed that a larger number of larger spheroids remained inside the bioprinted hepatic constructs (Figure 10B). However, following APAP treatment for 2 days, we observed reduced confluency of small spheroids in whole bio- printed control groups regardless of culture conditions. After APAP treatment, we divided the group into continuous APAP treatment (NAPAP) and no APAP treatment (Figure 10C). However, significant morphological changes under static conditions compared with NRec and Rec as well as NAPAP and APAP resulting from administration of NAC were not observed (Figure 10B). Representative H&E images show damaged cell nuclei in the APAP group, especially under spinning conditions. APAP

overdose induces severe liver injury accompanied by reactive metabolite formation, mitochondrial damage, cell death via apop- tosis and autophagy signaling (Palabiyik et al., 2016; Liang et al., 2012). To assess the effect of APAP and NAC treatment depending on culture conditions, Western blot analysis was performed (Figure 10D). As expected, RT-PCR and Western blot analysis of bioprinted hepatic constructs subjected to drug treatment under spinning conditions showed higher levels of the proinflammatory cytokines TNF-α, IL-1β and IL-6 in the APAP and Rec groups compared with the static group (Palabiyik et al., 2016; Schuster et al., 2018). On the other hand, IL-10 expression was enhanced in Rec under spinning conditions (Figure 10E). In addition, bioprinted hepatic constructs showed increased apoptosis levels, as observed by the expression of cleaved caspase-3 with constant APAP treatment (Figure 10F,I). Additionally, increased autophagy levels were identified based on a reduction in p62 and an increase in LC3II in the APAP group under spinning conditions (Figure 10F,G). In contrast to static culture conditions, apoptosis and autophagy effects were reinforced in NAPAP compared to APAP. In particular, the effect of NAC administration was significant in the NRec and Rec groups. Consistent with the activation of autophagy and apoptosis pathways with persistent APAP treatment, bioprinted hepatic constructs under spinning conditions showed enhanced levels of gamma H2AX, a hallmark of DNA double-strand breaks (Figure 10F,H). Furthermore, administration of NAC to bioprinted hepatic constructs prevented APAP-induced hepatotoxicity via apoptosis and autophagy signaling. In particular, the NRec and Rec groups exhibited regenerating liver phenomena confirmed by dephosphorylated H2AX expression from acetaminophen-induced hepatotoxicity (Borude et al., 2018). Based on these results, spinning conditions contribute to efficient drug sensitivity

ranging from APAP-induced hepatotoxicity to prevention of hepatotoxicity by administration of NAC compared to static conditions.
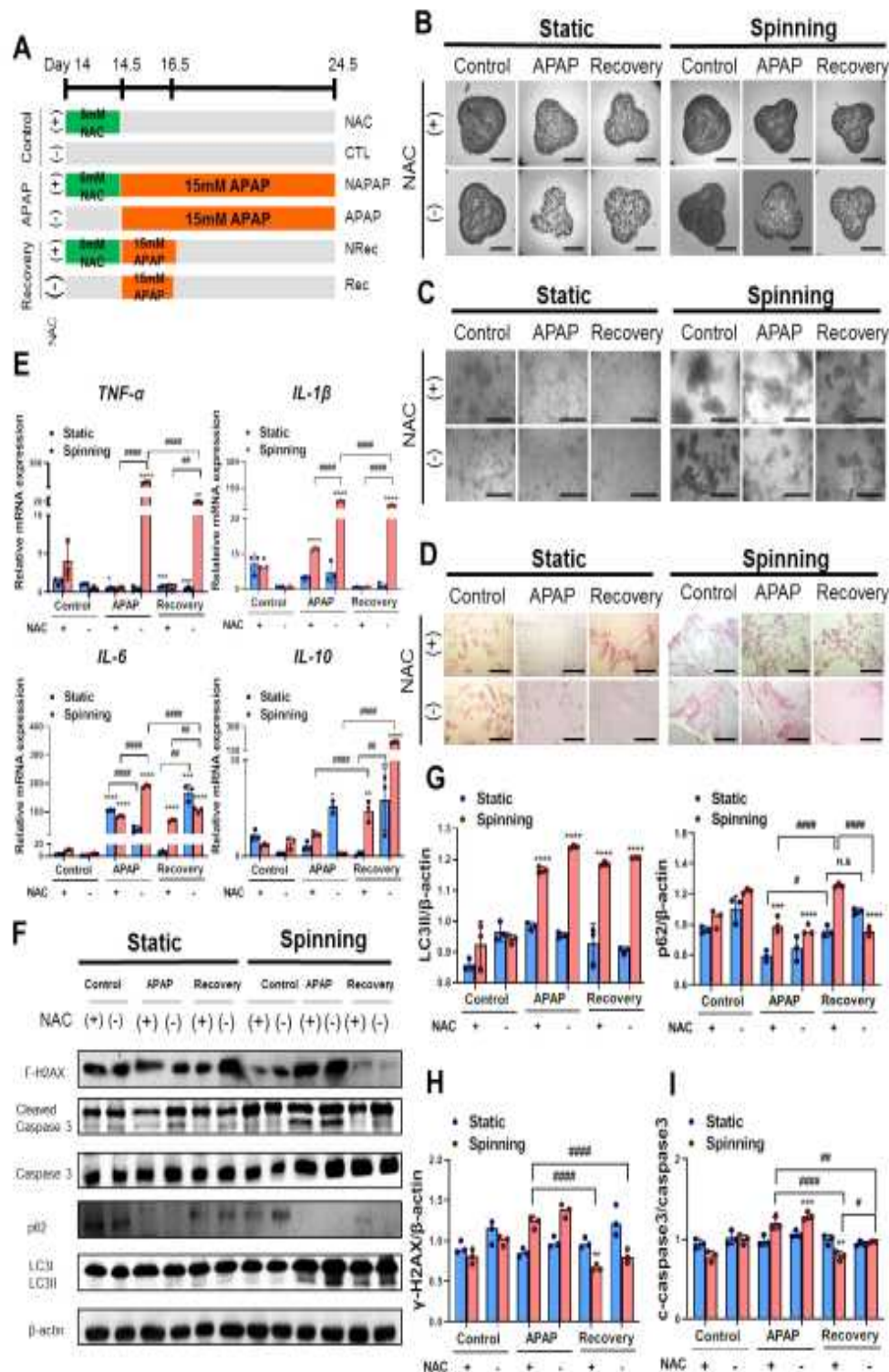
Figure 10. Spinning condition increased APAP-induced hepatotoxicity and prevention by administration of N-acetylcysteine (NAC) in

bioprinted hepatic constructs via apoptosis and autophagy signaling. (A) Schematic diagram illustrating the strategy for treatment with APAP and NAC in bioprinted hepatic constructs at the indicated time point. Groups were divided into control (without APAP for 8 days), APAP (with APAP treatment for 8 day) and recovery (with APAP treatment for 2 days and without APAP treatment after the 2nd day). Control, APAP and recovery groups were subdivided with administration of NAC for 12 h before APAP treatment in control (NAC), APAP (NAPAP) and recovery (NRec) under static or spinning conditions. (B,C) Representative bright field images represent (B) growth of bioprinted hepatic constructs and (C) magnified self- generated spheroids in bioprinted hepatic constructs on day 24.5. (B) Scale bar = 2500 μm. (C) Scale bar = 500 μm. (D) Magnified representative H&E images of bioprinted hepatic constructs on day 24.5 after acetaminophen and NAC treatment. Scale bar = 1000 μm. (E) qRT-PCR validation of TNF-α, IL-1β, IL-6 and IL-10 inflammatory response-related genes followed by APAP and NAC treatment on day 24.5. Error bars represent the means ± S.D. from three separate experiments. One-way ANOVA followed by Bonferroni's test was used for the statistical analysis. * $p < 0.05$, ** $p < 0.01$, *** $p < 0.001$ and **** $p < 0.0001$ represent significance between CTL and other group under indicated culture condition. ## $p < 0.01$ and #### $p < 0.0001$ show significance among each group under indicated culture condition. (F) Western blot analyses of total cell lysates from bioprinted hepatic constructs treated with NAC and APAP using anti-phospho-histone H2A.X (Ser139), anti-cleaved caspase-3, anti-caspase-3, anit-p62, anti-LC3II, anti-LC3III and anti-β-actin antibodies. β-Actin served as a loading control. (G‑I) (G) Quantification of p62, LC3II and (H) pH2AX expression levels normalized to β-actin and (I) cleaved-caspase-3 expression level

normalized to caspase-3. Error bars represent the means ± S.D. from three separate experiments. One-way ANOVA followed by Bonferroni's test was used for statistical analysis. ** $p < 0.01$, *** $p < 0.001$ and **** $p < 0.0001$ show significance between CTL and other group under indicated culture condition, and # $p < 0.05$, ## $p < 0.01$ and #### $p < 0.0001$ indicate significance among each group under indicated culture condition.

1.3.5 Functional Evaluation of Bioprinted Hepatic Constructs Revealed That Hepatotoxicity Induced by APAP and Prevented by NAC Was Enhanced under Spinning Conditions

To examine whether spinning conditions improve the functionality of bioprinted hepatic constructs for drug sensitivity, functional evaluation of bioprinted hepatic constructs was performed by assessing the level of albumin secretion and urea synthesis. The liver synthesizes albumin, which plays a role in carrying hormones, vitamins and enzymes to maintain homeostasis in the body and is secreted into the blood. Additionally, the liver is the primary site for the urea cycle, which converts highly toxic ammonia to urea for excretion. Therefore, the levels of albumin secretion and urea synthesis in blood or culture supernatant represent liver functionality. Specifically, low levels of albumin and urea indicate liver dysfunction. Under spinning conditions, control groups showed not only increased levels of secreted albumin but also increased urea production in culture supernatants compared to the static group. Additionally, APAP treatment in bioprinted hepatic constructs significantly decreased the level of secreted albumin and urea production (Figure 11A−F). Due to inaccuracies during extrusion-based bioprinting, unequal amounts of cells could lead to a misunderstanding of drug effects following different culture conditions. Thus, the fold change in albumin secretion in all groups was examined on day 10 and normalized to the secreted level in the culture supernatant after NAC treatment (Figure 11G,H). Both the fold change of urea production and albumin secretion indicated a more accurate drug effect under spinning conditions because no significant differences were observed in all groups on day 0.5. On day 16.5, the APAP and Rec groups were at a similar stage of acetaminophen-induced hepatotoxicity; however, bioprinted hepatic constructs cultivated under static conditions showed

inconsistent changes in the level of albumin secretion and urea synthesis (Figure 11B,E). Taken together, these results suggest that spinning conditions increased the susceptibility of drugs in bioprinted hepatic constructs immediately and clearly.
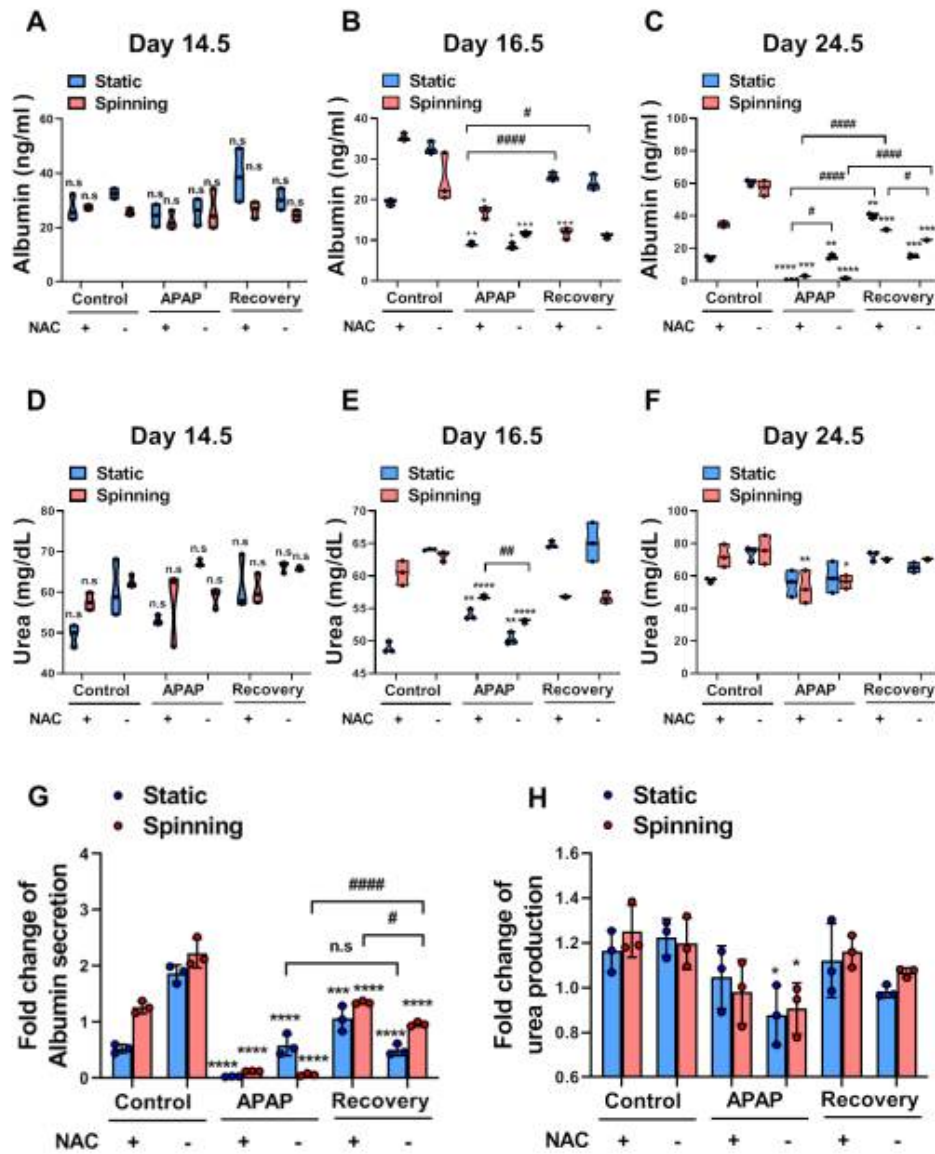
Figure 11. Functional evaluation for APAP-induced hepatotoxicity and prevention by NAC administration showed enhancement of drug sensitivity in the bioprinted hepatic constructs under spinning compared to static conditions. (A‑C) ELISA for albumin secretion levels in bioprinted hepatic constructs in each indicated group cultured under static and spinning conditions on (A) day 14.5, (B) day 16.5 and (C) day 24.5. Culture supernatants were collected every other day starting

on day 1 after bioprinting except during the NAC treatment period. Error bars represent the means ± S.D. from three separate experiments. One-way ANOVA followed by Bonferroni's test was used for statistical analysis. * $p < 0.05$, ** $p < 0.01$, *** $p < 0.001$ and **** $p < 0.0001$ indicate significance between CTL and other group under indicated culture condition. # $p < 0.05$ and #### $p < 0.0001$ show significance among each group under indicated culture condition. (D‒F) Urea production levels in bioprinted hepatic constructs in each indicated group cultured under static and spinning conditions on (D) day 14.5, (E) day 16.5 and (F) day 24.5. * $p < 0.05$, ** $p < 0.01$ and **** $p < 0.0001$ indicate significance between CTL and other group under indicated culture condition. ## $p < 0.01$ shows significance among each group under indicated culture condition. (G,H) (G) Fold change in albumin secretion and (H) urea production in culture supernatant of bioprinted hepatic constructs in each group on day 24.5 normalized to day 14.5 under static and spinning conditions. * $p < 0.05$, *** $p < 0.001$ and **** $p < 0.0001$ show significance between control and other for each group under indicated culture condition. # $p < 0.05$ and #### $p < 0.0001$ indicate significance among each group under indicated condition.

1.4 DISCUSSION

In vitro hepatic models are used by researchers to accurately predict and assess drug response and screening. It is important to represent the high metabolism of drugs and toxins resulting from the complex liver microenvironment (Rashidi et al., 2016). Unfortunately, in most of the currently developed in vitro hepatic models supported by biocompatible scaffolds, it is difficult to evaluate precise drug effects due to the slow diffusion of nutrients and oxygen between media and encapsulated cells. To address the limitations of current 3D cell culture models for hepatotoxicity evaluation (Davoodi et al., 2020; Ozbolat et al., 2015), we developed a 3D bioprinted hepatic model incorporated with a dynamic microenvironment that enables the accurate evaluation of hepatotoxicity drug responses.

To achieve successful bioprinting and develop a decent predictive model, the choice of an appropriate scaffold is an important factor to be considered. Recently, applied polymeric hydrogels have revealed poor stability and low printing accuracy; therefore, various biomixtures are being developed to enhance pre- and postprinting features as well as cytocompatibility and after-printing cellular development (Cui et al., 2020). In this study, GelXA bioinks, which constitute a gelatin methacrylate (GelMA)-based biocompatible mixture in combination with xanthan gum and alginate, were used to enhance printability (Ma et al., 2020). Given that GelMA has remarkable potential in controlling temporal and spatial properties, it is widely used as a 3D scaffold that plays a critical role in cell adhesion, biocompatibility and biodegradability (Morgan et al., 2020). The addition of different types of laminin proteins to GelXA bioink needs

to be optimized followed by the cellular properties of encapsulated cells. Laminins promote cell adhesion in the regenerating liver and provide the liver stem cell niche (Cameron et al., 2015; Carlsson et al., 1981). Additionally, laminin-511- and laminin-521-based matrices support efficient hepatic specification of human pluripotent stem cells and promote the acquisition of hepatic functions (Kanninen et al., 2016). In our study, among different commercially available types of bioinks based on gelatin methacrylate, xanthan gum, alginate and laminin, GelXA LAMININK521 was considered the most appropriate. It induced clonogenic expansion and provided spatial organization of cells with enhancement of hepatic phenotypes in bioprinted hepatic constructs. Cells grown in our 3D models printed with GelXA LAMININK521 formed spheroids with strong cell–cell and cell–ECM interactions within the extracellular matrix. Spheroids containing proliferating, quiescent, hypoxic and necrotic cells more closely mimic the in vivo microenvironment due to the different cell development stages instead of their existence in the same stage of the cell cycle (Edmondson et al., 2014). Consequently, it seems to exhibit an ineffective drug response in contrast to 2D models that are equally exposed to nutrients and drugs in growth media. Given that the 3D model depends on simple diffusion due to the absence of blood vessels, limited penetrability of nutrients and drugs in the media is noted. As a result, restricted oxygenation and nutrition environments in bioprinted hepatic constructs cause hypoxic conditions, which influence local pH and further hamper robust drug responses (Edmondson et al., 2014; Datta et al., 2020). These limitations were not sufficient to overcome bioink support and led to the development of another strategy in our model.

The major problem that we aimed to overcome in this study is the lack of sufficient supplementation of nutrients and oxygen, which

disturbs accurate drug metabolism. We introduced spinning conditions through the use of a rotatory platform shaker to 3D bio- printed hepatic constructs to exchange nutrients and oxygen efficiently and further extend the culture period. In our study, the HepG2 cell line, which has high proliferation capacity and consistent hepatic functionality, was chosen for encapsulation in bioink to represent the hepatocyte population in the parenchyma and achieve metabolic activity similar to that of the liver. Despite incompatible functionality compared to primary hepatocytes, HepG2 has advantages in easy accessibility, a long-term stable phenotype and strong survival rates during the bioprinting process. As reported previously, prolonged cultivation time of HepG2 cells rather than 3D culture contributed to increased drug metabolism (Luckert et al., 2017). As a result, bioprinted hepatic constructs cultivated under spinning conditions enable close representation of the in vivo state with reinforcement of clonogenic growth potential and functionality assessed by hepatic marker profiling and protein secretion levels.

Prior to modeling APAP-induced liver injury, we tested whether spinning conditions progress through the TGFβ-induced EMT pathway and whether this process is reversed by SB431542 treatment. Bioprinted hepatic constructs cultivated under spinning conditions showed breakdown of cell–cell interactions confirmed by TGFβ-induced EMT and reinforcement of drug sensitivity for hepatotoxicity based on gene level analysis and protein expression. This finding might be explained by mitigation of hypoxic conditions followed by rotation, which leads to reinforcement of chemically induced signals and drug-induced metabolism. Consequently, under spinning conditions, prolonged APAP treatment leads to enhanced hepatotoxicity by modulating the inflammatory response as well as autophagy and

apoptosis signaling and further causes necrosis in the encapsulated cells compared to static cells. In contrast, 3D bioprinted hepatic constructs with NAC under static conditions did not show a significant relative decline in apoptosis levels in contrast to spinning condi- tions, which is similar to that noted in a previous study (Manov et al., 2004). This finding indicates that under static conditions, bioprinted hepatic constructs show large spheroids that are less susceptible and are not subjected to apoptosis when exposed to drugs (Duval et al., 2017). Additionally, an extended culture period resulted in grape-like morphological changes that were responsible for poor cell–cell adhesion (Edmondson et al., 2014). Although short-term APAP-induced hepatotoxicity was not protected by administration of NAC regardless of culture conditions, spinning conditions enhanced the consistent APAP-induced hepatotoxicity effect in contrast to static conditions. Several studies evaluated continuous rotating effects mainly using perfusion to establish a more physiologically relevant in vitro 3D hepatic model (Jin et al., 2018; Jung et al., 2020). However, the major limitations of these systems include difficulties in standardizing and scaling up technology. Additionally, these systems require additional micropumps, tubes and valves to deliver drugs into the targeted area, which complicates the process of establishment (Wu et al., 2020).

Despite the encouraging application of our model for drug toxicity assessments, many factors should be considered in this study, i.e., restricted cell sources and the absence of exquisite design for representing liver anatomy in in vitro bioprinted hepatic constructs. Nevertheless, in particular, we recapitulated liver injury and repair phenom- ena, increasing susceptibility to acetaminophen toxicity and prevention by administration of N-acetylcysteine (NAC) in bioprinted hepatic constructs. It is difficult to represent complex liver regeneration

in vivo. In liver injury, hepatic regeneration responds to inflammatory cytokines, such as TNFα and IL-6 produced by Kupffer cells, to reconstitute the liver by rapidly inducing cells to enter the cell cycle (Kwon et al., 2015; Sanchez-Romero et al., 2019). Additionally, the absence of liver stem/progenitor cells, which contribute to liver regeneration, reveals the need for reinforcement in further studies (Roskams et al., 2003; Vig et al., 2006).

However, given that we encapsulated a single, representative cell type of liver in bioprinted hepatic constructs without sophisticated design, precise dynamic environmental effects can be evaluated in terms of maintaining the growth rate and functionality as well as metabolizing drugs. Based on these results, an ideal new generation in vitro model with multicellular organization can be established to parallel the main process responsible for pharmacokinetics and complete modeling of cell–cell interactions (Peng et al., 2016). Indeed, the cascade of immune responses from multiple cell types to injury leads to the development of a successful alternative method that enables the replacement of animal models (Sacchi et al., 2020). Further incorporation of the advanced development of robust human induced pluripotent stem cell (hiPSC) differentiation approaches is encouraging, and a patient-derived liver model can offer great potential for advancement of personalized disease modeling and medicine. This simple but efficient strategy will improve existing successful models for further in vitro research with simultaneous applications.

In conclusion, the successful combination of applied extrusion-based bioprinting technology with laminin-521-enriched biocompatible bioink facilitates the fabrication of a 3D in vitro model capable of supporting the structural integrity and tunability of mechanical properties in a precisely controlled manner. Bioengineered

hepatic constructs with controlled stiffness respond weakly to chemically induced microenvironmental signals and impair metabolic processes under static conditions, but these processes are improved upon the incorporation of a dynamic environment generated by an orbital shaker. The dynamic environment incorporated into these bioprinted hepatic constructs promotes a long-term culture period, resulting in enhanced functionality. Indeed, the dynamic environment replicates the complex in vivo microenvironment, including physiological and mechanical cues, permitting the study of induced fibrogenesis mechanisms at the cellular level and evaluation of the effects of drugs. Additionally, under spinning conditions, the increased number of existing healthy spheroids that play an important role in drug metabolism and the remarkable viability of encapsulated cells suggest that this combined strategy in bioprinted hepatic constructs can be utilized for accurate drug evaluation for hepatotoxicity prevention and induction. Indeed, enhancement of drug susceptibility verified by APAP-induced hepatotoxicity and alleviation by NAC administration through spinning conditions allowed the development of a novel culture system to study the human liver in the dish. Furthermore, this unique culture system will provide an excellent opportunity to scale up the advantages of 3D bioprinting technology with enhanced functionality and proliferation capacity compared to currently existing in vitro hepatic models. The combined application of 3D printing technology and subsequent spinning conditions improves the quality of 3D modeled tissue, is not resource-intensive and reduces labor costs and the need for reagents for further commercialization of the method in research applications and personalized medicine or cell therapy.

CHAPTER Ⅱ

Improved Hepatoblast Differentiation of Human Pluripotent Stem Cells by Coffee Bean Derived Graphene Quantum Dots

2.1 INTRODUCTION

Graphene quantum dots (GQDs), a graphene-based nanomaterial, have attracted wide attention in bio-applications fields, such as drug delivery systems (Iannazzo et al., 2017; Shang et al., 2014), tissue engineering 3D scaffolds (Park et al., 2021), biosensing (Sharma et al., 2022), and photodynamic agents (Das et al., 2021) due to their low toxicity, high dispersibility, and ease of functionalization (Tajik et al., 2020; Kim et al., 2018; He et al., 2015). Graphene-based nanomaterials are also known to effectively differentiate stem cells into various cell types by binding to various biomolecules such as DNA, protein, and small molecules, through complex physical and chemical interactions (Lee et al., 2011; Lv et al., 2015; Qiu et al., 2016; Yang et al., 2021; Yan et al., 2016). The mechanisms underlying the improved cell differentiation of graphene via biomolecule interaction, cell membrane interaction, and nano-topographical stiffness have been suggested (Luong et al., 2020). Despite the various suggested mechanism of graphene in differentiating stem cells into desired cell lineages, the role of graphene in the differentiation of human pluripotent stem cells (hPSCs) into the hepatic lineage has not been studied.

Hepatocytes are significantly used for hepatotoxicity drug screening, disease modelling, and cell therapy (Tasnim et al., 2015). Although many established protocols directly induce hepatocyte differentiation from hPSCs, sufficient amounts of hepatocyte-like cells are still difficult to obtain due to their variability and low differentiation efficiency (Hay et al., 2008; Kajiwara et al., 2012; Touboul et al., 2016). Calcium ions (Ca2+) play an important role in the regulation of cell proliferation and differentiation by altering the physical and chemical environment of living cells (Snoeck et al., 2020).

Extracellular calcium is known to have a significant role in the signalling pathway of the cell membrane via calcium ion channels of approximately 10^{-10} m in size in the phospholipid bilayer membrane; however, only a few studies have explored the relationship between calcium and cell surface receptors (Atkins et al., 1998). A greater understanding of how extracellular calcium impacts the niche or fate of stem cells would be valuable because of tissue-specific calcium gradients in skin and bones have been shown to alter stem cell and precursor cell functions (Dvorak et al., 2004; Zayzafoon et al., 2006; Hennings et al., 1980; Eckl et al., 1987).

Various methods for synthesizing GQDs have been consistently reported to date. In particular, methods were devised to replace the precursors of GQDs with natural substances and edible sources such as coffee beans, trees, and herbs due to its biocompatibility and doping effects. In 2021, our group successfully synthesized the coffee been derived graphene quantum dots (CB-GQDs) and showed similar effectiveness against abnormal α-synuclein fibrillation and the protection of neurons from relevant subcellular damages with low toxicity. The high biocompatibility and the feature of recycling coffee waste into therapeutics may minimize the psychological rejection by patients as well as lower the cost of medicine.

The present study confirmed that unlike carbon fiber-derived quantum dots (CF-GQDs), coffee bean derived graphene quantum dots, CB-GQDs, are inductive factors that are responsible for hepatoblast differentiation, with Ca^{2+} only found in CB-GQDs. Unlike conventional IGF1, the phosphorylation of CB-GQDs was concentration-dependent in the IGF1R-AKT pathway demonstrating that CB-GQDs can be independently used to induce hepatoblast differentiation without the use of additional growth factors. The chelated calcium of CB-GQDs forms

46

an electrostatic affinity with the phospholipid bilayer membrane, securing affinity and allowing for effective hepatoblast differentiation via the calcium channel. Compared with IGF1, the CB-GQDs are prepared using a cost-effective method and can be chemically stable at room temperature. Since CB-GQD treatment of hPSCs derived hepatoblasts upregulates maturation towards hepatocyte-like cells and downregulates the differentiation towards cholangiocytes, a large number of functional hepatocyte-like cells were ultimately acquired. To the best of our knowledge, this is the first report showing that calcium ions contained in CB-GQDs play an important role in promoting hepatoblast differentiation, suggesting that CB-GQDs are novel differentiation factors with independent bioactivity that can replace IGF1.

2.2 MATERIALS AND METHODS

2.2.1 GQDs synthesis

CF-GQDs and CB-GQDs were prepared following the previously reported synthesis methods (Kim et al., 2021; Peng et al., 2012). Coffee bean precursors were prepared in bulk by carbonizing coffee beans under at 1000 ℃ with 10 sccm H2 and 100 sccm Ar for 1 hour. Carbon fibers (99.999%) were finely chopped to increase the surface area to achieve a sufficient reaction. Each source materials, namely, carbonized coffee bean and carbon fibers, was mixed with sulfuric acid and nitric acid in a ratio of 3:1, heated to 100°C, and reacted for 1 day. CF-GQDs and CB-GQDs were prepared by diluting the reactants with tertiary deionized distilled water at a ratio of 10:1. The solution was dialyzed in a 1-killo Dalton molecular membrane bag (Thermo Fisher Scientific, Hampton, NH, USA) with continuous flowing DI water to remove exceramnss acid and discard unreacted ions.

2.2.2 Field emission-transmittance electron microscope

The FE-TEM sample was prepared by drop casting and drying 0.1 ml/mg GQD solution onto a monolayer graphene-encapsulated TEM grid. The samples were measured by FE-TEM (JEM-F200(TFEG) (JEOL Ltd, Japan)), and analysed by the ImageJ program. Atomic force microscope analysis. The GQD samples were spin-coated on SiO2 wafers and measured by Multimode 8 (Bruker, US) in noncontact mode at a scan rate of 0.5 Hz.

2.2.3 Atomic force microscope analysis

The GQD samples were spin-coated on SiO2 wafers and measured by Multimode 8 (Bruker, US) in noncontact mode at a scan rate of 0.5 Hz.

2.2.4 Raman spectroscopy

The fully dried CF- and CB- GQD powder was obtained by rotary evaporation and kept in a vacuum desiccator for 3 days to further prevent undesirable contamination. Raman spectroscopy (Renishaw, Gloucestershire, UK) was performed with a 514 nm Ar laser at room temperature.

2.2.5 FT-IR

GQD powder was prepared using the same method as for Raman analysis. The spectra were measured by the conventional K-Br pellet method (FT-IR 4600LE, JACOS, Tokyo, Japan)

2.2.6 X-ray photoelectron spectroscopy

The GQD powder was prepared by the same method as for Raman analysis. The binding energy in the full range was measured by XPS (AXIS-HSi, KRATOS, Shimadzu, Japan).

2.2.7 Zeta potential

The GQD solution (50 ug/ml) was filtered with a 200-nm syringe filter and measured by a Zetasizer Nano ZS (Malvern Instruments Ltd, Malvern, UK).

2.2.8 Cell culture

All experiments were carried out in accordance with the approved guidelines of the Seoul National University Institutional

Review Board (IRB no. 2109/001-018). Three hESC lines and three hiPSC lines were used. We labelled the SNUES3, SNUES4, and SNUES31 cell lines received from the Korea Centres for Disease Control and Prevention (KCDC) as hESC1, hESC2, and hESC3, respectively. For the KSB-iPSC1 and KSB-iPSC2 lines previously generated by our lab (Kwon et al., 2020), we labelled them as hiPSC1 and hiPSC2, respectively. Additionally, we named the FmiPSC2 line provided by the National Stem Cell Bank as hiPSC3.

2.2.9 Hepatocyte differentiation

Hepatic differentiation was performed using previously described protocols (Ferrari et al., 2000). Human PSCs were maintained on mitomycin C-treated mouse embryonic fibroblast (MEF) feeder cells in DMEM/F12 (Gibco, 11320082) supplemented with 4 ng/ml recombinant human basic fibroblast growth factor (bFGF; Gibco, PHG0261). For definitive endoderm differentiation, PSCs were seeded on Matrigel-coated dishes in RPMI 1640 (Gibco, GIB-22400-089) supplemented with 1 x B27 (Gibco, GIB-17504-044) and 100 ng/ml human activin A (Peprotech, 120-14E) for 5-6 days. For hepatic endoderm differentiation, the medium was exchanged with RPMI 1640 supplemented with 1 x B27, 10 ng/ml bFGF and 20 ng/ml BMP4 (Peprotech, 120-05ET). To culture hPSC-derived hepatoblasts, the cells were passaged every 5 days and the medium was replaced with DMEM/F12 supplemented with 10% FBS, 1 x insulin transferrin selenium (Thermo Fisher, 41400045), 20 ng/ml human HGF (Peprotech, 100-39H), 10 ng/ml human EGF (Peprotech, AF-100-15), 5 μM Y-27632 (Cayman, A60200) and 5 μM A83-01 (Peprotech, 9094360). To induce hepatic maturation of hPSC-derived hepatoblasts, confluent cells were incubated in RPMI 1640 supplemented with 1 x B27, 10

ng/ml Oncostatin M (Peprotech, 300-10), and 1 x 10-4 M dexamethasone (Sigma, D4902) for 10 days. For cholangiocyte differentiation (Kido et al., 2015), at a density of 1 x 105 cells were collected and resuspended in a gel made up of a 2:3 mixture of growth factor reduced Matrigel (Corning) and collagen type I (Nitta Gelatine). The cell suspensions were then placed in a 24-well plate (Corning) and incubated at 37 ℃ for 2 hours until solidification. For the next 7 days, the cells were grown in the presence of R-spondin-1 (40 ng/ml) and WNT-3a (40 ng/ml) (Peprotech).

2.2.10 Quantitative RT-PCT

Total RNA was extracted using TRIzol (Invitrogen, BRL-15596-018) according to the manufacturer's suggestion. SYBR Green PCR Master Mix (Applied Biosystems, 4309155) and QuantStudio3 (Biosystems) were used to extracted RNA, which was detected using the real-time qPCR (Biosystems). GAPDH was used to standardize the expression levels of each gene. For each gene, at least three independent analyses were performed. Quantstudio Design and Analysis software v1.4 was used to examine the results.

2.2.11 Immunocytochemistry

Hepatoblast, hepatocyte-like cells, and cholangiocytes from human pluripotent stem cells (hPSCs) were fixed with 4% paraformaldehyde (PFA) at room temperature for 10 minutes, permeabilized with 0.03% Triton X-100 solution for 10 minutes, and blocked with 5% normal goat serum (Vector Laboratories, K-S-10000-K13) for an hour at room temperature. The cells were incubated overnight at 4 ℃ with relevant primary antibodies at 1:100 dilution. Alexa Fluor mouse 488 (Invitrogen, A1100) and Alexa Fluor

rabbit 555 (Invitrogen, A-21428) secondary antibodie were applied at a 1:1000 dilution for an hour at room temperature. After washing, fluorescent staining with DAPI solution at 1:1000 in PBS was used to detect nuclei. A confocal microscope was used to take the images (Nikon, Eclipse TE200, Tokyo, Japan)

2.2.12 Periodic Acid-Schiff (PAS) staining

The PAS stain Kit (abcam, ab150680) was used to identify intracellular glycogen in paraffin-sectioned tissues according to manufacturer's instructions.

2.2.13 Oil Red O staining and Indocyanine green (ICG) uptake

Oil Red O staining was used to detect fat droplets in the differentiated hPSC-derived hepatocyte-like cells to confirm their functioning. Cells were fixed for 1 hour with 4% PFA and then washed with 60% isopropanol before being incubated for 10 minutes in freshly diluted Oil Red O. To detect ICG (Sigma-Aldrich, I2633) uptake, cells were incubated for 30 min at 37 ℃ in media containing 1mg/ml ICG and observed under phase-contrast microscope.

2.2.14 MTT assay

The proliferative ability of hPSC-hepatoblasts was measured using the 3-(4,5-dimethylthiazol-2-yl)-2,5-diphenyltetrazolium bromide (MTT) (Sigma-Aldrich, St. Louis, USA) assay as previously described (Lee et al., 2016).

2.2.15 Functional analysis

According to the manufacturer's instructions, the amount of secreted human albumin and urea from the collected cell supernatant

was measured using a Human Albumin ELISA Quantification Kit (Bethyl Laboratories, E80-129) and QuantiChrom™ Urea Assay Kit (Bioassay system, DIUR-100) (Kang et al., 2021).

2.2.16 Western-blot analysis

A Pierce^{TM} BCA Protein Assay Kit (Thermo Scientific, 23227) was used to determine the protein content. Approximately 10 μg of protein from each cell was subjected to 8% to 15% sodium dodecyl sulfate polyacrylamide gel electrophoresis and then transferred onto a nitrocellulose membrane. After bloking the membranes with a 3% bovine serum albumin solution in TBST, they were incubated for 1 hour. The membrane was then incubated with primary antibody overnight at 4 ℃. The following were the primary antibodies used to probe each protein: rabbit anti-phospho-IGF1R (Abcam, ab39398):1:1000, rabbit anti-IGF1R (Abcam, 131476): 1:1000, rabbit anti-phospho-AKT (Cell signaling, 9271S): 1:1000, rabbit anti-AKT (Cell signalling, 9272S): 1:1000, rabbit anti-phospho-ERK MAPK (Cell signaling, 4370S): 1:1000, rabbit anti-ERK MAPK (Cell signaling, 4695S): 1:1000, anti-phopho-JNK (Cell signaling, 9251S): 1:1000, rabbit anti-JNK (Cell signaling, 9252S): 1:1000, rabbit anti-phospho p38 (Cell signaling, 9211S): 1:1000, rabbit anti-p38 MAPK (Cell signaling, 9212S): 1:1000, mouse anti-β-actin (Cell signaling, 4967): 1:1000, rabbit anti-albumin (Genetex, 102419) : 1:1000, rabbit anti-Alpha-fetoprotein (DAKO, A0008): 1:1000, mouse anti-cytokeratin 19 (Santa Cruz, sc-6278): 1:1000, rabbit anti-EpCAM (Abcam, ab71916): 1:1000. Secondary horseradish peroxidase (HRP)-conjugated antibodies (Invitrogen, G21040, G21234): 1:2000. Antibody binding was detected using an enhanced chemiluminescene (ECL) detection kit (GE Healthcare Life Science, RPN2106).

2.2.17 Flow cytometry

To confirm the expression of hepatocyte markers, hPSC-derived hepatoblasts and hepatocyte-like cells were stained with a fluorochrome-conjugated antibody and further analysed. After cell surface staining, the cells were stained with antibodies against intracellular protein, as necessary. For intracellular staining, we used a transcription factor buffer set (BD Biosciences, #562725) according to the manufacturer's instructions. Briefly, the cells were fixed with 1x Fix/Perm Buffer and permeabilized with 1x Perm/Wash Buffer. The following antibodies were used: mouse IgG1-fluorescein isothiocyanate (FITC) - isotype control (Miltenyi Biotec, 130-113-199), mouse IgG1-phycoerythrin (PE) - isotype control (BD science BD559320), mouse IgG2A allophycocyanin (APC) - isotype control (R&D, IC003A), fluorescein isothiocyanate (FITC)-conjugated anti-human cytokeratin 18 (Miltenyi Biotec, 130-080-101), allophycocyanin (APC)-conjugated anti-human serum albumin (R&D, IC1455A), phycoerythrin (PE)-conjugated asialoglycoprotein receptor 1 (ASGR1) (BD Bioscience, BD563655). Fluorescence was detected with a FACSCalibur flow cytometer and evaluated using Cell Quest software (BD Bioscience).

2.2.18 Statistical analysis

Statistical analyses were performed using GraphPad Prism version 9 software. In addition, the data are presented as representative examples or mean values when more than three experiments were conducted. Data are presented as the means $\pm$ S.D. A two-tailed Student's t-test was performed to compare the data from two groups, or a one-way ANOVA followed by Bonferroni's test was performed to compare data from multiple groups throughout the experiments.

2.3 RESULTS

2.3.1 Physical and chemical characterizations of CB-and CF-GQDs

Among the natural sources of GQDs, coffee in particular can be a promising source to acquire GQDs due to its higher carbon content than other biomass types, including coffee beans, trees, and herbs (Table S1) (Abbas et al., 2018). In this regard, we previously reported an approach for synthesizing GQDs through abundant waste-to-treasure methods, e.g., from coffee waste to nano drugs (Kim et al., 2021). To separate carbon fiber-GQDs (CF-GQDs) and coffee bean-GQDs (CB-GQDs), carbon fiber and carbonized coffee bean precursors were synthesized as previously reported (Kim et al., 2021; Peng et al., 2012). Fine carbon fibers were prepared, and precursors derived from coffee beans were prepared by carbonization process in hydrogen and argon atmosphere at 1000°C for 1 hour. CF-GQDs and CB-GQDs were synthesized using a thermo-oxidative cutting method in sulfuric acid and nitric acid solutions (3:1) at 100°C for 24 hours. The end product was obtained after the dialysis and purification process using continuously flowing DI water to neutralize excess acids and to discard unreacted ions (Figure 12 (a)). To analyze the size distributions, the properties of as-prepared CF- and CB-GQDs were measured analyzed with transmission electron microscopy (TEM), atomic force microscopy (AFM), Raman spectroscopy and Fourier transform infrared (FT-IR) spectroscopy. The average lateral sizes of the CF- and CB-GQDs were 2.64 ± 0.24 nm and 3.02 ± 0.70 nm, and the average height was 1.37 ± 0.22 nm and 2.03 ± 0.39 nm, respectively, as confirmed by TEM and AFM (Figure 12 (b)–(c)). The average size of the CB-GQDs were 0.4 to 1 nm larger than that of the CF-GQDs in terms of the size distribution (Figure 12 (b)).

The optical properties of CB-GQDs were analyzed by Raman and Fourier-transform infrared (FT-IR) spectroscopy analyses. The Raman spectrum showed characteristic D and G bands at 1380 and 1595 cm^{-1}, showing a high-intensity spectrum from the bond stretching modes in the graphene atomic structure (Ferrari et al., 2000; Ferrari et al., 2013) (Figure 12 (d)). The edge functional groups were studied based on the FT-IR spectrum, and they exhibited abundant groups rich in carbon-oxygen bonds, such as carboxyl and hydroxyl groups (Kido et al., 2015) (Figure 12 (e)). Due to the rich oxygen functional groups, the CF-GQDs and CB-GQDs were well dispersed for up to 6 months at room temperature (Figure 13 (a)–(b)).

Table 1. Comparative table to the synthesis method, maximum excitation wavelength, maximum emission wavelength, PL color, and applications of the GQDs with the recently reported studies.

		Synthesis Method	Maximum Excitation Wavelength	Maximum Emission Wavelength	PL color	Applications
1	Coffee bean compounds (This study)	Chemical synthesis (H_2SO_4, HNO_3) + Carbonization	400 nm	490 nm, 535 nm	Yellow green	Cell differentiation Nano drugs Bio imaging
2	Carbon fiber (J. Peng et. al.)	Chemical synthesis (H_2SO_4, HNO_3)	370 nm	480 nm, 540 nm	Yellow	Bioimaging Protein analysis Cell tracking Isolation of biomolecules
3	Rice husk (Abbas A. et. al.)	Pyrolysis + Hydrothermal treatment	280 nm	380 nm, 410 nm	Green	Photocatalysis Optoelectronics Biomedicines Drug delivery
4	Herbal plants (N. Sharma et. al.)	Microwave	280 nm	350 nm, 450 nm	Green	Photocatalysis Optoelectronics Biomedicines Thin-film displays
5	Spent tea (Abbas A. et. al.)	Pyrolysis + Microwave	340 nm	500 – 530 nm	Light green	Selective detection of Fe3+ ions
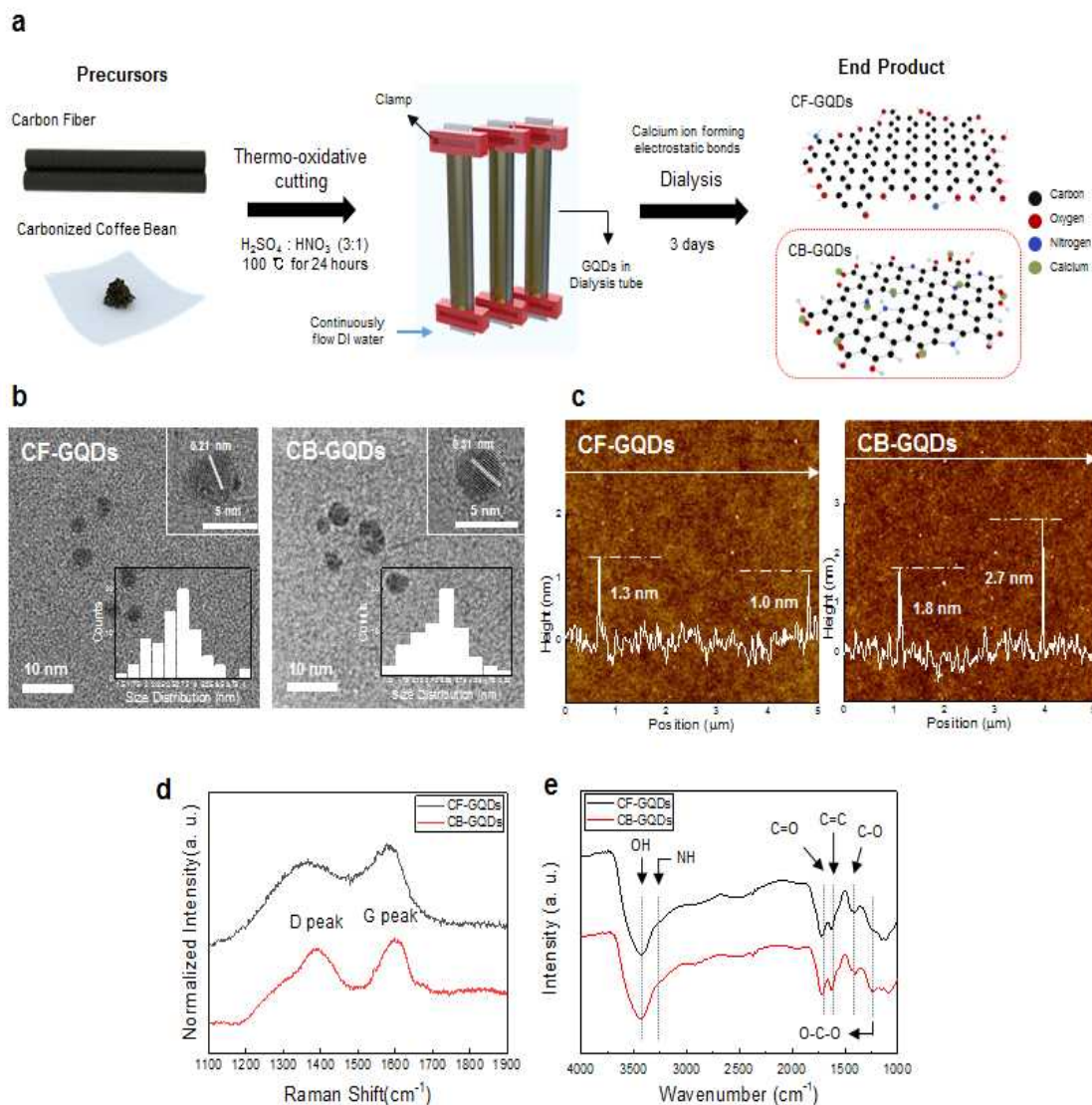
Figure 12. Characterization of CF- and CB-GQDs.

a) Schematic diagram of the GQDs synthesis derived from carbon fiber and coffee bean, respectively. b) Representative TEM images and size distribution graph of CF- and CB-GQDs with interlayer spacing distance on a graphene TEM grid. (scale bar: 10 nm, inset (5 nm)) c) Atomic force microscope images of CF- and CB- GQDs with its height graph. d)-e), Analysis of Raman spectra and Fourier transform infrared (FT-IR) graph after CF- and CB-GQDs synthesis.
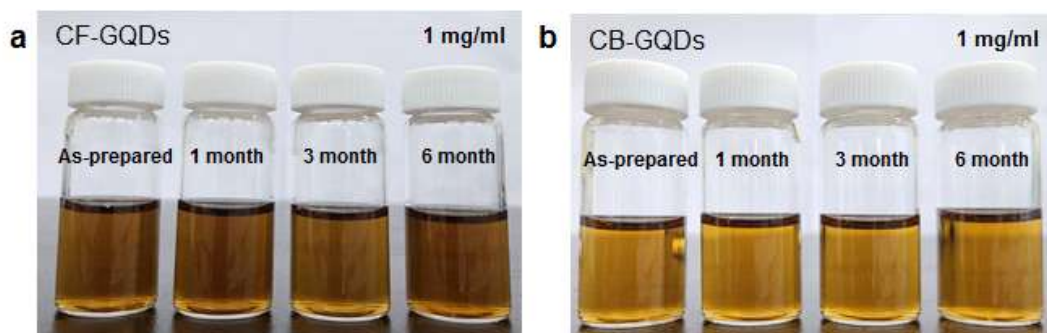
Figure 13. Characterization of CF- and CB-GQDs.

a) Schematic diagram of the GQDs synthesis derived from carbon fiber and coffee bean, respectively. b) Representative TEM images and size distribution graph of CF- and CB-GQDs with interlayer spacing distance on a graphene TEM grid. (scale bar: 10 nm, inset (5 nm)) c) Atomic force microscope images of CF- and CB- GQDs with its height graph. d)-e), Analysis of Raman spectra and Fourier transform infrared (FT-IR) graph after CF- and CB-GQDs synthesis.

2.3.2 Correlation with hepatoblast differentiation rate in the presence or absence of calcium

To understand the further chemical binding of CF and CB-GQDs, x-ray photoelectron spectroscopy (XPS) was carried out. The XPS survey spectrum indicates that both the CF- and CB-GQDs show the presence of typical carbon, oxygen, and nitrogen atoms, with major peaks at C-C 283.1 eV, C-O 529.9 eV, C-N 399.7 eV (Zhang et al., 2016). Since calcium did not diffuse throughout during the GQD synthesis process due to electrostatic interactions between calcium ions and CB-GQDs, the distinguishable calcium atom peaks (Ca2p: 346.0 eV, Ca2s: 437.0 eV) in the CB-GQDs were determined based on the intrinsic composition originating from coffee beans (Figure 14 (a) and Figure 15). A comparision of the atomic ratio of CF- and CB-GQDs showed that the O/C ratio increased to 0.6847 from 0.3973 and the N/C ratio increased to 0.0586 from 0.0116; however, the Ca/C ratio of 0.2727 was only monitored in the CB-GQDs (Figure 14 (b)). The zeta potential of the CB-GQDs was -21.4 mV, while that of the CF-GQDs was -23.48mV. The value of CB-GQDs was 8.9% higher due to chelation of calcium ions with oxygen and nitrogen bonds neutralization of the charges by nitrogen bonds to induce a higher zeta-potential (Figure 14 (c)). After stage-specific differentiation based on a previous report (Takebe et al., 2013) using human pluripotent stem cells (Figure 16 (a)-(b)), we investigated the potential roles of CF-GQDs and CB-GQDs in elevating hepatoblast differentiation rates to obtain a large number of hepatoblasts (Figure 16 (a)). The CB-GQDs showed higher viability than the CF-GQDs when treated at the same concentration using the MTT assay (Figure 16 (b)), and the results corresponded to the high nitrogen content and oxygen atomic ratio data (Figure 14 (b)). Further experiments were carried out with 5 μg/ml CF- and CB-GQDs.

After 15 days, the CK18 and ALB double-positive cells in the absence of the CB-GQDs averaged approximately 20% in three human embryonic stem cells and three induced pluripotent stem cells (Figure 18 (a)-(f)). Hepatoblast differentiation was strongly induced approximately twice on average for the CB-GQD treatment but was reduced for the CF-GQDs treatment, as confirmed by the gene expression, immunostaining, and flow cytometry results (Figure 16 (c)-(f) and Figure 17 (d)-(f)). The enhancement of hepatoblast efficiency persisted for up to 35 days (Figure 17 (c)), thus demonstrating that the CB-GQDs were highly biocompatible stimulants to hepatoblasts over a long period of cultivation. Based on the XPS spectrum (Figure 14 (a)), the calcium content was observed solely in CB-GQDs, and such findings imply a correlation between the presence of calcium and hepatoblast differentiation.
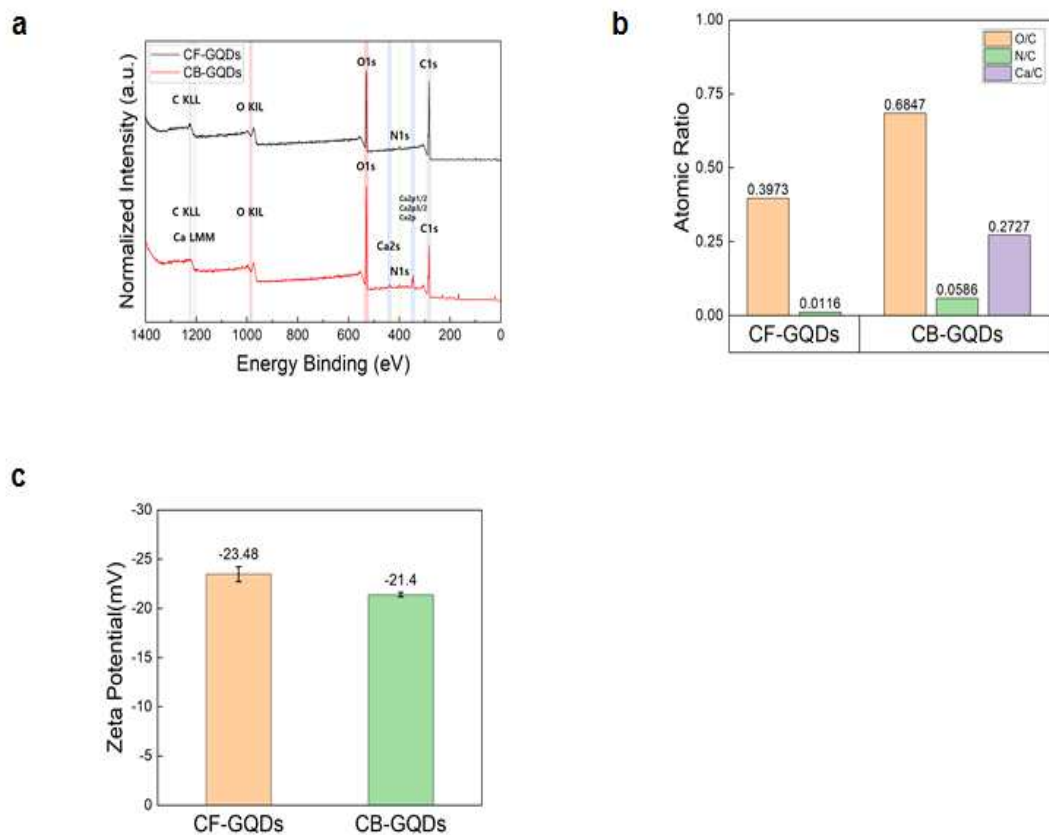
Figure 14. Atomic atomic characterization of CF- and CB-GQDs
a) XPS survey spectrum of CF- and CB-GQDs showing different atomic components. b) The ratio of the elements constituting CF- and CB-GQDs divided by carbon. c) Zeta potential of CF- and CB-GQDs (Data are means ± S.D., which are 0.768 and 0.218, respectively).
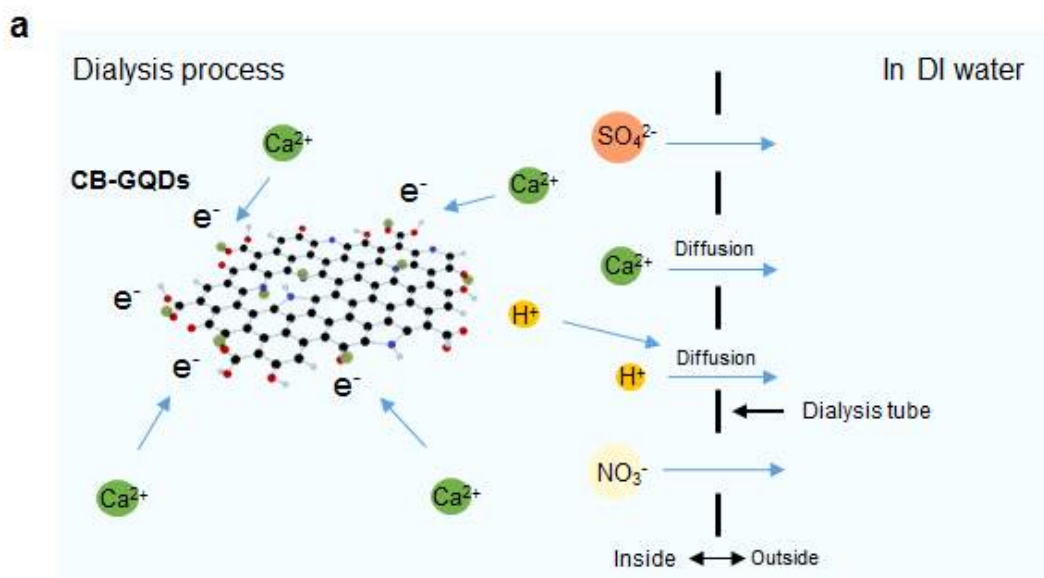
Figure 15. The schematic diagram explains the dialysis process to remove undesirable ions and unreacted impurities post GQDs synthesis. The other calcium ions remained in the dialysis membrane without diffusing out of the dialysis membrane due to the electrostatic attraction between CB-GQDs and calcium ions.
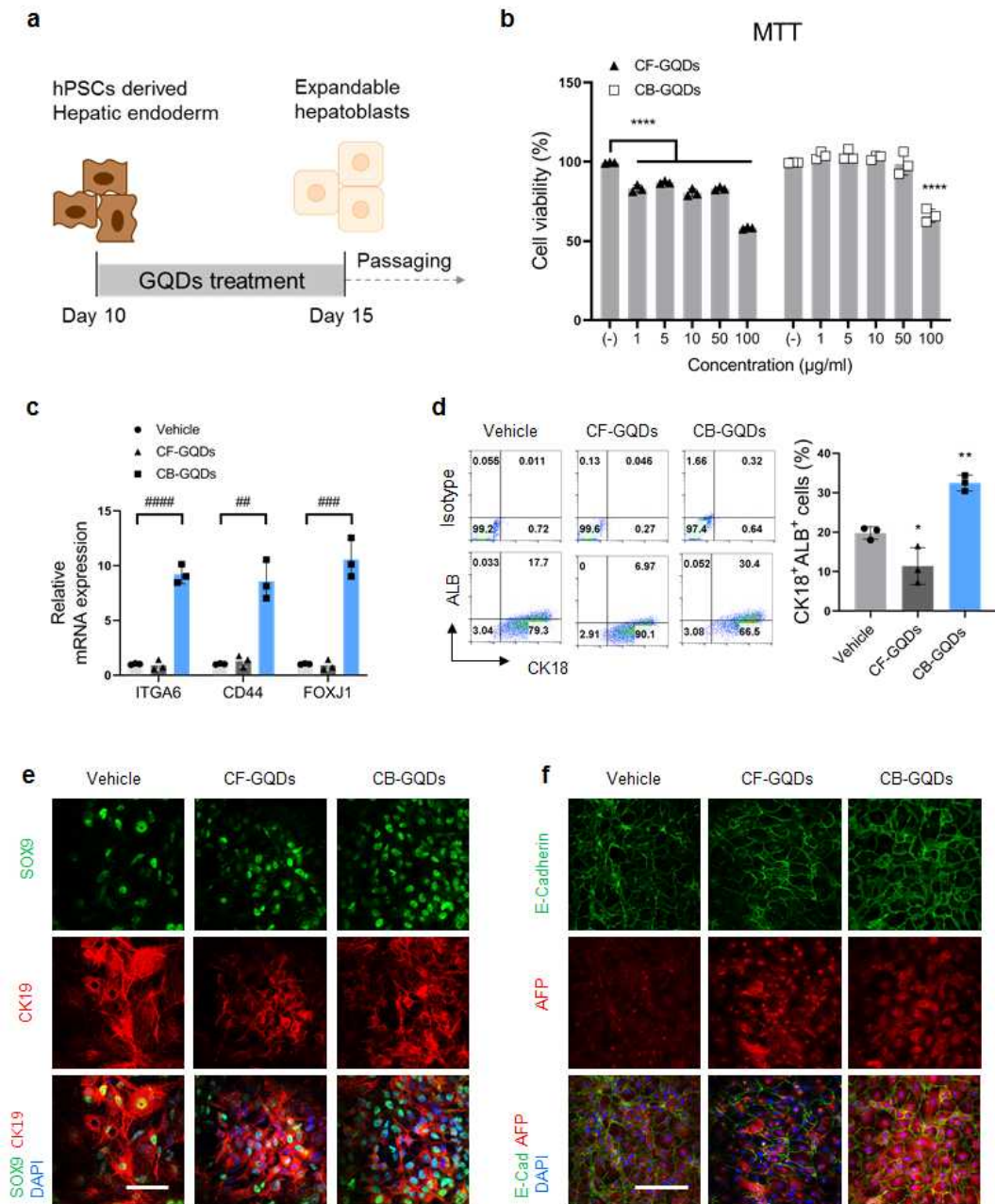
Figure 16. CB-GQDs supplemention in supplemention in hepatoblast medium increases the efficiency of hepatoblast differentiation in hPSC derived hepatic endoderm cells.

a) Schematic illustration for differentiation of hPSC-derived hepatic endoderm cells treated with CB-GQDs into hepatoblasts. The hepatoblast medium supplemented by CB-GQDs was changed every other day and

expanded until passage 5 with the expression of hepatoblast markers. The expanded hepatoblasts were passaged every 5 days. b) Cytotoxicity assessment of various CB-GQDs concentration on hepatoblasts compared to untreated control by MTT assay. **$p < 0.01$, ****$p < 0.0001$. c) Quantification of hepatoblast marker genes expression by qRT-PCR analysis. ##$p < 0.01$, ###$p < 0.001$ and ####$p < 0.0001$. d) Quantification for differentiation of hPSC lines into hepatoblasts treated without GQDs, with CB-GQDs and CF-GQDs. The percentage of CK18 and ALB double-positive cells was quantified by flow cytometry. *$p < 0.05$ and **$p < 0.01$ denote significance compared to vehicle control. e)-f) Representative double immunofluorescence images for hepatoblast markers e) SOX9 (green)/CK19 (red), f) E-cadherin (green)/AFP (red). hHBs were cultured in hepatoblast medium supplemented by CF-GQDs and CB-GQDs, vehicle control represents hepatoblast medium without CB-GQDs. Nuclei were counterstained with DAPI (blue). e) Scale bar, 250 µm; f), Scale bar, 100 µm. Data are means ±S.D. b, c, d, n=3 biologically independent samples b), c), d). One-way ANOVA followed by Bonferroni post hoc analysis.
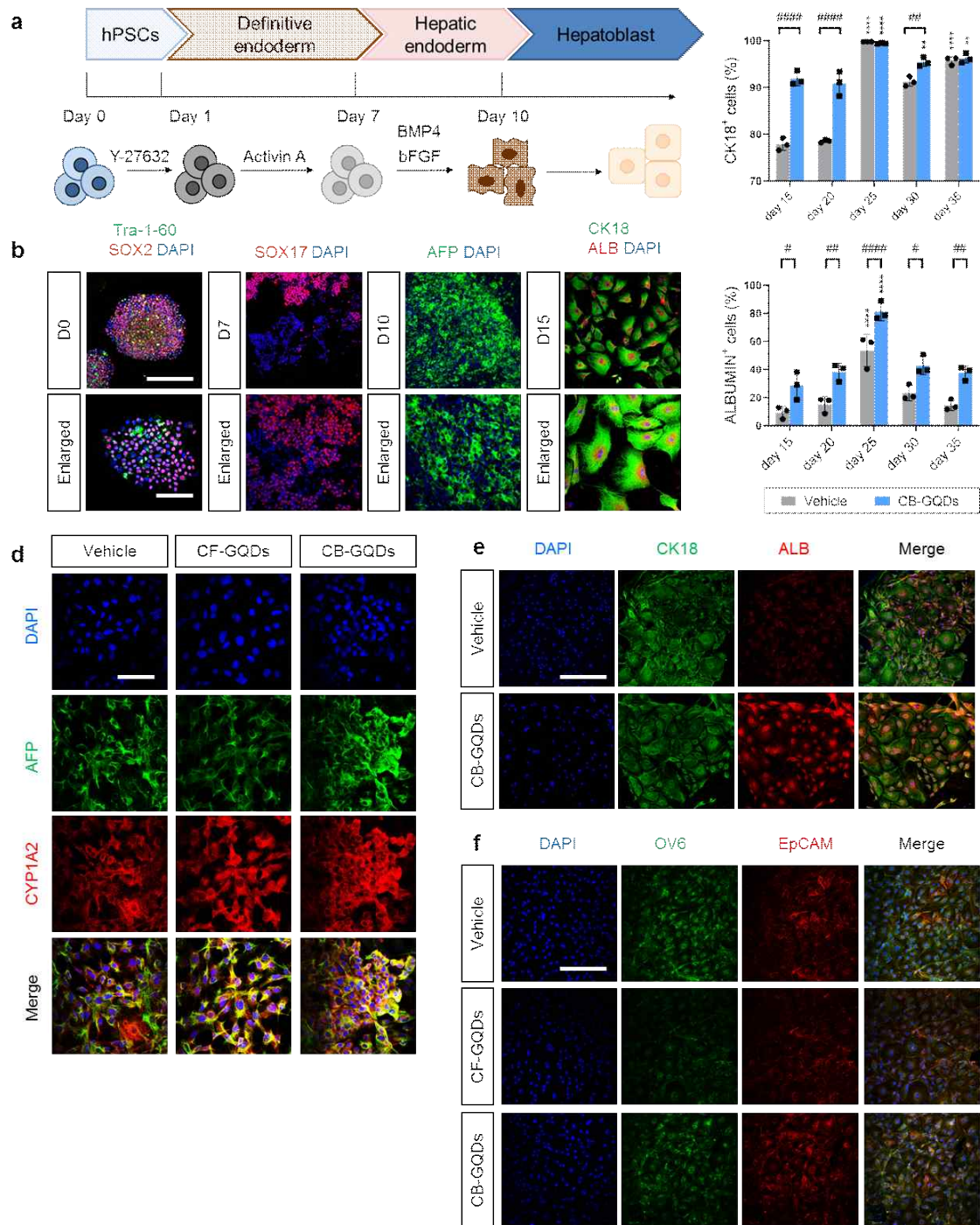
Figure 17. Directed differentiation of human PSCs into hepatic endoderm cells.

a) Schematic illustration of the protocol to differentiate hPSCs into hepatoblasts. Establishment of stage 2 differentiation conditions: Induction of hepatic endoderm cells from definitive endoderm cells. b) Immunostaining of Tra-1-60, SOX2, SOX17, AFP, CK18, and ALB. Scale bar, 250 μm. c) Quantification of CK18 positive, ALBUMIN positive cells with or without CB-GQDs during 35 days. $**p < 0.01$ and $****p < 0.0001$ represent significance between control and each group under indicated time for indicated proteins expression. $\#\#p < 0.01$ and $\#\#\#\#p < 0.0001$. d,) Representative images of immunofluorescence staining for hepatoblast markers, AFP (green)/CYP1A2 (red), Scale bar, 100 μm, e) CK18 (green)/ALB (red), 250 μm, f, SOX9 (green)/CK19(red), Scale bar, 100 μm. Nuclei were counterstained with DAPI (blue).
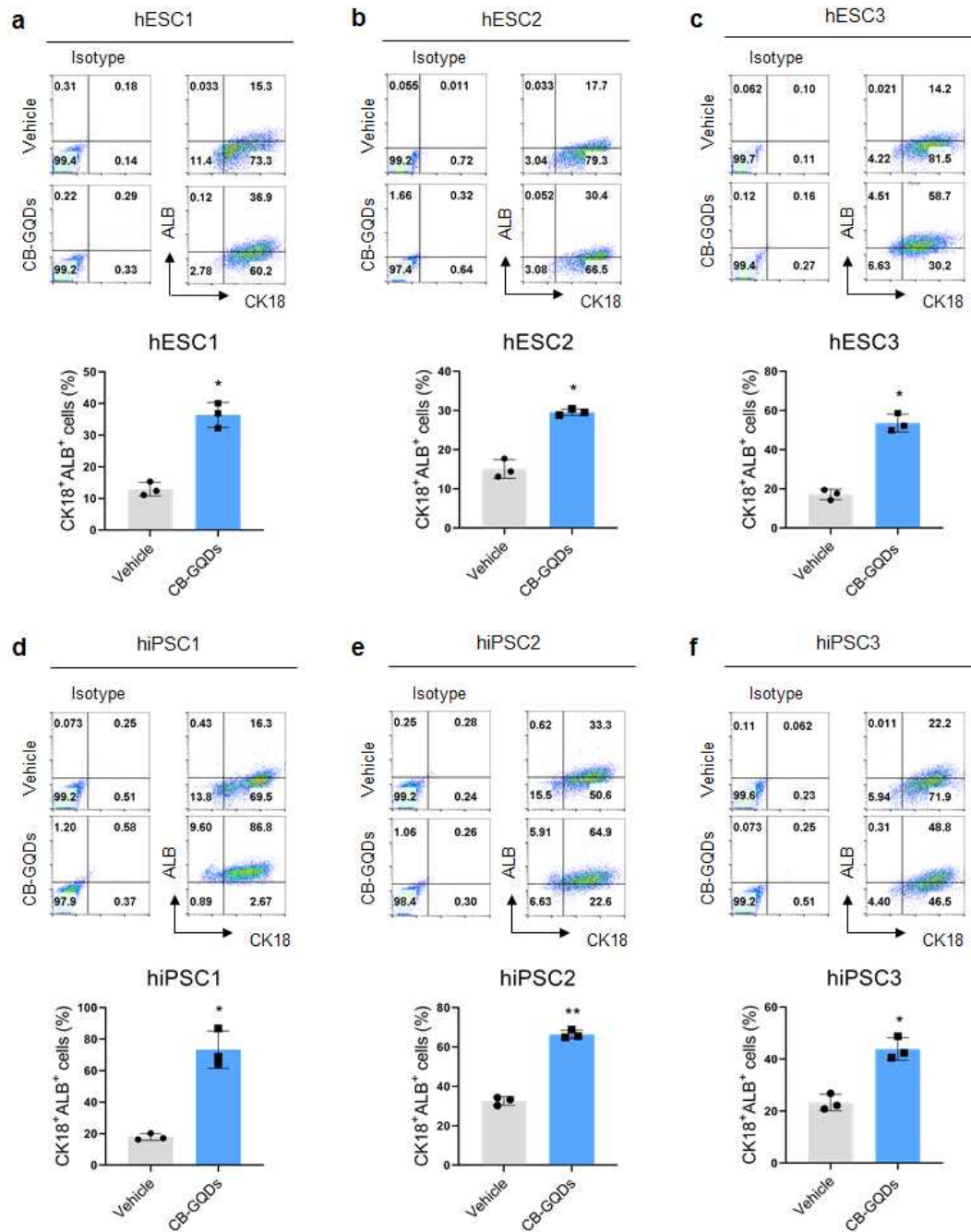
Figure 18. The effect of improving hepatoblast differentiation of CB-GQDs identified in three human embryonic stem cells (hESCs) and three induced pluripotent stem cells (hiPSCs).

a)-f) Quantification of CK18 and ALBUMIN double-positive cells with or without CB-GQDs using flow cytometry analyses, Error bars

represent the means ± S.D. from three separate experiments. Data analyzed by two-tailed t-test, *p < 0.05 and **p < 0.01 represent significance of CB-GQDs treatment. Data are means ±S.D. n=3 biologically independent samples. Two-tailed t-test.

2.3.3 CB-GQDs treatment of hPSCs derived hepatoblasts upregulated the maturation toward hepatocyte-like cells and downregulated the differentiation toward cholangiocytes

Expandable hepatoblasts (HBs), which are also known as liver progenitor cells, can be differentiated into hepatocyte-like cells and cholangiocytes, which are bile duct epithelial cells (Kido et al., 2015; Wu et al., 2019; Wang et al., 2019). Hepatocyte differentiation was induced for 10 days under previously reported liver maturation medium conditions (Woo et al., 2012) to determine whether CB-GQDs regulate the differentiation bipotential in HBs, and the functionality and maturation of hepatocyte-like cells were confirmed (Figure 19 (a)). Hepatocyte-like cells generated from pluripotent stem cells are recognized to have immature characteristics and low functionality compared to human hepatocytes, which represents a challenge to overcome (Peters et al., 2016; Li et al., 2019; Goldman et al., 2016). The mRNA expression of hepatocyte maturation markers significantly increased after the CB-GQD treatment (Figure 19 (b)). This treatment boosted the expression of ZO-1 and MRP2, which are abundant in the bile canaliculi (Figure 19 (d)), as well as the expression of ASGR1, which is rarely seen in immature hepatocytes, as confirmed in three human embryonic stem cells and three human induced pluripotent stem cells (Figure 19 (c) and Figure 21 (a)-(f)). Furthermore, improvements in hepatocyte functions, such as glycogen accumulation, ICG secretion, lipid deposition (Figure 19 (d)), albumin secretion (Figure 19 (e)), and urea synthesis (Figure 19 (f)), were also shown. Figure 20 (a) describes the schematic illustration for the effect of CB-GQD in cholangiocyte differentiation. For cholangiocyte differentiation, the vehicle negative control groups possessed cyst-like morphological characteristics (Figure 20 (b)) and expressed the cholangiocyte markers CK19, ZO-1, AQP1, and integrin β4, as confirmed by immunostaining (Figure 20 (c)-(d)). In contrast, the CB-GQD treatment decreased *NOTCH* signaling (Figure 20 (f)) and cholangiocyte marker expression (Figure 20 (e)) and led to cholangiocyte differentiation but not cholangiocyte generation.

Based on these results, CB-GQDs can interact with growth factor signals in the medium to promote or reduce specific lineage differentiation in a complementary manner when they are added to the medium. Thus, the potential independent and complementary roles of growth factors must be determined. Growth factors are proteins involved in the differentiation and proliferation of stem cells, and they are routinely used in cellular biology and biomedical applications. The combination of these growth factors with specific receptors acts as signalling factors in cells. Previous studies (Qiu et al., 2016; Yang et al., 2021; Ku et al., 2021) that correlated the differentiation rates using GQDs potentially showed that GQDs can be used as a substrate to trigger different signals in cells and biomolecules. In many papers, the effects of graphene have been intensively explored (Lee et al., 2011; Chen et al., 2012), although the mechanaisms underlying the ability of graphene-related materials to induce these biomedical effects have yet to be clearly explained. Furthermore, systematic reviews of the interaction between graphene and biological systems at the cellular level are lacking. Given that the major signalling pathways that control human growth and development are based on a combination of multiple pathways at different levels, the effects and signals of graphene and its derivatives need to be investigated first through the development of mammalian cells in vitro (Vert et al., 2011; Liao et al., 2018).

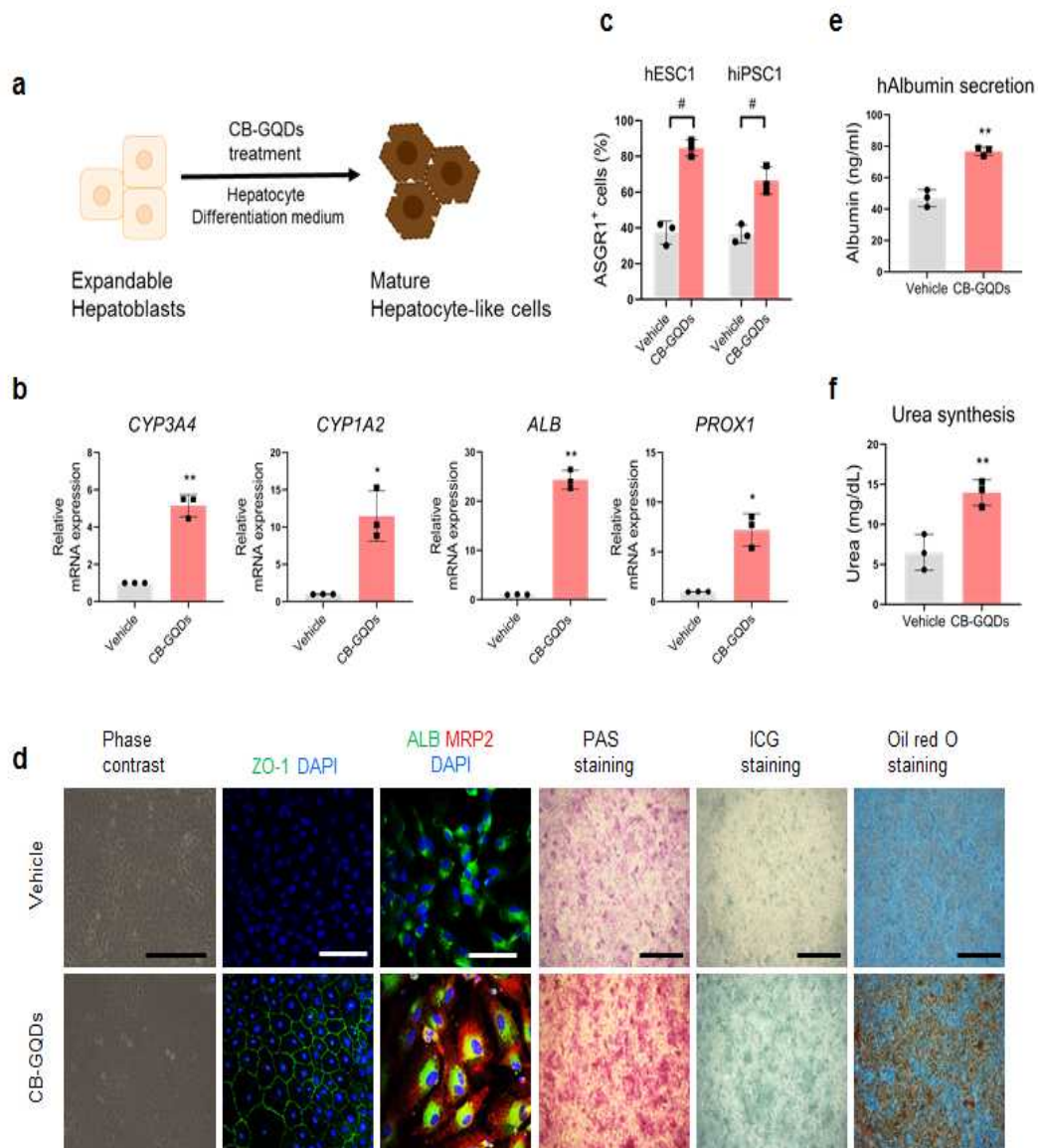**Figure 19. CB-GQDs treatment increases maturation and functionality of hepatocyte-like cells in hepatocyte differentiation medium.**

a) Schematic diagram of hepatoblasts differentiation potential treated with CB-GQDs in hepatocyte differentiation medium. b) Quantification of hepatocyte-specific marker genes expression quantitative RT-PCR (RT-qPCR) analysis. GAPDH was used as an internal control for

RT-qPCR. *p < 0.05 and **p < 0.01. c) Quantification of ASGR1-positive cells in two indicated hPSC lines by flow cytometry analysis. Bar graph represents the results of Supplementary figure 3A, 3D showing each value of ASGR1-positive cells. #p < 0.05. d) Representative images for phase-contrast microscopy and immunofluorescence staining of hHB-HLCs with mature hepatocytes characteristics. Phase contrast images, Scale bar, 250 μm. Double immunofluorescence staining for mature hepatocyte markers ZO-1 (green) and ALB (green)/MRP2 (red); nuclei were counterstained with DAPI (blue), Scale bar, 100 μm. Representative images for Periodic Acid Schiff (PAS), Indocyanine green (ICG) and Oil red O staining demonstrating enhancement of hepatocyte-specific functionality by CB-GQDs treatment, Scale bar, 1000 μm. e) Quantification of human albumin secretion and f) urea synthesis level in culture media supplemented with or without CB-GQDs. 1×10^{6} cells were seeded and culture media was collected after 48 hours. *p < 0.05 and **p < 0.01. Data are means ± S.D. b), c), e), f), n=3 biologically independent samples. b), c), e), f). Two-tailed t-test b), c), e), f)
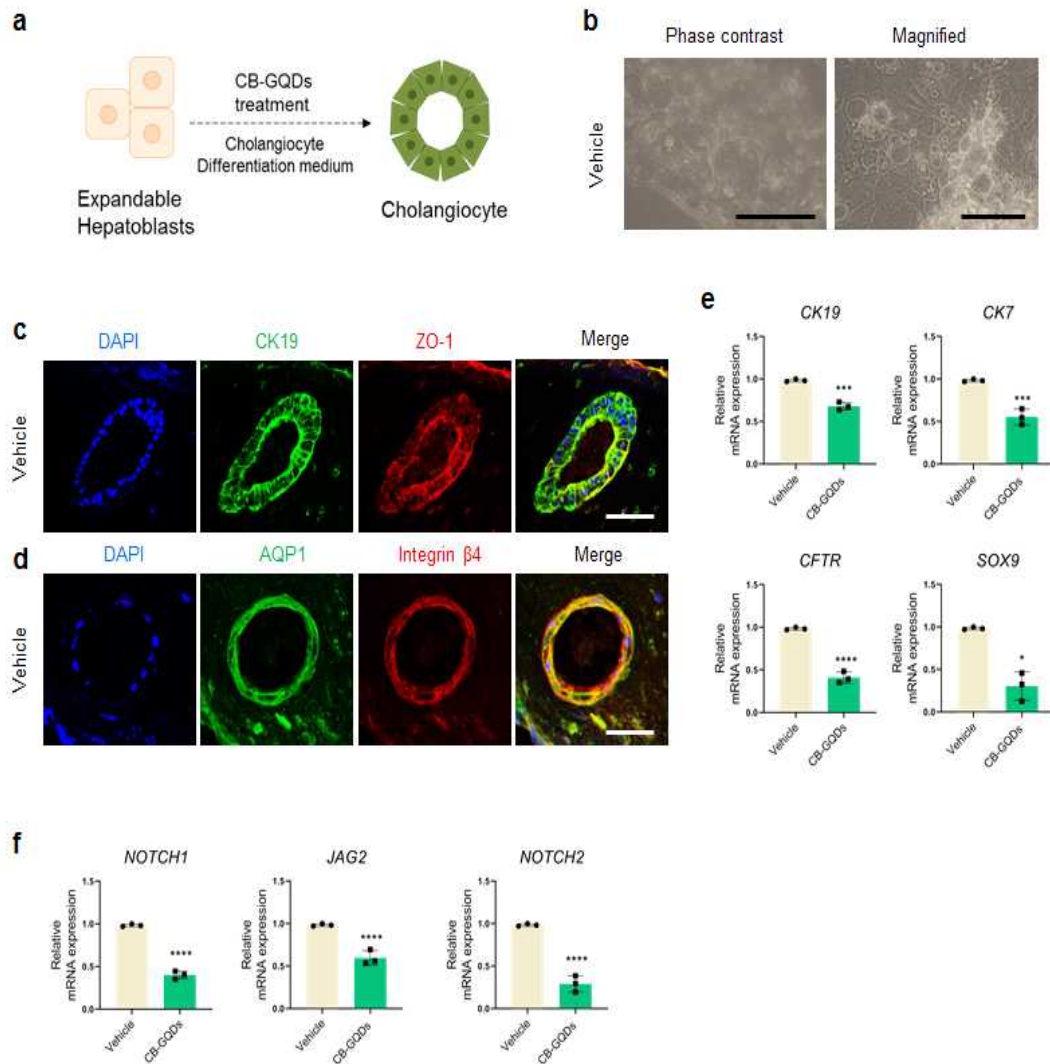
Figure 20. CB-GQDs treatment decreases cholangiocyte differentiation potential of hPSCs derived hepatoblasts in cholangiocyte differentiation medium.

a) Schematic illustration of hepatoblasts differentiation potential treated with CB-GQDs in cholangiocyte differentiation medium. b) Representative images for phase contrast microscopy of hHBs subjected to the cholangiocyte differentiation protocol. Bile duct-like structures are observed in collagen/Matrigel after 7 days of culture. Scale bar, 250

μm; magnified image, Scale bar, 100 μm. c)-d), Representative images of immunofluorescence staining for cholangiocyte markers b) CK19 (green)/ZO-1 (red) and c) AQP1 (green)/Integrin β4 (red). Nuclei were counterstained with DAPI (blue). Scale bar = 100 μm. e) Quantification of cholangiocyte-specific marker genes expression in cells treated with CB-GQDs by quantitative RT-PCR (RT-qPCR) analysis. GAPDH was used as an internal control for RT-qPCR. $*p < 0.05$, $***p < 0.001$ and $****p < 0.0001$. f) Quantification of Notch signaling associated genes expression in cells treated with CB-GQDs by quantitative RT-PCR (RT-qPCR) analysis. GAPDH was used as an internal control for RT-qPCR. $****p < 0.0001$. Data are means ± S.D. e), f), n=3 biologically independent samples. e), f). Two-tailed t-test e), f)

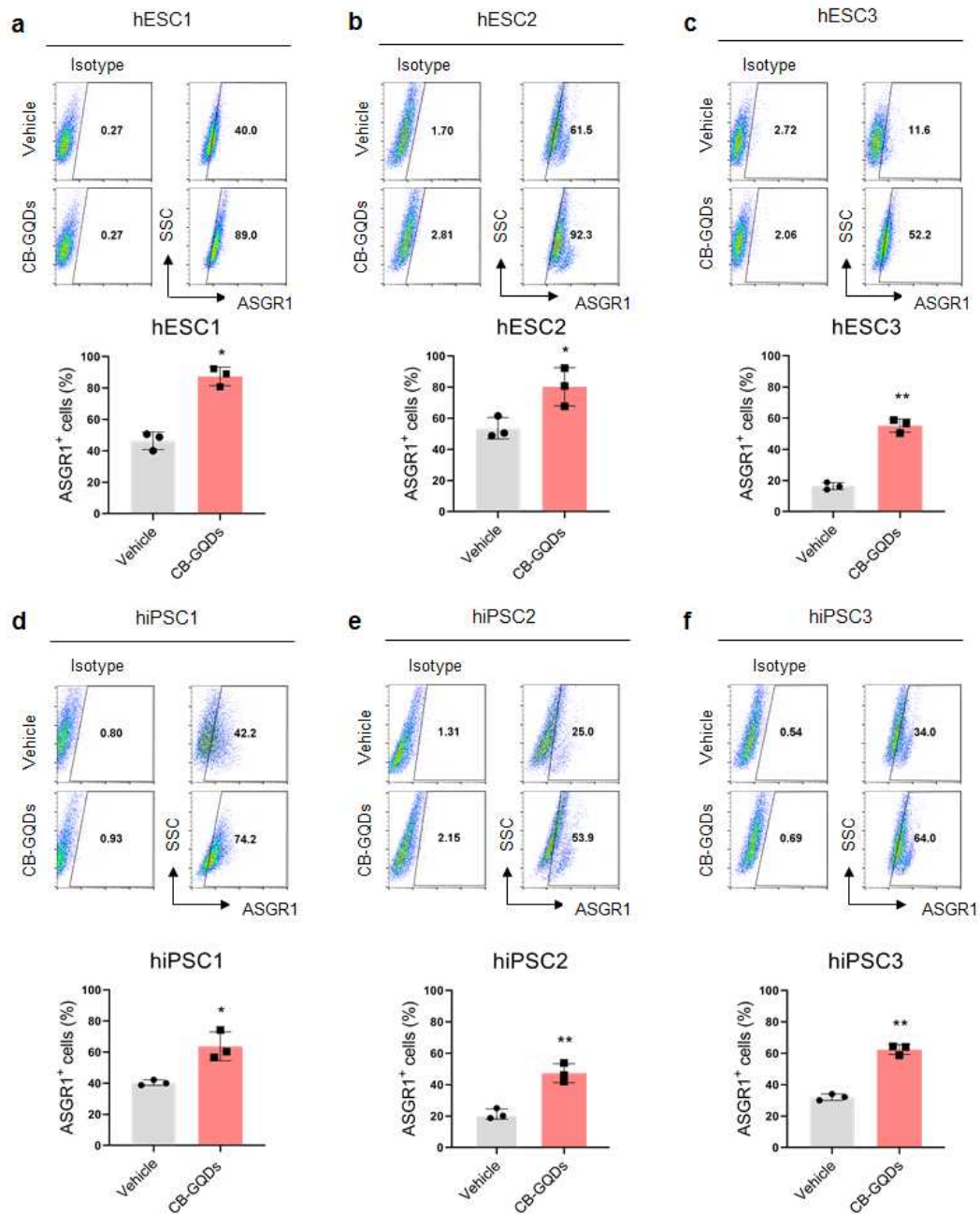**Figure 21. The effect of enhancement of hepatocyte maturation by CB-GQDs treatment in three hESCs and three hiPSCs.**

a)-f), Quantification of ASGR1 positive cells cultured in hepatocyte differentiation medium supplemented with or without CB-GQDs using

flow cytometry analyses, $*p < 0.05$ and $**p < 0.01$ represent the significance of CB-GQDs treatment. Data are means ±S.D. n=3 biologically independent samples. Two-tailed t-test.

2.3.4 CB-GQDs increases the efficiency of hepatoblast differentiation through the IGF1R/AKT pathway, regardless of the presence or absence of growth factors

Based on a report showing that insulin and insulin growth factor (IGF) induce effective hepatocyte differentiation via the PI3K/AKT pathway (Magner et al., 2013), we further investigated whether CB-GQDs have the capacity to activate the IGF1R pathway. IGF1R is a large tyrosine kinase receptor present in human cell plasma membranes that is activated by interacting with insulin-like growth factors, and it mediates the phosphoinositide 3-kinase (PI3K-)/Akt and Ras/extracellular signal regulation kinase (ERK) pathways (Baserga et al., 2000). Because the expression of IGF1R decreases as hepatocytes mature (Waraky et al., 2016) the mechanism underlying the action of CB-GQDs was investigated only in hepatoblast differentiation and not in hepatocyte differentiation. To evaluate the function of CB-GQDs, we then analysed the time-dependent phosphorylation status of IGF1R and primary downstream effectors implicated in the control of hepatoblast differentiation. Among the normal hepatoblast medium components (HB), fetal bovine serum (FBS) has an unclear effect on activating signalling pathways; thus, FBS was removed from the hepatoblast medium (HBF). Since basal signals in the presence of growth factors can lead to misinterpretation, the IGF1R signalling pathway and effects of CB-GQDs were examined in the presence and absence of growth factors. Based on the presence and absence of growth factors in the medium and the stimulation of hPSC-derived hepatoblasts with CB-GQDs IGF1R was tyrosine-phosphorylated in a time-dependent manner, with a peak activation at an hour (Figure 23 (a)).

Independent of the presence or absence of growth factors, the activation of IGF1R-AKT (Figure 22 (a)) significantly induced the

expression of hepatoblast markers ALB, AFP, EpCAM, and CK19 (Figure 22 (b)), suggesting that IGF1R-AKT signalling is a major chemical reaction that promotes hepatoblast differentiation. Additionally, even in the absence of growth factors, CB-GQDs alone activated IGF1R-AKT signalling to induce hepatoblast differentiation which has the potential to replace the IGF1 growth factor. To clearly verify that the CB-GQDs mediate IGF1R/AKT signalling to improve the hepatoblast efficiency, we blocked the activity of IGF1R and AKT with the selective inhibitors PPP and LY294002, respectively. PPP prevented the phosphorylation of both IGF1R and AKT and blocked the CB-GQD- mediated enhancement of hepatoblast differentiation, which we evaluated by qRT-PCR, flow cytometry, and western blotting (Figure 22 (c)-(e) and Figure 23 (d)-(e)). We observed that LY294002 treatment did not affect the CB-GQD- mediated IGF1R phosphorylation, indicating that IGF1R is upstream of CB-GQD-induced AKT phosphorylation (Figure 22 (c)-(e) and Figure 24 (d)-(e)). Previous results showed that the reduction in ERK in the presence of growth factors was concentration-dependent upon CB-GQD treatment (Figure 22 (a) and Figure 23 (a)).

Considering that AKT and ERK are two major downstream molecules for IGF1R (Wu et al., 2019), we used the ERK- specific inhibitor, U0126 to determine the effect of the decreasing the phosphorylation of ERK on hepatoblast differentiation efficiency. Increases in the concentration of U0126 reduced the hepatoblast differentiation efficiency in the presence of growth factors (Figure 24 (a)-(c)), and we demonstrated that the decrease in CB-GQD-mediated ERK negatively regulated the hepatoblast differentiation efficiency. Overall, the presence of growth factors reduced ERK phosphorylation,

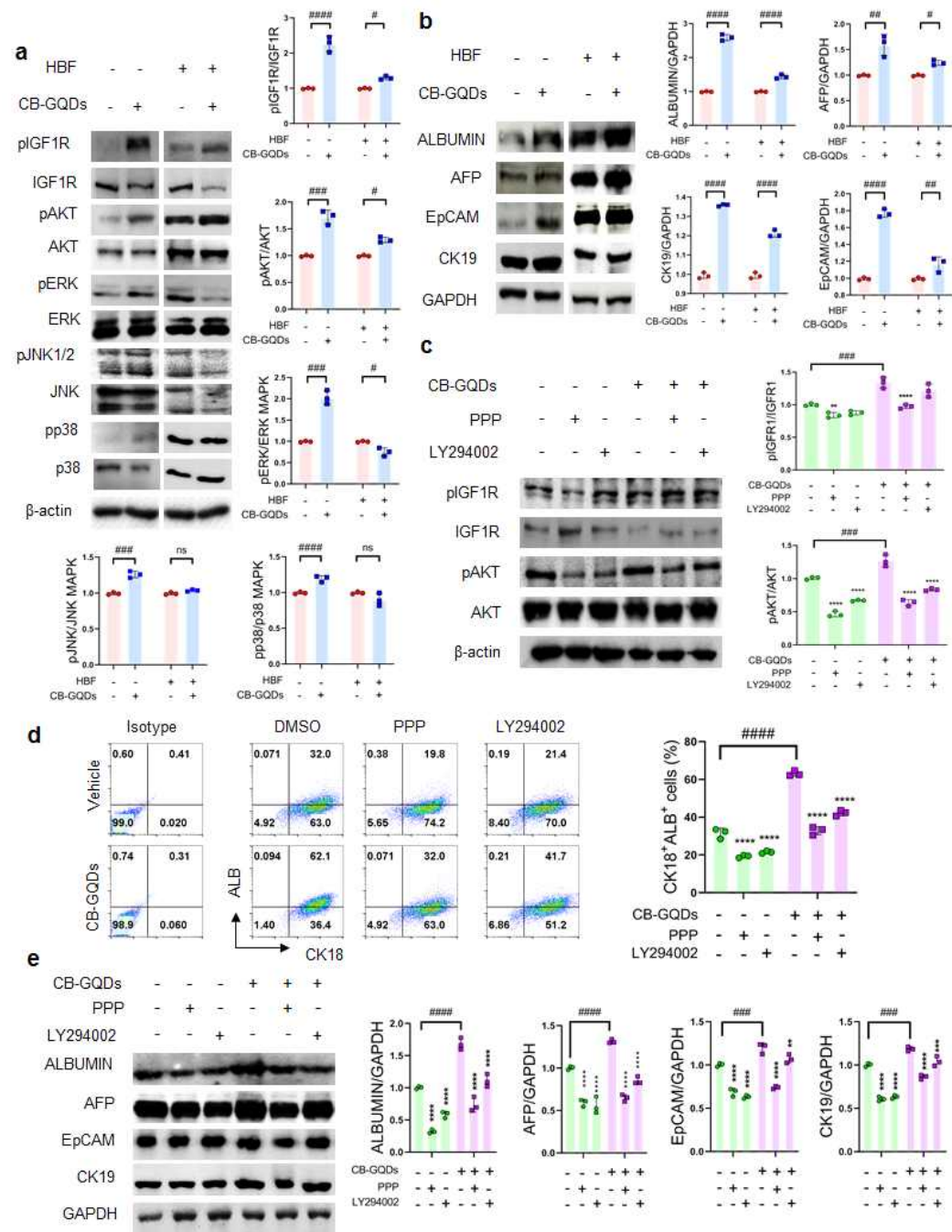thus indicating growth factor signals interfere with CB-GQD-mediated signals.

Figure 22. Evaluation of hepatoblast differentiation effect and IGF1R signal activity of CB-GQDs with or without growth factors.

a) Representative immunoblot images for indicated protein expression cultured in hepatoblast medium excluded FBS (HBF) with or without growth factors during an hour CB-GQDs treatment. Indicated protein expression was quantified. β-actin served as a loading control. #p < 0.05, ###p < 0.001 and ####p < 0.0001. n.s: no significance. b) Representative hepatoblast markers, ALBUMIN, AFP, EpCAM, CK19, GAPDH proteins expression quantified by western blot analyses. GAPDH served as a loading control. Qunatification of indicated hepatoblast markers, ALBUMIN, AFP, EpCAM, CK19 was normalized to GAPDH. #p < 0.05, ##p < 0.01 and ####p < 0.0001. c) Representative immunoblot images of IGF1R and AKT suppression using the specific inhibitor, PPP and LY294002, respectively. β-actin served as a loading control. **p < 0.01 and ****p < 0.0001 represent significance between control and each group under indicated chemical for indicated proteins expression. ###p < 0.001 denote significance for CB-GQDs treatment. d) Reduction in hepatoblast differentiation resulted from PPP and LY294002 treatment was identified by flow cytometry. Quantification for the co-expression of CK18 and ALBUMIN in the cells cultured under indicated chemical. ****p < 0.0001 represents significance between control and each group under indicated chemical for indicated proteins expression. ####p < 0.0001 denote significance for CB-GQDs treatment. e) Western blotting confirmed the expression of ALBUMIN, AFP, EpCAM, CK19, representative hepatoblast markers following each inhibitor and CB-GQDs treatment. GAPDH served as a loading control. **p < 0.01 and ****p < 0.0001 represent significance between control and each group under indicated chemical for indicated proteins expression. ####p < 0.0001 denote significance for CB-GQDs treatment. Data are means ± S.D. a), b), c), d), e), n=3 biologically

independent samples b), c), e), f), j), k). Two-tailed t-test a), b); Two-way ANOVA with Sidak's multiple comparisons test c), d), e)

Figure 23. Evaluation of hepatoblast differentiation effect and IGF1R signal activity of CB-GQDs with or without growth factors.

a) Representative immunoblot images for indicated protein expression cultured in hepatoblast medium excluded FBS (HBF) with or without

growth factors during an hour CB-GQDs treatment. Indicated protein expression was quantified. β-actin served as a loading control. #p < 0.05, ###p < 0.001 and ####p < 0.0001. n.s: no significance. b) Representative hepatoblast markers, ALBUMIN, AFP, EpCAM, CK19, GAPDH proteins expression quantified by western blot analyses. GAPDH served as a loading control. Qunatification of indicated hepatoblast markers, ALBUMIN, AFP, EpCAM, CK19 was normalized to GAPDH. #p < 0.05, ##p < 0.01 and ####p < 0.0001. c) Representative immunoblot images of IGF1R and AKT suppression using the specific inhibitor, PPP and LY294002, respectively. β-actin served as a loading control. **p < 0.01 and ****p < 0.0001 represent significance between control and each group under indicated chemical for indicated proteins expression. ###p < 0.001 denote significance for CB-GQDs treatment. d) Reduction in hepatoblast differentiation resulted from PPP and LY294002 treatment was identified by flow cytometry. Quantification for the co-expression of CK18 and ALBUMIN in the cells cultured under indicated chemical. ****p < 0.0001 represents significance between control and each group under indicated chemical for indicated proteins expression. ####p < 0.0001 denote significance for CB-GQDs treatment. e) Western blotting confirmed the expression of ALBUMIN, AFP, EpCAM, CK19, representative hepatoblast markers following each inhibitor and CB-GQDs treatment. GAPDH served as a loading control. **p < 0.01 and ****p < 0.0001 represent significance between control and each group under indicated chemical for indicated proteins expression. ####p < 0.0001 denote significance for CB-GQDs treatment. Data are means ±S.D. a), b), c), d), e), n=3 biologically independent samples b), c), e), f), j), k). Two-tailed t-test a), b); Two-way ANOVA with Sidak's multiple comparisons test c), d), e)
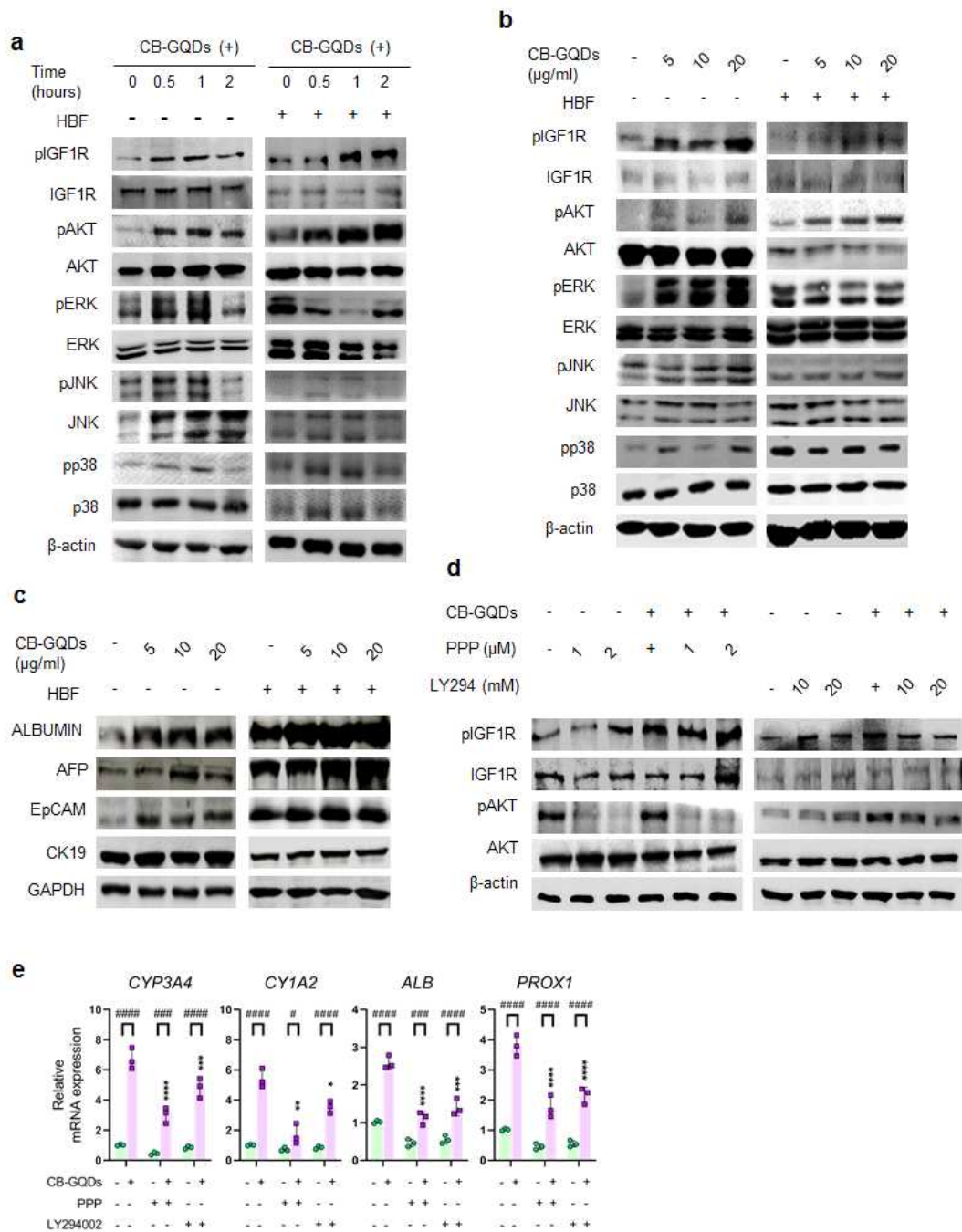
Figure 24. Downregualtion of ERK negatively regulates hepatoblast differentiation.

a) hHBs were pre-treated with the various concentration of U0126 for 30 min after overnight incubation in HBF medium and then cultured for 5 days in HBF medium with and without 5 μg/ml CB-GQDs supplementation. GAPDH served as a loading control. **p < 0.01 and

****p < 0.0001 represent significance between DMSO and other group for indicated proteins expression. ##p < 0.01, ####p < 0.0001. ns; no significance. b) Quantification for the co-expression of CK18 and ALBUMIN cells cultured in HB medium supplemented with or without CB-GQDs and inhibited by various concentration of U0126 using flow cytometry analyses. *p < 0.05, ***p < 0.001 and ****p < 0.0001 represent significance between DMSO and other group for indicated proteins expression. ###p < 0.001 and ####p < 0.0001. c) Western blotting images for representative hepatoblast markers, ALBUMIN, AFP, EpCAM and CK19 under indicated concentration of U0126 and quantified. Error bars represent the means ± S.D. from three separate experiments. Data analyzed by two-tailed t-test. **p < 0.01, ***p < 0.001 and ****p < 0.0001. n.s: no significance ####p < 0.0001 denote significance among each group under indicated U0126 concentration. Data are means ±S.D. n=3 biologically independent samples. Two-tailed t-test a), b), c)
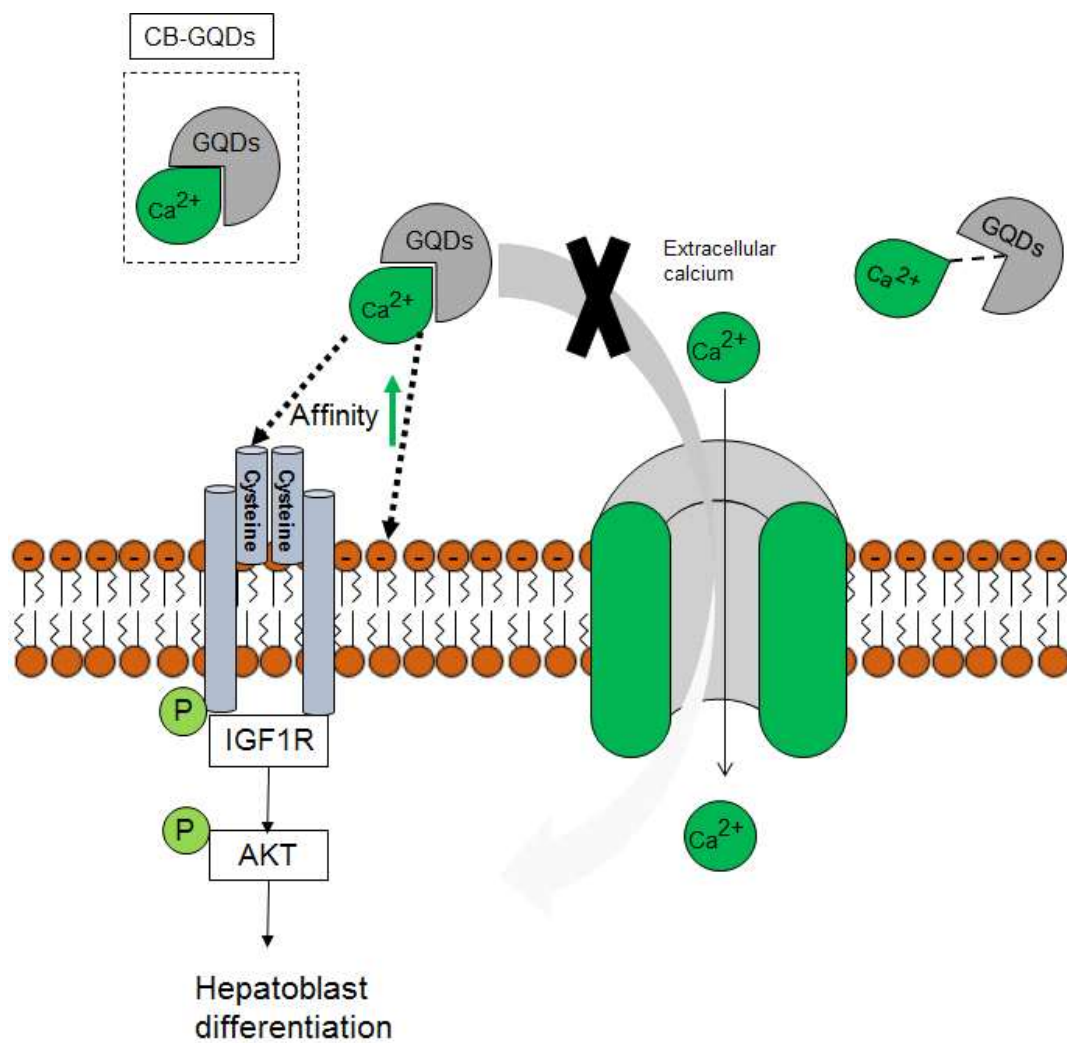
Figure 3.8. Schematic representation of how CB-GQD regulates hepatic differentiation in hPSCs.

2.4 DISCUSSION

Based on these results, CB-GQDs can interact with growth factor signals in the medium to promote or reduce specific lineage differentiation in a complementary manner by adding it to the medium. This showed the need to confirm the possibility of CB-GQDs as an independent as well as a complementary role as a growth factor. Growth factors are proteins involved in the differentiation and proliferation of stem cells and are routinely used in cellular biology and biomedical applications. These growth factors, combined with specific receptors, act as signaling factors in cells. Previous results (He et al., 2015; Lee et al., 2011; Ku et al., 2021) of correlation with differentiation rates using GQDs, potentially showing that GQDs can be used as a substrate to trigger different signals in cells and biomolecules. In many papers, the effects of graphene have been intensively explored (Tajik et al., 2020; Chen et al., 2012), but how graphene-related materials perform these biomedical effects has yet to be clearly explained. Furthermore, there is still a lack of systematic review in the interaction between graphene and biological systems at the cellular level. Given that the major signaling pathways that control human growth and development are the results of a combination of multiple pathways at different levels, the effects and signals of graphene and its derivatives need to be investigated first through the development of mammalian cells in vitro (Vert et al., 2011; Liao et al.,

2018).

Considering that AKT and ERK are two major downstream molecules for IGF1R (Wu et al., 2019), we used ERK specific inhibitor, U0126 to determine the effect of the decreased phosphorylated ERK on hepatoblast differentiation efficiency. As the increasing concentration of U0126 reduced hepatoblast differentiation efficiency in the presence of growth factors (Supplementary Fig. 7a-c), we demonstrated that the decrease in CB-GQDs mediated ERK negatively regulates hepatoblast differentiation efficiency. Overall, the presence of growth factors reduced ERK phosphorylation, leading to the conclusion that growth factor signals interfere with CB-GQDs-mediated signals.

In this study, XPS and zeta potential were used to demonstrate the existence and ionization of calcium in CB-GQDs, however, the direct link between chelated calcium and IGF1R needs to be clarified. CB-GQDs containing calcium would have approached the calcium channel present in the phospholipid membrane more closely, improving the efficiency of hepatoblast differentiation because GQDs are negatively charged. Conventional IGFs simply enhance the other signals (Hakuno et al., 2018) but IGF1R was quickly phosphorylated within 1 hour, complementarily and independently, after CB-GQDs treatment. Based on this, it is reasonable to assume that CB-GQDs interact with IGF1R more directly rather than help secrete cytokines such as IGF1. Considering that IGF1R is receptor tyrosine kinases, CB-GQDs may play a critical role in understanding the development and progression of

many cancers as well as normal cellular processes such as differentiation, proliferation, and endocytosis.

In conclusion, this study showed that CB-GQDs with high calcium ion concentration improved the hepatoblast differentiation rate through the IGF1R-AKT pathway while being biocompatible, in contrast to that calcium ion free CF-GQDs shows no effect. As a result, a substantial number of functional hepatocyte-like cells were obtained by adding CB-GQDs to the hepatocyte differentiation medium of human pluripotent stem cells derived hepatoblasts. The independent association between IGF1R-AKT activity and hepatoblast differentiation rate suggests that IGF1 can be substituted with CB-GQDs and be employed as a differentiation factor. However, the mechanism that contributes to hepatocyte differentiation, not hepatoblast is assumed to be different from that of IGF1R activity, and thus, further studies are needed. It is expected that CB-GQDs with their unique calcium contents, biocompatibility, and chemical stability can be widely utilized as an important inducer to differentiate and proliferate a variety of cell lineages.

GENERAL CONCLUSION

To construct a artificial liver, it needs a structure that can make up an orgnan and a large number of cells. In the first study, an vitro hepatic model with increased drug sensitivity was established in combination with dynamic condition. In conclusion, the successful combination of applied extrusion-based bioprinting technology with laminin-521-enriched biocompatible bioink facilitates the fabrication of a 3D in vitro model capable of supporting the structural integrity and tunability of mechanical properties in a precisely controlled manner. Bioengineered hepatic constructs with controlled stiffness respond weakly to chemically induced microenvironmental signals and impair metabolic processes under static conditions, but these processes are improved upon the incorporation of a dynamic environment generated by an orbital shaker. The dynamic environment incorporated into these bioprinted hepatic constructs promotes a long-term culture period, resulting in enhanced functionality. Indeed, the dynamic environment replicates the complex in vivo microenvironment, including physiological and mechanical cues, permitting the study of induced fibrogenesis mechanisms at the cellular level and evaluation of the effects of drugs. Additionally, under spinning conditions, the increased number of existing healthy spheroids that play an important role in drug metabolism and the remarkable viability of encapsulated cells suggest that this combined strategy in bioprinted hepatic constructs can be utilized for accurate drug evaluation for hepatotoxicity prevention and induction. Indeed, enhancement of drug susceptibility verified by APAP-induced hepatotoxicity and alleviation by NAC administration through spinning conditions allowed the development of a novel culture system to study the human liver in the dish. Furthermore, this unique

culture system will provide an excellent opportunity to scale up the advantages of 3D bioprinting technology with enhanced functionality and proliferation capacity compared to currently existing in vitro hepatic models. The combined application of 3D printing technology and subsequent spinning conditions improves the quality of 3D modeled tissue, is not resource-intensive and reduces labor costs and the need for reagents for further commercialization of the method in research applications and personalized medicine or cell therapy.

In the second study showed that CB-GQDs with high calcium ion concentration improved the hepatoblast differentiation rate through the IGF1R-AKT pathway while being biocompatible, in contrast to that calcium ion free CF-GQDs shows no effect. As a result, a substantial number of functional hepatocyte- like cells were obtained by adding CB-GQDs to the hepatocyte differentiation medium of human pluripotent stem cells derived hepatoblasts. The independent association between IGF1R-AKT activity and hepatoblast differentiation rate suggests that IGF1 can be substituted with CB-GQDs and be employed as a differentiation factor. However, the mechanism that contributes to hepatocyte differentiation, not hepatoblast is assumed to be different from that of IGF1R activity, and thus, further studies are needed. It is expected that CB-GQDs with their unique calcium contents, biocompatibility, and chemical stability can be widely utilized as an important inducer to differentiate and proliferate a variety of cell lineages.

REFERENCES

Abbas, A., Mariana, L.T., and Phan, A.N. 2018. Biomass-waste derived graphene quantum dots and their applications. Carbon, 140, 77-99.

Abbas, A., Tabish, T.A., Bull, S.J., Lim, T., M., Phan, A.N. 2020. High yield synthesis of graphene quantum dots from biomass waste as a highly selective probe for Fe^{3+} sensing. Sci Rep, 10, 21262.

Acik, M., Lee, G., Mattevi, C., Pirkle, A., Wallace, R.M., Chhowalla, M., Cho, K., and Chabal, Y. 2011. The role of oxygen during thermal reduction of graphene oxide studied by infrared absorption spectroscopy. The Journal of Physical Chemistry C, 115, 19761-19781.

Ahmed, H.M.M., Salerno, S., Morelli, S., Giorno, L., and De Bartolo, L. 2017. 3D liver membrane system by co-culturing human hepatocytes, sinusoidal endothelial and stellate cells. Biofabrication, 9, 25022.

Atkins, A.R., Brereton, I.M., Kroon, P.A., Lee, H.T., and Smith, R. 1998. Calcium is essential for the structural integrity of the cysteine-rich, ligand-binding repeat of the low-density lipoprotein receptor. Biochemistry, 37, 1662-1670.

Baserga, R. 2000. The contradictions of the insulin-like growth factor 1 receptor. Oncogene, 19, 5574-5581.

Bhatia, S.N., Underhill, G.H., Zaret, K.S., and Fox, I.J. 2014. Cell and tissue engineering for liver disease. Sci. Transl. Med, 6, 245sr2.

Bhise, N.S., Manoharan, V., Massa, S., Tamayol, A., Ghaderi, M., Miscuglio, M., Lang, Q., Zhang, Y.S., Shin, S.R., Calzone, G., Annabi, N., Shupe, T.D, Bishop, C.E., Atala, A., Dokmeci, M.R., and Khademhosseini, A. 2016. A liver-on-a-chip platform with bioprinted hepatic spheroids. Biofabrication, 8, 14101.

Borude, P., Bhushan, B., and Apte, U. 2018. DNA damage response regulates initiation of liver regeneration following aceta-minophen overdose. Gene Expr, 18, 115.

Cameron, K., Tan, R., Schmidt-Heck, W., Campos, G., Lyall, M.J., Wang, Y., Lucendo-Villarin, B., Szkolnicka, D., Bates, N., Kimber, S.J., Hengstler, J.G., Godoy, P., Forbes, S., and Hay, D.C. 2015. Recombinant laminins drive the differentiation and self-organization of hESC-derived hepatocytes. Stem Cell Rep, 5, 1250-1262.

Carlsson, R., Engvall, E., Freeman, A., and Ruoslahti, E. 1981. Laminin and fibronectin in cell adhesion: Enhanced adhesion of cells from regenerating liver to laminin. Proc. Natl. Acad. Sci. USA, 78, 2403-2406.

Chang, R., Emami, K., Wu, H., and Sun, W. 2010. Biofabrication of a three-dimensional liver micro-organ as an in vitro drug metabolism model. Biofabrication, 2, 045004.

Chen, G.-Y., Pang, D.-P., Hwang, S.-M., Tuan, H.-Y., and Hu, Y.-C. 2012. A graphene-based platform for induced pluripotent stem cells culture and differentiation. Biomaterials, 33, 418-427.

Cho, S., and Yoon, J.-Y. 2017. Organ-on-a-chip for assessing environmental toxicants. Curr. Opin. Biotechnol, 45, 34-42.

Choi, S.S., and Diehl, A.M. 2009. Epithelial-to-mesenchymal transitions in the liver. Hepatology, 50, 2007-2013.

C.T. 2020. Progress in 3D bioprinting technology for tissue/organ regenerative engineering. Biomaterials, 226, 119536.

Cui, X., Li, J., Hartanto, Y., Durham, M., Tang, J., Zhang, H., Hooper, G., Lim, K., and Woodfield, T. 2020. Advances in Extrusion 3D Bioprinting: A Focus on Multicomponent Hydrogel-Based Bioinks. Adv. Healthc. Mater, 9, 1901648.

Das, P., Ganguly, S., Margel, S., and Gedanken, A. 2021. Tailor made magnetic nanolights: fabrication to cancer theranostics applications. Nanoscale Advances, 3, 6762-6796.

Datta, P., Dey, M., Ataie, Z., Unutmaz, D., and Ozbolat, I.T. 2020. 3D bioprinting for reconstituting the cancer microenvironment. npj Precis. Oncol, 4, 1-13.

Davoodi, E., Sarikhani, E., Montazerian, H., Ahadian, S., Costantini, M., Swieszkowski, W., Willerth, S., Walus, K., Mofidfar, M., Toyserkani, E., Khademhosseini, A., and Ashammakhi, N. 2020. Extrusion and Microfluidic-Based Bioprinting to Fabricate Biomimetic Tissues and Organs. Adv. Mater. Technol, 5, 1901044.

Duval, K., Grover, H., Han, L.-H., Mou, Y., Pegoraro, A.F., Fredberg,

J., and Chen, Z. 2017. Modeling Physiological Events in 2D vs. 3D Cell Culture. Physiology, 32, 266-277.

Dvorak, M.M., Siddiqua, A., Ward, D.T., Carter, D.H., Dallas, S.L., Nemeth, E.F., and Riccardi, D. 2004. Physiological changes in extracellular calcium concentration directly control osteoblast function in the absence of calciotropic hormones. Proceedings of the National Academy of Sciences, 101, 5140-5145.

Eckl, P.M., Whitcomb, W.R., Michalopoulos, G. and Jirtle, R.L. 1987. Effects of EGF and calcium on adult parenchymal hepatocyte proliferation. Journal of cellular physiology, 132, 363-366.

Edmondson, R., Broglie, J.J., Adcock, A.F., and Yang, L. 2014. Three-Dimensional Cell Culture Systems and Their Applications in Drug Discovery and Cell-Based Biosensors. ASSAY Drug Dev. Technol, 12, 207-218.

Ferrari, A.C., and Robertson, J. 2000. Interpretation of Raman spectra of disordered and amorphous carbon. Physical review B, 61, 14095.

Ferrari, A.C., and Basko, D.M. 2013. Raman spectroscopy as a versatile tool for studying the properties of graphene. Nature nanotechnology, 8, 235-246.

Goldman O., and Gouon-Evans V. 2016. Human pluripotent stem cells: myths and future realities for liver cell therapy. Cell Stem

Cell, 18, 703-706.

Hakuno, F., and Takahashi, S.-I. 2018. 40 years of IGF1: IGF1 receptor signaling pathways. Journal of molecular endocrinology, 61, T69-T86.

Hay, D.C., Fletcher, J., Payne, C., Terrace, J.D., Gallagher, R.C., Snoeys, J., Black, J.R., Wojtacha, D., Samuel, K., and Hannoun, Z. 2008. Highly efficient differentiation of hESCs to functional hepatic endoderm requires ActivinA and Wnt3a signaling. Proceedings of the National Academy of Sciences, 105, 12301-12306.

He, P., Sun, J., Tian, S., Yang, S., Ding, S., Ding, G., Xie, X., and Jiang, M. 2015. Processable aqueous dispersions of graphene stabilized by graphene quantum dots. Chemistry of Materials, 27, 218-226.

Hennings, H., Michael, D., Cheng, C., Steinert, P., Holbrook, K., and Yuspa, S.H. 1980. Calcium regulation of growth and differentiation of mouse epidermal cells in culture. Cell, 19, 245-254.

Huang, D., Gibeley, S.B., Xu, C., Xiao, Y., Celik, O., Ginsberg, H.N., and Leong, K.W. 2020. Engineering Liver Microtissues for Disease Modeling and Regenerative Medicine. Adv. Funct. Mater, 30, 1909553.

Hosseini, V., Maroufi, N.F., Saghati, S., Asadi, N., Darabi, M., Ahmad, S.N.S., Hosseinkhani, H., and Rahbarghazi, R. 2019. Current progress in hepatic tissue regeneration by tissue engineering. J. Transl. Med, 17,

1-24.

Iannazzo D., Pistone A., Salamò M., Galvagno S., Romeo R., Giofré S. V., Branca C., Visalli G. and Di Pietro A. 2017. Graphene quantum dots for cancer targeted drug delivery. International journal of pharmaceutics, 518, 185-192.

Jin, Y., Kim, J., Lee, J.S., Min, S., Kim, S., Ahn, D.H., Kim, Y.G., and Cho, S.W. 2018. Vascularized liver organoids generated using induced hepatic tissue and dynamic liver-specific microenvironment as a drug testing platform. Adv. Funct. Mater, 28, 1801954.

Jung, D.J., Byeon, J.H., and Jeong, G.S. 2020. Flow enhances phenotypic and maturation of adult rat liver organoids. Biofabrication, 12, 45035.

Kang, H.K., Sarsenova, M., Kim, D.-H., Kim, M.S., Lee, J.Y., Sung E.-A., Kook, M.G., Kim, N.G., Choi, S.W., and Ogay, V. 2021. Establishing a 3D In Vitro Hepatic Model Mimicking Physiologically Relevant to In Vivo State. Cells, 10, 1268.

Kajiwara, M., Aoi, T., Okita, K., Takahashi, R., Inoue, H., Takayama, N., Endo, H., Eto, K., Toguchida, J., and Uemoto, S. 2012. Donor-dependent variations in hepatic differentiation from human-induced pluripotent stem cells. Proceedings of the National Academy of Sciences, 109, 12538-12543.

Kanninen, L.K., Harjumäki, R., Peltoniemi, P., Bogacheva, M., Salmi, T., Porola, P., Niklander, J., Smutný, T., Urtti, A., Yliperttula, M.L.,

and Lou, Y.-R. 2016. Laminin-511 and laminin-521-based matrices for efficient hepatic specification of human pluripotent stem cells. Biomaterials, 103, 86-100.

Kido, T., Koui, Y., Suzuki, K., Kobayashi, A., Miura, Y., Chern, E.Y., Tanaka, M., and Miyajima, A. 2015. CPM is a useful cell surface marker to isolate expandable bi-potential liver progenitor cells derived from human iPS cells. Stem Cell Reports, 5, 508-515.

Kim, D., Yoo, J.M., Hwang, H., Lee, J., Lee, S.H., Yun, S.P., Park, M.J., Lee, M., Choi, S., and Kwon, S.H. 2018. Graphene quantum dots prevent α-synucleinopathy in Parkinson's disease. Nature nanotechnology, 13, 812.

Kim, D.J., Yoo, J.M., Suh, Y., Kim, D., Kang, I., Moon, J., Park, M., Kim, J., Kang, K.-S., and Hong B. H. 2021. Graphene Quantum Dots from Carbonized Coffee Bean Wastes for Biomedical Applications. Nanomaterials, 11, 1423.

Ku, T., Hao, F., Yang, X., Rao, Z., Liu, Q.S., Sang, N., Faiola, F., Zhou, Q., and Jiang, G. 2021. Graphene Quantum Dots Disrupt Embryonic Stem Cell Differentiation by Interfering with the Methylation Level of Sox 2. Environmental Science & Technology , 55, 3144-3155.

Kwon, Y.J., Lee, K.G., and Choi, D. 2015. Clinical implications of advances in liver regeneration. Clin. Mol. Hepatol, 21, 7-13.

Kwon, D., Ahn, H.-J., Han, M.-J., Ji, M., Ahn, J., Seo, K.-W., and Kang, K.-S. 2020. Human Leukocyte Antigen Class I Pseudo-Homozygous Mesenchymal Stem Cells Derived from Human Induced Pluripotent Stem Cells. Stem Cell Reviews and Reports, 16, 792-808.

Lauschke, V.M., Hendriks, D.F.G., Bell, C.C., Andersson, T.B., and Ingelman-Sundberg, M. 2016. Novel 3D Culture Systems for Studies of Human Liver Function and Assessments of the Hepatotoxicity of Drugs and Drug Candidates. Chem. Res. Toxicol, 29, 1936-1955.

Lee, B.-C., Lee, J.Y., Kim, J., Yoo, J.M., Kang, I., Kim, J.-J., Shin, N., Kim, D.J., Choi, S.W., Kim, D., Hong, B.H., and Kang, K.-S. 2020. Graphene quantum dots as anti-inflammatory therapy for colitis. Sci. Adv, 6, eaaz2630.

Lee, H., Chae, S., Kim, J.Y., Han, W., Kim, J., Choi, Y., and Cho, D.W. 2019. Cell-printed 3D liver-on-a-chip possessing a liver microen-vironment and biliary system. Biofabrication, 11, 025001.

Lee, J.Y., Yu, K.-R., Kim, H.-S., Kang, I., Kim, J.-J., Lee, B.-C., Choi, S.W., Shin, J.-H., Seo, Y. and Kang, K.-S. 2016. BMI1 inhibits senescence and enhances the immunomodulatory properties of human mesenchymal stem cells via the direct suppression of MKP-1/DUSP1. Aging (Albany NY), 8, 1670.

Lee, S.W., Jung, D.J., and Jeong, G.S. 2020. Gaining New Biological and Therapeutic Applications into the Liver with 3D In Vitro Liver Models. Tissue Eng. Regen. Med, 17, 731-745.

Lee, W.C., Lim, C.H.Y., Shi, H., Tang, L.A., Wang, Y., Lim, C.T., and Loh, K.P. 2011. Origin of enhanced stem cell growth and differentiation on graphene and graphene oxide. ACS nano, 5, 7334-7341.

Liang, Y.-L., Zhang, Z.-H., Liu, X.-J., Liu, X.-Q., Tao, L., Zhang, Y.-F., Wang, H., Zhang, C., Chen, X., and Xu, D.-X. 2012. Melatonin Protects against Apoptosis-Inducing Factor (AIF)-Dependent Cell Death during Acetaminophen-Induced Acute Liver Failure. PLoS ONE, 7, e51911.

Liao, C., Li, Y., and Tjong, S.C. 2018. Graphene nanomaterials: Synthesis, biocompatibility, and cytotoxicity. International journal of molecular sciences, 19, 3564.

Li, Z., Wu, J., Wang, L., Han, W., Yu, J., Liu, X., Wang, Y., Zhang, Y., Feng, G., and Li, W. 2019. Generation of qualified clinical-grade functional hepatocytes from human embryonic stem cells in chemically defined conditions. Cell death & disease, 10, 1-14.

Luckert, C., Schulz, C., Lehmann, N., Thomas, M., Hofmann, U., Hammad, S., Hengstler, J.G., Braeuning, A., Lampen, A., and Hessel, S. 2017. Comparative analysis of 3D culture methods on human HepG2 cells. Arch. Toxicol, 91, 393-406.

Lv, L., Liu, Y., Zhang, P., Zhang, X., Liu, J., Chen, T., Su, P., Li, H., and Zhou, Y. 2015. The nanoscale geometry of TiO2 nanotubes influences the osteogenic differentiation of human adipose-derived stem cells by modulating H3K4 trimethylation. Biomaterials, 39, 193-205.

Luong-Van, E., Madanagopal, T.T., and Rosa, V. 2020. Mechanisms of graphene influence on cell differentiation. Materials Today Chemistry, 16, 100250.

Ma, L., Wu, Y., Li, Y., Aazmi, A., Zhou, H., Zhang, B., and Yang, H. 2020. Current Advances on 3D-Bioprinted Liver Tissue Models. Adv. Healthc. Mater, 9, e2001517.

Magner, N.L., Jung, Y., Wu, J., Nolta, J.A., Zern, M.A., and Zhou, P. 2013. Insulin and IGFs enhance hepatocyte differentiation from human embryonic stem cells via the PI3K/AKT pathway. Stem Cells, 31, 2095-2103.

Manov, I., Hirsh, M., and Iancu, T.C. 2004. N-Acetylcysteine does not Protect HepG2 Cells against Acetaminophen-Induced Apoptosis. Basic Clin. Pharmacol. Toxicol, 94, 213-225.

Matai, I., Kaur, G., Seyedsalehi, A., McClinton, A., and Laurencin, Mandrycky, C., Wang, Z., Kim, K., and Kim, D.-H. 2016. 3D bioprinting for engineering complex tissues. Biotechnol. Adv, 34, 422-434.

Morgan, F.L.C., Moroni, L., and Baker, M.B. 2020. Dynamic Bioinks to Advance Bioprinting. Adv. Healthc. Mater., 9, 1901798.

Nguyen, D.G., Funk, J., Robbins, J.B., Crogan-Grundy, C., Presnell, S.C., Singer, T., and Roth, A.B. 2016. Bioprinted 3D Primary Liver Tissues Allow Assessment of Organ-Level Response to Clinical Drug Induced Toxicity In Vitro. PLoS ONE, 11, e0158674.

No, D.Y., Lee, K.-H., Lee, J., and Lee, S.-H. 2015. 3D liver models on a microplatform: Well-defined culture, engineering of liver tissue and liver-on-a-chip. Lab Chip, 15, 3822-3837.

Ozbolat, I.T., and Hospodiuk, M. 2016. Current advances and future perspectives in extrusion-based bioprinting. Biomaterials, 76, 321-343.

Ozbolat, I.T. Scaffold-Based or Scaffold-Free Bioprinting: Competing or Complementing Approaches?. 2015. J. Nanotechnol. Eng. Med, 6, 024701.

Palabiyik, S.S., Karakus, E., Halici, Z., Cadirci, E., Bayir, Y., Ayaz, G., and Cinar, I. 2016. The protective effects of carvacrol and thymol against paracetamol‑induced toxicity on human hepatocellular carcinoma cell lines (HepG2). Hum. Exp. Toxicol, 35, 1252-1263.

Pang, Y., Mao, S., Yao, R., He, J., Zhou, Z., Feng, L., Zhang, K., Cheng, S., and Sun, W. 2018. TGF-β induced epithelial‑mesenchymal transition in an advanced cervical tumor model by 3D printing. Biofabrication, 10, 044102.

Park, S.C., Yang, W.S., Ahn, J.Y., Park, J.B., Lee, J.-H., Jung, Y., Kim, H.R., Kim, J.Y., Lim, J.M., and Hong, B.H. 2021. Improved osteogenesis of human adipose-derived stromal cells on hydroxyapatite-mineralized graphene film. 2D Materials, 8, 035012.

Peng, J., Gao, W., Gupta, B.K., Liu, Z., Romero-Aburto, R., Ge, L., Song, L., Alemany, L.B., Zhan, X., and Gao, G. 2012. Graphene quantum dots derived from carbon fibers. Nano letters, 12, 844-849.

Peng, W., Unutmaz, D., and Ozbolat, I.T. 2016. Bioprinting towards Physiologically Relevant Tissue Models for Pharmaceutics. Trends Biotechnol, 34, 722-732.

Peters, D.T., Henderson, C.A., Warren, C.R., Friesen, M., Xia, F., Becker, C.E., Musunuru, K., and Cowan, C.A. 2016. Asialoglycoprotein receptor 1 is a specific cell-surface marker for isolating hepatocytes derived from human pluripotent stem cells. Development, 143, 1475-1481.

Pinzani, M. 2011. Epithelial-mesenchymal transition in chronic liver disease: Fibrogenesis or escape from death?. J. Hepatol, 55, 459-465.

Rashidi, H., Alhaque, S., Szkolnicka, D., Flint, O., Hay, D.C. 2016. Fluid shear stress modulation of hepatocyte-like cell function. Arch. Toxicol, 90, 1757-1761.

Roskams, T.A., Libbrecht, L., and Desmet, V.J. 2003. Progenitor Cells in Diseased Human Liver. Semin. Liver Dis, 23, 385-396.

Qiu, J., Li, D., Mou, X., Li, J., Guo, W., Wang, S., Yu, X., Ma, B., Zhang, S., and Tang, W. 2016. Effects of graphene quantum dots on the self-renewal and differentiation of mesenchymal stem cells. Advanced healthcare materials, 5, 702-710.

Sánchez-Romero, N., Sainz-Arnal, P., Pla-Palacín, I., Dachary, P.R., Almeida, H., Pastor, C., Soto, D.R., Rodriguez, M.C., Arbizu, E.O., Martinez, L.B., Serrano-Aullo, S., and Baptista, P.M. 2019. The role of extracellular matrix on liver stem cell fate: A dynamic relationship in health and disease. Differentiation, 106, 49-56.

Schmidt, S.K., Schmid, R., Arkudas, A., Kengelbach-Weigand, A., and Bosserhoff, A.K. 2019. Tumor Cells Develop Defined Cellular Phenotypes after 3D-Bioprinting in Different Bioinks. Cells, 8, 1295.

Schuster, S., Cabrera, D., Arrese, M., and Feldstein, A.E. 2018. Triggering and resolution of inflammation in NASH. Nat. Rev. Gastroenterol. Hepatol, 15, 349-364.

Shang W, Zhang X, Zhang M, Fan Z, Sun Y, and Han M. 2014. The uptake mechanism and biocompatibility of graphene quantum dots with human neural stem cells. Nanoscale, 11, 5799-5806.

Sharma, N., Sharma, I., and Bera, M.K. 2022. Microwave-Assisted Green Synthesis of Carbon Quantum Dots Derived from Calotropis Gigantea as a Fluorescent Probe for Bioimaging. Journal of Fluorescence, 35262854.

Snoeck, H.W. 2020. Calcium regulation of stem cells. EMBO

reports, 21, e50028.

Sung, E.A., Yu, K.R., Shin, J.H., Seo, Y., Kim, H.S., Koog, M.G., Kang, I., Kim, J.J., Lee, B.C., Shin, T.H., Lee, J.Y, Lee, S., Kang, T.-W., Choi, S.W., and Kang, K.-S. 2017. Generation of patient specific human neural stem cells from Niemann-Pick disease type C patient-derived fibroblasts. Oncotarget, 8, 85428.

Tajik, S., Dourandish, Z., Zhang, K., Beitollahi, H., Van Le, Q., Jang, H.W., and Shokouhimehr, M. 2020. Carbon and graphene quantum dots: A review on syntheses, characterization, biological and sensing applications for neurotransmitter determination. RSC Advances, 10, 15406-15429.

Takebe, T., Sekine, K., Enomura, M., Koike, H., Kimura, M., Ogaeri, T., Zhang, R.-R., Ueno, Y., Zheng, Y.-W., and Koike, N. 2013. Vascularized and functional human liver from an iPSC-derived organ bud transplant. Nature, 499, 481–484.

Talari, A.C.S., Raza, A., Rehman, S., and Rehman, I.U. 2017. Analyzing normal proliferating, hypoxic and necrotic regions of T-47D human breast cancer spheroids using Raman spectroscopy. Appl. Spectrosc. Rev, 52, 909-924.

Tasnim, F., Phan, D., Toh, Y.-C., and Yu, H. 2015. Cost-effective differentiation of hepatocyte-like cells from human pluripotent stem cells using small molecules. Biomaterials, 70, 115-125.

Tasoglu, S., and Demirci, U. Bioprinting for stem cell research. 2013. Trends Biotechnol, 31, 10-19.

Touboul, T., Chen, S., To, C.C., Mora-Castilla S., Sabatini K., Tukey R.H., and Laurent L.C. 2016. Stage-specific regulation of the WNT/ β-catenin pathway enhances differentiation of hESCs into hepatocytes. Journal of hepatology, 64, 1315-1326.

Vert, G., and Chory, J. 2011. Crosstalk in cellular signaling: background noise or the real thing?. Developmental cell, 21, 985-991.

Vig, P., Russo, F.P., Edwards, R.J., Tadrous, P.J., Wright, N.A., Thomas, H.C., Alison, M.R., and Forbes, S.J. 2006. The sources of parenchymal regeneration after chronic hepatocellular liver injury in mice. Hepatology, 43, 316-324.

Wang, S., Wang, X., Tan, Z., Su, Y., Liu, J., Chang, M., Yan, F., Chen, J., Chen, T., and Li, C. 2019. Human ESC-derived expandable hepatic organoids enable therapeutic liver repopulation and pathophysiological modeling of alcoholic liver injury. Cell research, 29, 1009-1026.

Waraky, A., Aleem, E., and Larsson, O. 2016. Downregulation of IGF-1 receptor occurs after hepatic linage commitment during hepatocyte differentiation from human embryonic stem cells. Biochemical and biophysical research communications, 478, 1575-1581.

Woo, D.H., Kim, S.K., Lim, H.J., Heo, J., Park, H.S., Kang, G.Y., Kim, S.E., You, H.J., Hoeppner, D.J., and Kim, Y. 2012. Direct and indirect contribution of human embryonic stem cell–derived hepatocyte-like cells to liver repair in mice. Gastroenterology, 142, 602–611.

Wu, F., Wu, D., Ren, Y., Huang, Y., Feng, B., Zhao, N., Zhang, T., Chen, X., Chen, S., and Xu, A. 2019. Generation of hepatobiliary organoids from human induced pluripotent stem cells. Journal of hepatology, 70, 1145-1158.

Wu, G., Wu, D., Lo, J., Wang, Y., Wu, J., Lu, S., Xu, H., Zhao, X., He, Y., Li, J., Demirci, U., and Wang. S. 2020. A bioartificial liver support system integrated with a DLM/GelMA-based bioengineered whole liver for prevention of hepatic encephalopathy via enhanced ammonia reduction. Biomater. Sci. 2020, 8, 2814-2824.

Yan, X., Yang, W., Shao, Z., Yang, S., and Liu, X. 2016. Graphene/single-walled carbon nanotube hybrids promoting osteogenic differentiation of mesenchymal stem cells by activating p38 signaling pathway. International journal of nanomedicine, 11, 5473.

Yang, R., Miki, K., He, X., Killeen, M.E., and Fink, M.P. 2009. Prolonged treatment with N-acetylcystine delays liver recovery from acetaminophen hepatotoxicity. Crit. Care, 13, 1-7.

Yang, X., Zhao, Q., Chen, J., Liu, J., Lin, J., Lu, J., Li, W., Yu, D., and Zhao, W. 2021. Graphene Oxide Quantum Dots Promote Osteogenic Differentiation of Stem Cells from Human Exfoliated Deciduous Teeth via the Wnt/β-Catenin Signaling Pathway. Stem Cells International, 2021.

Zayzafoon, M. 2006. Calcium/calmodulin signaling controls osteoblast growth and differentiation. Journal of cellular biochemistry, 97, 56-70.

Zhang, S., Li, Y., Song, H., Chen, X., Zhou, J., Hong, S., and Huang, M. 2016. Graphene quantum dots as the electrolyte for solid state supercapacitors. Scientific reports, 6, 1-7.

'국문 초록

바이오프린팅 기술과 그래핀 양자점을 이용한 인간 만능줄기세포 유래 간세포 분화효율 향상 연구

서울대학교 대학원

수의과대학

수의병인생물학 및 예방수의학 전공

강현경

(지도교수: 강경선)

미국에서는 15분마다 장기 이식 대기자 명단에 이름이 하나 씩 추가된다. 장기이식에 대한 수요는 빠르게 증가하지만 대기자 명 단 중 기증자로부터 일치하는 장기를 받을 수 있는 환자는 3분의 1 도 되지 않는다. 이러한 부족을 완화하기 위한 가장 유망한 기술 중 하나는 세포, 공학 및 재료 방법을 결합하여 인공 장기를 생산하는 조직 공학이다. 여러 장기 중 특히 간의 경우, 약물과 독소대사를 하는 것이 가장 큰 특징이다. 또한 약물개발시 부작용이 나타나는 대표적인 장기이므로 약물개발과 독성학적 평가를 함에 있어 체외 간 모델은 필수적이다. 인공 간을 만들기 위해서는 장기를 구성할 수 있는 구조체와 많은 수의 세포가 필요하다. 장기를 구성할 수 있 는 구조체는 탈세포화 과정을 거친 생체유래나 3D bioprinting 기술 을 통해 ECM 성분의 구조체를 직접 프린팅 하는 방법등이 있다.

이 연구의 첫 번째 부분에서는 3D bioprinting 기술을 통해 구조체를 프린팅 한 후 스피닝 세포배양조건을 활용하여 생체내 상 태와 생리적 관련이 있는 3차원 체외 간 모델을 구축하였다. 본 연 구에서는 우리 몸속의 가장 큰 장기인 간을 3차원 압출기반 바이오 프린팅 기술을 활용하여 프린팅하였다.. 그러나 현재 간과 같이 크 기가 큰 체외 모델에서는 중앙 부위가 저산소 상태로 인해 약물과 독소의 신진대사가 느리고 약해지기 때문에 체외 간 모델에서 정확 한 약물 효과를 예측하는 것은 여전히 어렵다. 여기서 우리는 육각

형 바이오프린트 간 구조를 구성하고 지속적인 매체 자극이 있는 동적 조건을 통합했다. 동적 조건은 실제 간의 영양소가 풍부한 정맥과 산소가 풍부한 동맥을 포함하는 이중 혈액 공급 순환 시스템을 모사하고자 하였다. 그 결과 동적 조건 하에서 바이오프린트된 간구조의 HepG2 세포는 정적 조건의 세포에 비해 증식능력과 기능성이 향상되었다. 또한, 회전 조건에서 배양된 생체 인쇄 간 구조에서 약물 유도 신호와 반응을 촉진하는 역할을 하는 스페로이드의 수가 증가했다. 또한, 동적 조건에서 HepG2 세포는 집중적인 TGFα 유도 상피에서 중간엽으로의 전이(EMT)를 나타내었고, 아세트아미노펜 유도 간 독성에 대한 감수성을 증가시켰으며, N-아세틸시스테인(NAC)의 투여에 의한 간 독성 예방도 증가시켰다. 이중 혈액 공급 순환 시스템의 충분한 양의 산소와 영양소는 생체내 간의 높은 재생 능력을 가능하게 하는데, 우리의 연구 결과를 종합하면, 바이오 프린팅된 간 구조를 생성하는 동안 사용된 동적 조건은 부분적으로 간 손상과 복구 현상의 재현을 가능하게 한다는 것을 보여준다. 이 단순하지만 효과적인 배양 전략은 약물 효과 평가를 위한 체외 모델링을 개선하기 위해 바이오프린트된 간 구조를 용이하게 한다.

첫 연구에서는 간암세포인 HepG2를 활용한 체외 인공 간 모델을 설립하였으나 질병 모델링 및 개인 맞춤 의료에는 유도만능

줄기세포가 각광 받고 있다. 그러나, 유도만능줄기세포에서 간세포로의 분화에서 낮은 분화효율은 최종적으로 많은 수의 분화된 세포를 얻기 어렵게 하기 때문에 극복해야 할 문제점 중 하나이다. 두 번째 연구에서는 커피콩 유래 그래핀 양자점을 활용하여 인간만능줄기세포에서 간세포로의 분화효율을 높여 많은 수의 간세포를 최종적으로 얻고자 하였다. 최근까지 그래핀 양자점은 다양한 세포 유형으로 줄기세포의 효율적인 분화를 촉진하는 것으로 밝혀졌다. 그러나 간 계통에서 이들의 생물학적 활성과 신호 전달 메커니즘은 완전히 조사되지 않았다. 여기서, 우리는 통합된 칼슘 이온들이 인슐린 유사 성장 인자 1 수용체(IGF1R)-AKT의 신호를 활성화하는 칼슘이 풍부한 커피콩 유래 그래핀 양자점를 활용하여 간세포 분화 속도를 촉진할 수 있다고 보고한다. 우리는 또한 커피콩 유래 그래핀 양자점 처리에서 인간 만능줄기세포에서 유래한 간 전구세포가 간세포와 유사한 세포로의 성숙을 상향 조절하고 담관세포에 대한 분화를 하향 조절하여 많은 수의 기능성 간세포를 성공적으로 얻는 경향이 있다는 것을 발견했다. 더욱이, 커피콩 유래 그래핀 양자점 처리로부터 인슐린 유사 성장인자 1 수용체의 활성화는 성장 인자에 관계없이 간세포 분화 효율을 향상시켜, 킬레이트 칼슘이 인슐린 유사 성장인자 1 수용체의 활성화에 중요한 역할을 할 수 있음을 암시한다. 이 연구 결과는 독립적인 생체 활성을 가진 커피콩 유래

113

그래핀 양자점이 인슐린 유사 성장 인자 1 대신 널리 사용될 수 있으며 비용 효율적인 성장 인자뿐만 아니라 잠재적 신규 분화인자로 활용될 수 있음을 시사한다.

감사의 글

열정 하나로 실험실 생활을 시작했던 기억이 엊그제 같은데 박사과정을 마치고 학위논문을 마무리하면서 감사의 글을 쓰고 있다니 여러 생각과 많은 감정들이 스쳐 지나갑니다. 줄기세포 연구에 대한 흥미로 수의과대학원에 진학하여 다양한 연구를 하시는 강경선 교수님 연구실에서 많은 것을 배웠고 감사하게도 좋은 인연들을 많이 만났습니다. 그 덕분에 짧지 않은 학위과정을 무사히 마칠 수 있었던 것 같습니다. 학위과정동안 배웠던 것을 바탕으로 앞으로 지치지 않고 미래를 향해 걸어가겠습니다.

먼저 6년 반에 걸친 학위과정 동안 저를 지도편달 해주신 지도교수님이신 강경선 교수님께 깊은 존경과 감사를 드립니다. 연구방향을 잘못 잡고 있을 때마다 무심히 탁탁 쳐주시고, 묵묵히 지켜봐 주셔서 포기하지 않고 학위과정을 마칠 수 있었습니다. 직접 말씀 드리지는 못했지만, 어려운 시기마다 도와주셔서 진심으로 감사했습니다. 교수님을 본받아 연구에 있어 언제나 열려있고 강한 추진력으로 목표한 바를 이루도록 노력하겠습니다. 바쁘신 와중에 소중한 시간을 내서 학위 논문의 방향을 잡아주시고 지도해주신 서울대학교 자연과학대학 생명과학과 이건수 교수님, 공영윤 교수님, 서

115

울대학교 수의과대학 윤준원 교수님, 강스템 바이오텍 이승희 박사님께도 감사드립니다. 또한 그래핀 양자점을 소개시켜주신 서울대학교 홍병희 교수님, 인턴 시절 격려와 함께 꿈을 북돋아 주신 가천대학교 홍인선 교수님, 유도만능줄기세포의 세계로 초대해 주신 권대기 박사님, 연구소에서 만난 소중한 인연이자 사수 같은 안희진 박사님, 저의 실험실 생활의 출발점을 같이 해 주셨던 임희영 박사님, 친언니처럼 항상 챙겨주시는 감사한 인연 한미정 선생님 께도 진심으로 감사드립니다.

학위과정동안 많은 시간을 함께 보낸 서울대학교 수의과대학 공중보건학 교실 식구들에게도 감사를 드리고 싶습니다. 짧은 인연이 아쉬웠던 형식오빠, 가까워지고 싶었던 유진언니, 잊지 못할 추억을 남겨준 인성오빠, 재밌는 언어를 구사하던 병철오빠, 뒤늦게 시작된 고마운 인연 진영언니, 스마트 가이 재준오빠, 교실 전반에 걸쳐 많은 것을 알려주셨던 최순원 박사님께 진심으로 감사드립니다. 저에게 많은 것을 베풀어줬던 태훈 오빠, 자상한 만큼 엄격했던 지희 언니께도 감사 인사를 드립니다. 듬직한 명근오빠, 실험실 웃는 추억 속 항상 존재하는 참치메이트 인연 은아선배, 열심히 실험에 매진하는 민수오빠, 똑 부러지는 다현언니, 똑똑한 후배 나리, 인턴시절을 같이 보냈던 승은, 현재 공보실 조교가 된 다솜, 우여곡절이 많았던 남교 에게도 감사 인사를 전합니다. 그리고 우리 멋진 후

배들, 다양한 표정의 소유자 희영이, 웃음이 많은 민지, 갓 발돋움을 시작한 막내 정주, 첫 논문의 기쁨을 같이 나눴던 즐거운 인연 Madina Sarsenova 에게 감사의 마음을 전합니다. 실험에 바빠 자주 만나지 못해도 늘 그 자리에 있어 준 친구들, 곧 출산을 앞둔 예비맘 다은이, 미국의 회계사가 된 인화, 꼼꼼하고 여성스러운 선생님 민정이, 치맥 메이트 혜원이, 분위기 메이커 용우 에게도 감사드립니다.

그리고 영원한 내 안식처이자 언제나 따뜻하게 사랑과 응원을 아끼지 않았던 우리 가족들, 아침마다 데려다 주시고 저를 위해 헌신하셨던 내 편 우리 아빠, 애정 어린 시선으로 학위과정의 어려움을 사랑으로 보듬어주셨던 우리 엄마, 딸 같은 아들이자 저를 믿어주었던 듬직한 우리 오빠 에게도 사랑과 감사의 마음을 전합니다. 지금까지 받았던 사랑과 응원을 되갚을 수 있게 앞으로 열심히 살겠습니다. 부모님께서 항상 말씀 하셨던 대로 모든 순간 감사하며 투정 부리지 않고 긍정적인 태도로 매순간 임하겠습니다. 마지막으로 학위과정 동안 넓은 마음과 애정으로 누구보다 가장 큰 힘이 되어준 사랑하는 형진이에게 감사의 인사를 전합니다.

고대하던 학위과정을 마치니 기쁘고 새로운 시작을 할 생각에 설레기도 하면서 다시금 각오를 다지게 됩니다. 많은 사람들에게

117

받았던 응원과 사랑만큼 열린 사고를 가지고 진취적인 연구자로 살
겠습니다. 다시 한번 도움 주신 분들께 진심으로 감사드립니다.

<div align="right">2022년 8월</div>

<div align="right">강현경 드림.</div>